UNIVERSITY OF ROCHESTER
LABORATORY FOR LASER ENERGETICS

Volume 79
April–June 1999
DOE/SF/19460-317

LLE Review

Quarterly Report

About the Cover:

Charles Kellogg, Sr. Lab Engineer (left), and Per Adamson, Lab Engineer, align the OMEGA equivalent-target-plane (ETP) diagnostic. The system samples 4% of an OMEGA beam just prior to delivery to target and allows for the capture of magnified images of on-target laser beam profiles. The sample is reflected off an uncoated wedge that is highlighted by a lamp in the background of the image near the target mirror structure. This instrument is a valuable tool for investigating beam-smoothing techniques such as smoothing by spectral dispersion (SSD) and is the diagnostic used for the measurements featured in the article beginning on p. 149. The two photos below show the detailed beam path of the laser beam to the two cameras: (a) an 8×10 film camera and (b) a scientific-grade CCD array.

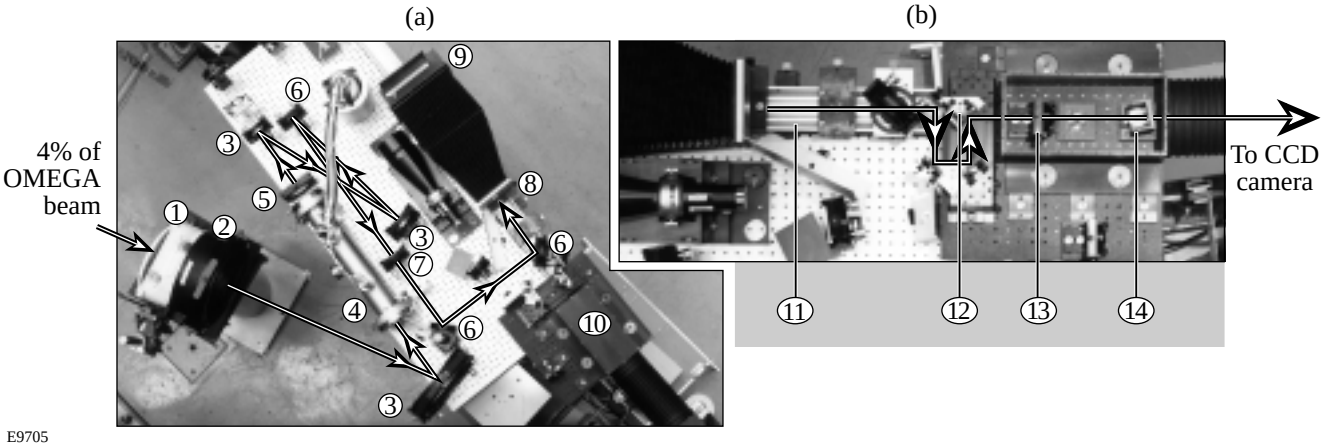

E9705

Photo (a). A full-aperture beam of 1/25th OMEGA intensity is phase scrambled at the DPP in location (1), focused by an *f*/6 lens (2), and brought through a vacuum image relay (4). As the beam is re-imaged by a collimating optic (5), excess energy is eliminated by reflections off uncoated front-surface mirrors (3). Mirrors (6) send the reduced-energy beam through a 2-m-focal-length lens (7) and into a wedged "rattle plate" (8) that generates an array of spots of decreasing intensity for the film camera (9). Photo (b) is a close-up view of the second arm of the detector where the beam is picked up off the rattle plate (11). Here the fifth beam of the array is redirected through a trombone (12), focusing element (13), and filter array (14) to the CCD detector.

The work described in this volume includes current research at the Laboratory for Laser Energetics, which is supported by New York State Energy Research and Development Authority, the University of Rochester, the U.S. Department of Energy Office of Inertial Confinement Fusion under Cooperative Agreement No. DE-FC03-92SF19460, and other agencies.

Printed in the United States of America
Available from
National Technical Information Services
U.S. Department of Commerce
5285 Port Royal Road
Springfield, VA 22161
Price codes: Printed Copy A04
Microfiche A01

For questions or comments, contact Samuel F. B. Morse, *Editor*, Laboratory for Laser Energetics, 250 East River Road, Rochester, NY 14623-1299, (716) 275-9672; e-mail: smor@lle.rochester.edu

Worldwide-Web Home Page: http://www.lle.rochester.edu/

UNIVERSITY OF ROCHESTER
LABORATORY FOR LASER ENERGETICS

Volume 79
April–June 1999
DOE/SF/19460-317

LLE Review

Quarterly Report

UR LLE

Contents

In Brief

This volume of the LLE Review, covering the period April–June 1999, features a theoretical analysis of direct-drive target performance on NIF. In this article R. P. J. Town, J. A. Delettrez, R. Epstein, V. N. Goncharov, R. L. McCrory, P. W. McKenty, R. W. Short, and S. Skupsky detail ignition target designs developed at LLE specifically to achieve successful direct-drive ignition on the NIF facility. A baseline "all-DT" target design is described along with a two shock compression analysis, which includes discussion of the parameters leading to variability in shock timing. The modeling and analysis presented flow down to specification requirements for the laser and target parameters to ignite this baseline target design with the NIF laser.

Additional highlights of the research presented in this issue are

- P.W. McKenty, M. D. Wittman, and V. N. Goncharov discuss the measurement of one of the critical parameters contributing to the performance of cryogenic DT targets: the uniformity of the inner ice surface. A numerical analysis is described that follows from a novel optical technique used to isolate the surface under investigation and resolve perturbations at the relevant level.

- B. Yaakobi, V. A. Smalyuk, J. A. Delettrez, and R. P. J. Town summarize the use of an embedded titanium layer in spherical targets to determine the areal density of the compressed shell. Target performance enhancement with the SSD beam-smoothing effect turned on is characterized with this method. A recently developed pinhole-array x-ray spectrometer captures core images below and above the *K*-edge energy of titanium. Results are compared with 2-D *ORCHID* simulations.

- S. P. Regan, J. Marozas, J. H. Kelly, T. R. Boehly, W. R. Donaldson, P. A. Jaanimagi, R. L. Keck, T. J. Kessler, D. D. Meyerhofer, W. Seka, S. Skupsky, and V. A. Smalyuk present techniques to characterize the laser-irradiation nonuniformity on OMEGA using time-integrated UV equivalent-target-plane imaging. A comparison of observed 2-D SSD beam-smoothing rates and theoretical predictions for the 0.2-THz SSD system currently on OMEGA permits confident extrapolation to larger-bandwidth smoothing effects.

- V. A. Smalyuk, T. R. Boehly, D. K. Bradley, V. N. Goncharov, J. A. Delettrez, J. P. Knauer, D. D. Meyerhofer, D. Oron, D. Shvarts, Y. Srebo, and R. P. J. Town discuss the growth and imprinting characteristics of planar targets in the presence of the three beam-smoothing effects available on OMEGA. Throughfoil radiography was used to observe the saturation of 3-D perturbations produced by laser imprinting; the results were compared to those predicted by the Haan model.

- F. Dahmani, A. W. Schmid, J. C. Lambropoulos, S. Papernov, and S. J. Burns, present experimental results on the changes in the thresholds for initiation of crack formation as well as propensity for crack growth in fused silica and BK7 glasses under applied stress. Biaxial applied stress is shown to raise damage thresholds by significant amounts for these optical materials common to fusion-class laser systems.

- J. L. Chaloupka and D. D. Meyerhofer discuss the trapping of high-energy electrons in a single-beam ponderomotive optical trap. Thomson-scattered light from the electron trap was enhanced through the use of a novel trapping focus of the laser. The scatter distribution is compared with simulations for ordinary and trapping-focus beams.

Samuel F. B. Morse
Editor

Direct-Drive Target Designs for the National Ignition Facility

The National Ignition Facility (NIF) is currently under construction at Lawrence Livermore National Laboratory (LLNL). One of the primary missions of the NIF is to achieve fusion ignition by means of inertial confinement fusion (ICF). Two main approaches have been considered for achieving thermonuclear yield in ICF. The first approach, known as indirect-drive ICF,[1] encloses a DT-fuel target inside a hohlraum. The laser beams are incident on the hohlraum's wall where the laser light is converted to x rays. These x rays then implode the target, leading to the ion temperature and ρR product necessary to achieve ignition. The second approach, known as direct-drive ICF, dispenses with the hohlraum and directly illuminates the laser light onto the target.

Direct drive offers a number of advantages[2] over indirect drive: (1) direct-drive designs have potentially higher gains than indirect drive; (2) direct-drive plasma coronas are not as susceptible to laser–plasma instabilities (LPI's) as indirect drive; (3) direct-drive targets are inherently less complex than indirect-drive hohlraum targets. Direct drive also has some potential disadvantages, especially the severe requirements on laser-beam uniformity.

Most of the U.S. research effort has centered on the indirect-drive approach, which is reflected in the decision to commence operations on the NIF in the indirect-drive configuration. NIF, however, is not to preclude direct drive, and it is currently expected that the NIF will be reconfigured for direct-drive operations commencing in 2009. Before the conversion to direct-drive operations, a number of modifications must be made to the NIF. First, to provide a uniform illumination of the direct-drive target, half the final optics assemblies (FOA's) must be relocated from the poles to the waist of the target chamber; second, direct-drive uniformity enhancements (2-D SSD[3] and polarization smoothing) must be added to all beamlines; and third, the cryogenic-handling system must be capable of "cradle-to-grave" operations.

This article describes the direct-drive ignition target designs developed at the University of Rochester's Laboratory for Laser Energetics (LLE). The following three sections will (1) outline the current direct-drive designs under investigation at LLE and NRL; (2) present a sensitivity study of the "all-DT" design; and (3) review the current laser and target specifications required to achieve a successful direct-drive ignition campaign on the NIF.

Direct-Drive Target Design Overview

Many common areas of physics exist between direct- and indirect-drive capsule designs. Both target designs require high compression of the DT fuel with a central high-temperature (>5-keV) ignition region. A typical implosion involves the deposition of energy (laser light in direct drive, x rays in indirect drive) on the target surface, which rapidly heats up and expands. As this *ablator* expands outward, the remainder of the shell is driven inward by the rocket effect compressing the fuel to the necessary density. The implosion can be tailored to give a number of assembled fuel configurations, such as isobaric with a uniform temperature and density in the fuel or isochoric with a high-temperature hot spot surrounding a low-temperature main fuel layer. The most energy efficient[1] configuration is isobaric with a central high-temperature *hot spot* surrounding a low-temperature *main fuel layer*. The central hot spot initiates the fusion reaction, which leads to a burn wave propagating into the main fuel layer; thus, for robust high-gain designs, it is vitally important to assemble the high-temperature hot spot and cold, dense main fuel layer accurately. For direct-drive target designs two main effects can prevent the correct assembly of the fuel: (1) preheat of the fuel and (2) hydrodynamic instabilities of the imploding shell.

Preheat of the DT fuel will increase the pressure of the fuel and thus make the target harder to compress. Preheat can arise from fast electrons, radiation, and the passage of shocks. The amount of preheat can be quantified in terms of the *adiabat* α of the implosion. The adiabat is defined as the ratio of the fuel's specific energy to the Fermi-degenerate specific energy. It can be shown that the gain G of the target scales as $\alpha^{-3/5}$. Fast electrons generated by laser–plasma processes (such as SBS, SRS, and two-plasmon decay) in the plasma corona can couple

into the fuel. These plasma processes occur when the intensity of the laser exceeds certain thresholds; thus, the control of fast-electron production constrains the maximum intensity of the design pulse. Radiative preheat and the passage of shocks are controlled by the target material and the shape of the laser pulse, respectively.

Hydrodynamic instabilities, such as the Rayleigh–Taylor instability (RTI), can seriously degrade the implosion by breaking the spherical symmetry of the implosion. The RTI occurs twice during the implosion: at the outer ablation surface as the shell accelerates inward and at the hot spot–main fuel layer interface as the capsule decelerates at the end of the implosion. Considerable theoretical,[4] numerical,[5] and experimental[6] work has demonstrated that the RT growth rate at the ablation surface is reduced from the classical value by ablative stabilization. From design simulations the ablation velocity v_a has been shown to scale as $\alpha^{-3/5}$. Another important parameter for stability considerations is the in-flight aspect ratio (IFAR). This is the ratio of the shell radius R to its thickness ΔR as the shell implodes. Higher IFAR implosions are more susceptible to hydrodynamic instabilities. Simulations have shown that the IFAR depends primarily on the square of the implosion velocity v^2_{imp} and the adiabat ($\alpha^{-3/5}$).

Control of the isentrope of the implosion is thus important for overall target gain ($G \sim \alpha^{-3/5}$) and target stability. Indirect-drive designs are believed to be sufficiently stable to hydrodynamic instabilities that they can operate very near the Fermi-degenerate limit ($\alpha = 1$). Direct-drive designs require the implosion to operate at a higher isentrope. LLE and NRL are currently investigating three designs (see Fig. 79.1) that use various combinations of shock and radiative heating to control the isentrope.

The first design [Fig. 79.1(a)] employs a solid (cryogenic) DT-shell target with a thin polymer ablator (required to fabricate the cryogenic shell) surrounding the DT-ice shell.[7] For this design the DT acts as both the fuel and the ablator. This design uses shock preheat to control the isentrope of the ablation surface and the fuel.

The second design [Fig. 79.1(b)] employs a low-density foam surrounding a clean cryogenic DT layer (a thin barrier layer separates the foam layer from the DT). The foam layer acts as the ablator. This design uses shock preheat to control the isentrope, but it offers the flexibility of placing the ablation surface and main fuel layer on different isentropes.

The third design [Fig. 79.1(c)] places a high-Z coating over a DT wicked foam ablator, which encases a pure-DT ice layer.[2] This design uses mainly radiative preheat. By carefully selecting the radiative properties of the high-Z ablator, it is possible to preferentially heat the carbon in the foam, boosting the isentrope of the ablation surface, while leaving the fuel on a lower isentrope.

Although the "all-DT" design has the disadvantage that the fuel and ablator are on the same adiabat, it has a number of significant advantages. First, the target is very simple, with no classically unstable RTI interfaces. Second, DT has a very high ablation velocity, which reduces the RTI at the ablation surface. Third, a DT ablator potentially gives higher hydrodynamic efficiencies, thus maximizing the achievable gain. Because of these considerations, a scaled version of this target design has been selected for experimental investigation on the OMEGA laser and is used as the base-line design for establishing the detailed specifications for the NIF. The next section presents a more-detailed review of the all-DT design.

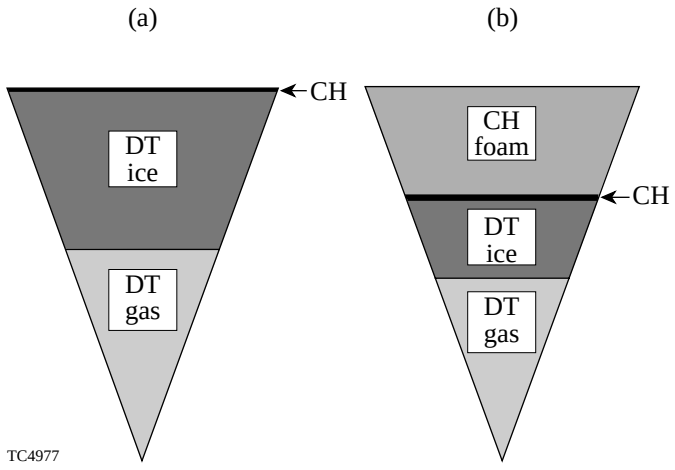

Figure 79.1
Schematic of the direct-drive target designs. (a) The all-DT target design, which relies on shock heating to select the adiabat. (b) The foam ablator design, which relies on shock heating to select the adiabat separately for the ablator and the fuel. (c) The radiative design, which relies on radiative absorption to select the adiabat for the ablator.

The Baseline All-DT Target Design

Figure 79.2 shows the gain curves constructed by LLE during the design phase of the NIF[7] for laser energies from 1 to 2 MJ and for implosions on isentropes from $\alpha = 1$ to 4. Variation in the isentrope was achieved by varying the incident laser pulse shape. Based on the results of current OMEGA experiments and theoretical calculations of these NIF designs, we have selected the 1.5-MJ, $\alpha = 3$ continuous-pulse design to be the baseline design for further study. Figure 79.3(a) shows the target specification; Fig. 79.3(b) shows the pulse shape for this design. This pulse shape consists of two distinct temporal regions: the foot and the main drive. The DT-ice thickness and adiabat of the implosion determine the length and duration of the foot. In this design, the foot is 4.25 ns long at a power of 10 TW. This region launches a 10-Mbar shock through the DT ice. At the time of shock breakout at the rear surface of the DT ice, the pulse ramps up to the drive region, which lasts for 2.5 ns at a power of 450 TW. This rapid rise in intensity generates pressures of approximately 80 Mbar and thus accelerates the DT ice inward. Different adiabats can be achieved by varying the length and intensity of the foot and carefully shaping the rise to the drive pulse. For example, an $\alpha = 2$ design has a longer, lower-intensity foot and a gentler-rising transition region.

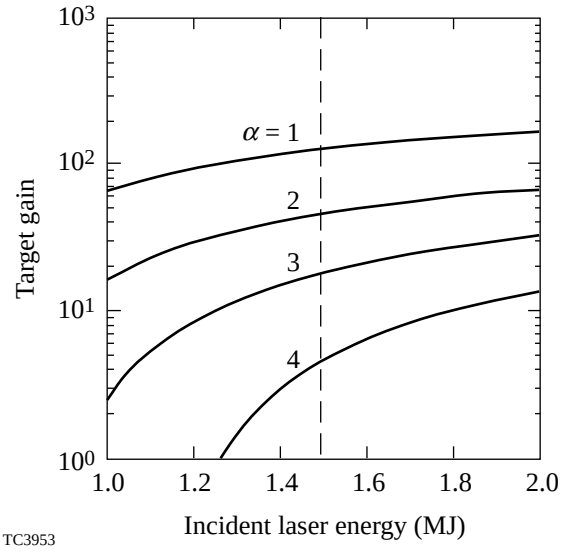

Figure 79.2
The gain curves constructed at LLE for various isentropes and incident laser energies. The dashed line corresponds to the NIF baseline 1.5-MJ energy.

The $\alpha = 3$ design is predicted, by 1-D calculations, to have a gain of 45, a neutron-averaged ion temperature of 30 keV, and a neutron-averaged $\rho R = 900$ mg/cm^2. The peak IFAR of this design is 60, and the hot-spot convergence ratio is 29. The conditions near peak compression ($t = 10.4$ ns) are shown in Fig. 79.4.

These direct-drive designs have two distinct shocks: the first is launched at the start of the pulse; the second is generated during the rise to the main drive intensity. Figure 79.5 is a contour map of the radial logarithmic derivative of the pressure [d(lnP)/dr] as a function of Lagrangian coordinate and time. The darker, more-intense regions represent a larger gradient in pressure and thus capture the position of the shocks. The timing between these two shocks determines the gain of the target design. When the first shock breaks out of the DT-ice layer (at 5.8 ns), a rarefaction wave expands outward from the rear surface of the DT ice. If the second shock arrives too late, the shock travels through a decreasing density gradient, which

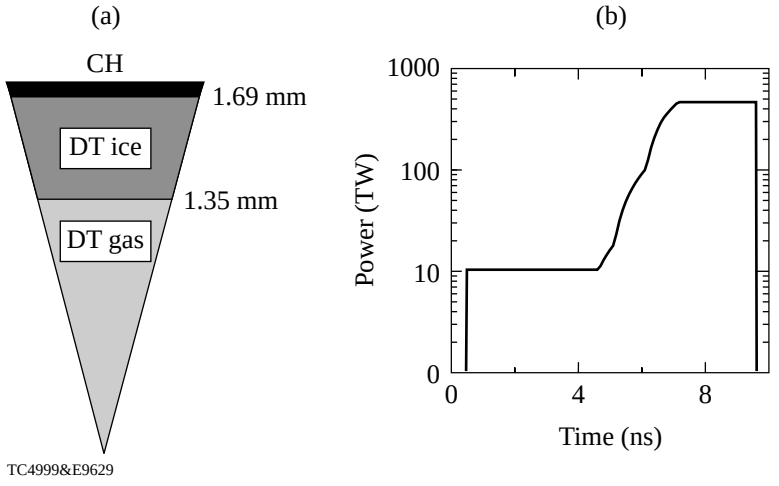

Figure 79.3
The baseline, $\alpha = 3$, "all-DT," 1.5-MJ target design. (a) The target specification and (b) the pulse shape.

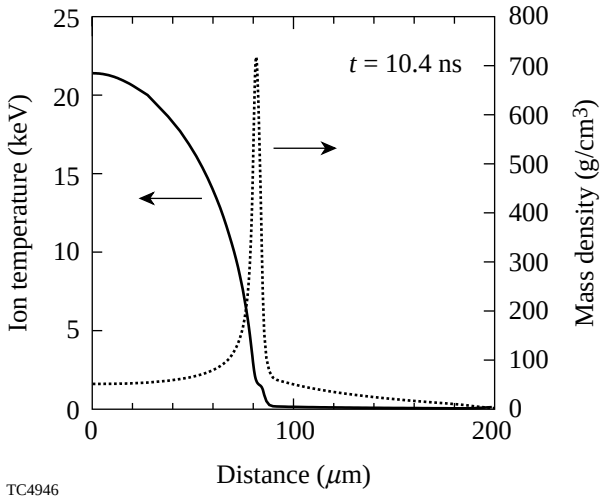

Figure 79.4
The ion temperature (solid line) and the mass density (dotted line) near peak compression for the $\alpha = 3$ baseline design.

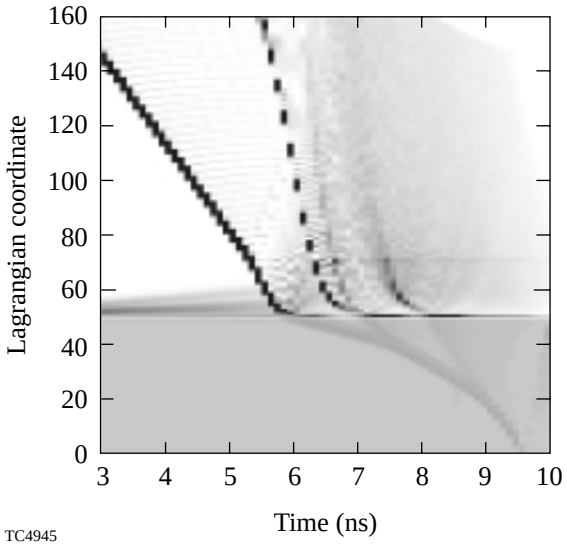

Figure 79.5
Shock propagation as shown by a contour map of the logarithmic derivative of the pressure as a function of time and Lagrangian coordinate. The interface between the DT ice and gas is at Lagrangian marker 50.

increases the shock strength. This puts the main fuel layer onto a higher adiabat and thus reduces the gain. Conversely if the second shock arrives too early, the hot spot produces the burn wave before the main fuel layer has reached peak density and thus reduces the overall target gain. An error in shock timing can arise from the following:

1. Inadequate Control of the Laser Pulse Shape

The $\alpha = 3$ laser pulse shape is essentially defined by eight temporal points as shown in Fig. 79.6. To establish the sensitivity of the target design to variations in pulse shape we performed a series of 1-D calculations. These calculations involved varying the power and temporal position of each point (while holding the other points fixed). By adjusting the last point of the laser pulse we ensured that the overall energy in the pulse remained constant at 1.5 MJ. If a temporal point was adjusted to be in front of another point, that point was removed from the pulse. Figure 79.6 shows the contours of gain generated by moving five of the points. Note that as the first point moves earlier in time (thus lengthening the foot region), the power must drop to preserve target gain; however, reduced foot intensity leads to a weaker shock formation, thus reducing the adiabat of the target and leading to a more unstable implosion. We can see that target performance is sensitive to the foot and transition regions of the laser pulse, but is relatively insensitive to the details of the high-power region. Figure 79.7(a) shows the target gain as a function of a change in the foot power. Figure 79.7(b) shows the target gain as a

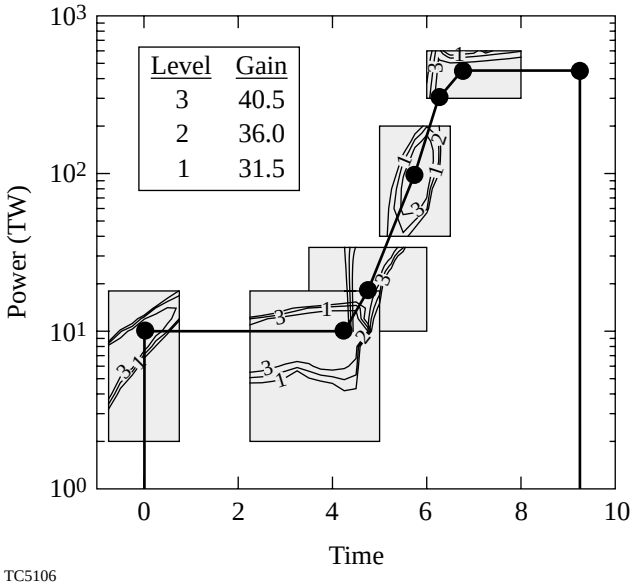

Figure 79.6
The $\alpha = 3$ pulse shape with overlaid contours of gain. The circles correspond to the temporal points used to define the pulse shape. The contours correspond to the gain that would be achieved if the temporal point was moved to that time and power location (holding all other points fixed).

function of the length of the foot region. From these curves it has been established that the pulse power in the foot region must be controlled and measured to ±3%, and that the pulse duration is controlled and measured to ±50 ps. These curves suggest a possible "tuning" strategy for the NIF. By varying the length of the foot (and holding the other portion of the pulse constant) we can scan through the optimal gain region and adjust for uncertainties in the shock transit through the DT ice.

2. Uncertainties in the Target's Equation of State (EOS)

1-D simulations with *SESAME* tables, analytic Thomas-Fermi, and Livermore DT-ice tables have been performed to address the uncertainties in EOS. Using the tuning strategy of foot-length and intensity variations, we can optimize the gain for different EOS models. For example, the optimal gain for targets modeled using the analytic Thomas-Fermi EOS required a 600-ps reduction in foot length from the *SESAME* case. Although we have established that the designs can be retuned to these EOS models, experimental measurements of the EOS of D_2 ice, D_2 wicked foam, and high-Z-doped plastics are required to accurately model the target.

3. Uncertainties in Target Thickness

A series of 1-D simulations have been performed to establish the required control of the DT-ice thickness (which is controlled by the DT-gas-fill pressure). Specifying the control of the ice thickness determines the control and measurement of the fill pressure during ice layering. Figure 79.8 shows the gain as a function of ice-layer thickness (holding the outer radius of the shell fixed). A variation of ±5 μm in a total ice thickness of 340 μm leads to a 2% reduction in gain. This corresponds to a control of the DT-fill pressure of ~20 atm out of a total fill pressure of 1020 atm (at room temperature).

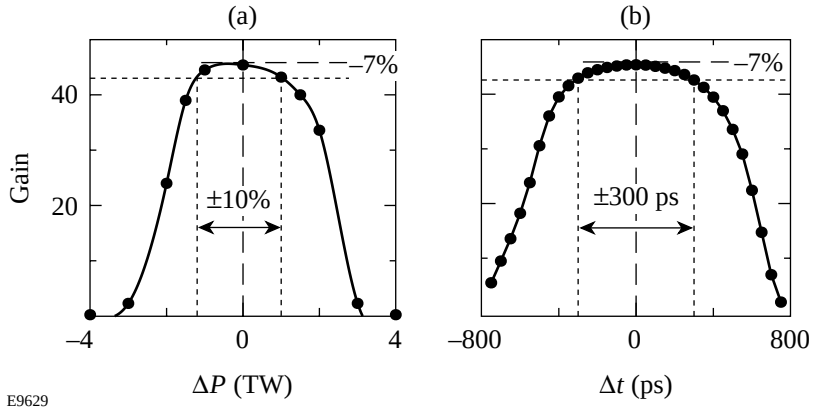

Figure 79.7
The target gain as a function of the change in (a) the foot power and (b) the foot duration from the nominal 10-TW, 4.25-ns parameters.

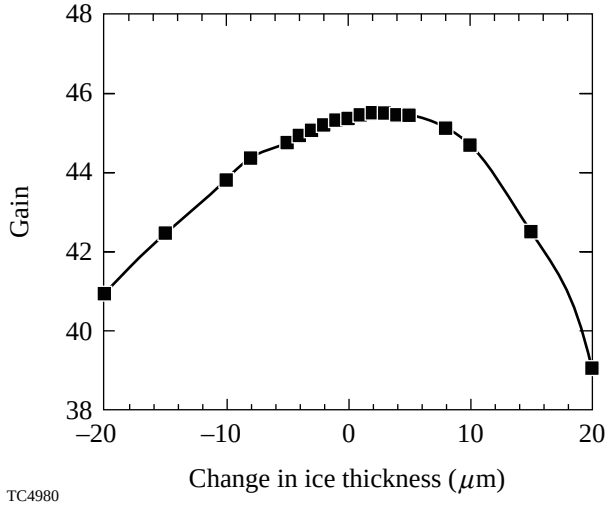

Figure 79.8
The target gain as a function of the change in the ice-layer thickness.

The need to control the hot-electron fraction is similar to the indirect-drive requirements, namely that less than 0.1% of the laser energy is deposited in the DT fuel via hot electrons. Since the laser is more closely coupled to the target in direct drive, however, the transport of hot electrons to the target is more efficient, and the targets are therefore more sensitive to hot electrons than in indirect drive. 1-D simulations were performed with various percentages of laser energy dumped at the critical surface into an 80-keV hot-electron tail. These hot electrons were transported through the target where approximately 4% of the energy absorbed into fast electrons was deposited in the DT-ice fuel layer. Figure 79.9 shows the effect of between 1% and 3% laser energy absorbed into fast electrons on the gain. A 30% reduction in gain occurred when 1% of the incident laser energy was absorbed into fast electrons. The hot electrons are produced by laser–plasma instabilities (LPI's), such as SRS, SBS, and two-plasmon decay.

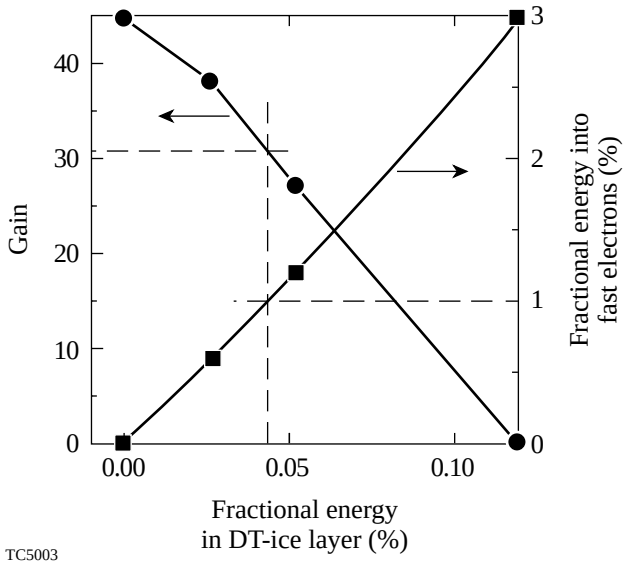

Figure 79.9
The effect of varying the fraction of energy dumped into an 80-keV hot-electron tail on the target gain.

Figure 79.10(a) shows the threshold intensities for SRS and SBS; Fig. 79.10(b) shows the total NIF intensity at the quarter- and tenth-critical surfaces. At each time the minimum threshold in the corona is calculated based on simulations of the $\alpha = 3$ density and velocity profiles. For SRS the threshold is seen to be well above the total NIF intensity at tenth-critical; this is the most relevant density since the minimum thresholds tend to occur far out in the corona where scale lengths are long and densities are low. The single-cluster NIF intensity would be lower by a factor of about 12. For SBS the total intensity is well above threshold after about 6 ns, while the single-cluster intensity is comparable to the threshold. Further study is required to determine how many clusters are likely to participate in driving SBS. SBS has a low threshold at this time because the NIF pulse is rapidly increasing in intensity, producing a local velocity minimum in the density profile and a correspondingly long velocity scale length. These thresholds are calculated on the basis of inhomogeneity scale lengths; the density scale length is the determining factor for SRS and the velocity scale length for SBS. Damping has little effect on the minimum thresholds; the damping contribution depends on the product of the electromagnetic wave damping (mostly collisional, small at low densities) and the electrostatic wave damping (mostly Landau). The Landau damping becomes large for electron-plasma waves (SRS) at low densities and for ion-acoustic waves (SBS) when T_i approaches T_e. The minimum threshold for both instabilities tends to occur at low densities where the small damping of the electromagnetic wave makes the contribution to the threshold negligible. Large Landau damping of the electrostatic waves may, however, substantially reduce growth rates even if the instability is above threshold.

A high level of illumination uniformity is required to achieve ignition. Both direct- and indirect-drive designs require that the targets be driven by pressure nonuniformity levels of less than 1% rms. The angular variation in the intensity distribution on the target is routinely described in terms of spherical-harmonic modes. An ℓ-mode is related to the target radius R and the nonuniformity wavelength λ through $\ell = 2\pi R/\lambda$. The mode spectrum is normally divided into two regions: a low ℓ-mode region ($\ell < 20$) and a high ℓ-mode region ($20 < \ell < 500$). Indirect drive benefits from the conversion of the laser light to x rays. Essentially all modes above $\ell = 10$ are eliminated by x-ray conversion. In direct drive the laser beam alone must achieve the desired level of uniformity; thus, direct drive places much tighter tolerances on the single-beam uniformity and beam-to-beam balance than indirect drive.

Low ℓ-mode (long-wavelength) perturbations are seeded by beam-to-beam variations arising from (1) the mispointing or misfocusing of the laser beams, (2) a lack of energy and power balance, or (3) mispositioning of the target. Such modes grow secularly during the implosion. A simple argument is used to calculate the maximum tolerable variation in the low ℓ-mode spectrum. Since these modes grow secularly, the final distortion δr_f of the compressed fuel at average radius r_f is given by $\delta r_f = \Delta a t^2$, where Δa is the acceleration nonuniformity and t is the implosion time. For a shell initially at radius r_0 the

distortion of the shell is given by $\delta r_f / r_f = \Delta a / a\left(r_0 / r_f - 1\right)$. Numerical calculations using the 2-D hydrocode *ORCHID* suggest that final core distortions of 50% can be tolerated; thus, for a convergence ratio of 25 (which is typical for direct-drive targets), a peak-to-valley acceleration nonuniformity of 2% can be tolerated. The laser nonuniformity in the low ℓ-mode region must be maintained below 1% rms.

The high ℓ-mode (short-wavelength) region is seeded by the structure within the individual laser beam. These modes excite the Rayleigh–Taylor instability, which causes the modes to grow much more rapidly than in the low ℓ-mode region. Note that extremely high mode numbers are not important since they are ablatively stabilized, rapidly saturate, and do not feed through to the hot-spot region.

The effect of the growth of the hydrodynamic instabilities has been examined by two techniques: The first technique uses detailed 2-D *ORCHID* simulations to directly determine the effects of perturbation on target performance. This technique is computationally intensive and does not give the correct 3-D multimode saturation of the RT instability. The second technique uses a postprocessor to the 1-D simulations. This postprocessor uses a self-consistent model[8] to study the evolution of perturbations at the ablation front and the back surface of an accelerated spherical shell. The model includes the ablative Richtmyer–Meshkov (RM),[9] RT, and Bell–Plesset (BP) instabilities; 3-D Haan saturation[10] is included. The model consists of two differential equations (describing the ablation- and inner-surface perturbations) obtained by solving the linearized conservation equations in the DT gas, the shell, and the blowoff plasma regions. The overdense–ablated plasma interface is approximated as a surface of discontinuity.[11]

Direct-drive target designs must tolerate four sources of nonuniformity to ignite and burn: (1) inner-DT-ice roughness, (2) outside CH capsule finish, (3) drive asymmetry, and (4) laser imprinting. Multidimensional simulations of the deceleration phase have shown that our design will ignite when the inner-surface nonuniformity is less than 1.5 μm at the start of the deceleration phase. By performing an extensive series of calculations with various levels of nonuniformity, it is possible to establish the requirements for the four seed terms.

The hardest seed term to establish is that for laser imprint. A series of planar 2-D simulations have been performed using *ORCHID*. These simulations determined the imprint efficiency for single modes of irradiation nonuniformity. The effect of 2-D SSD was included using the approximation

$$\sigma_{\text{rms}} \sim \sqrt{t_c / t}\,,$$

where

$$t_c = \left[\Delta\nu \sin\left(k\Delta/2\right)\right]^{-1}$$

is the coherence time, $\Delta\nu$ is the bandwidth, k is the wave number of the spatial-intensity nonuniformity, and Δ is the speckle size. For example, using a phase-plate nonuniformity spectrum with 1 THz of bandwidth, the laser will imprint a surface nonuniformity equal to σ_{rms} = 360 Å (in modes ℓ < 1000) at the start of the acceleration phase. The additional sources of nonuniformity are then added to that from the laser. For example, Fig. 79.11 shows the mode spectrum of the ablation surface at the start of the acceleration phase for the case of a 1-THz-bandwidth, perfectly uniform outer shell and

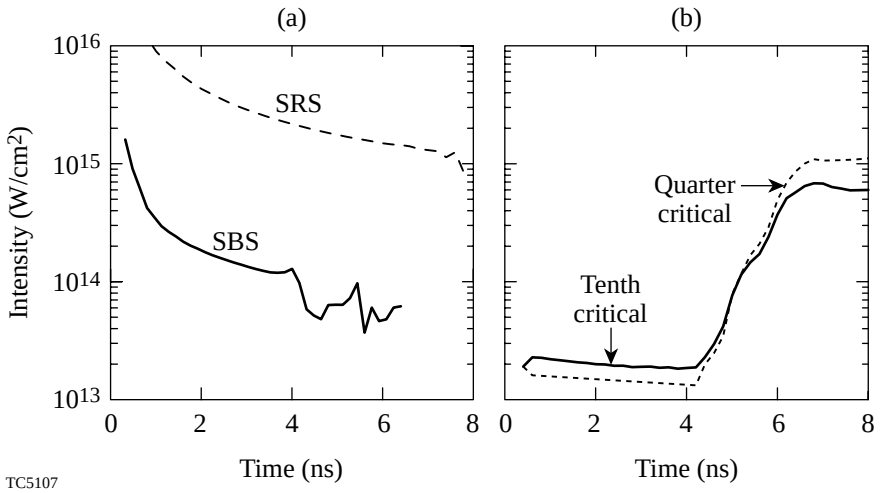

Figure 79.10
(a) The SBS (solid line) and SRS (dashed line) thresholds calculated from the density and velocity profiles as a function of time for the baseline target design. (b) The combined, overlapped beam intensity at the quarter- (dashed line) and tenth-critical (solid line) surfaces as a function of time.

an additional σ_{rms} = 1300-Å perturbation, which has accumulated from the feed-out of 0.5-μm rms from the inner DT-ice layer. Figure 79.11 also shows the mode spectrum of the ablation surface at peak shell velocity, which defines the end of the acceleration phase. The sum of the amplitude of the individual modes gives the total mix width of the ablation-surface instability. Figure 79.12 shows the mix width and the shell thickness as a function of time. In this example we can clearly see that the shell is larger than this mix width, so we conclude that the α = 3 design will survive the acceleration phase when we have 1 THz of bandwidth and 0.5-μm rms of inner DT-ice roughness. At the end of the deceleration phase the total nonuniformity on the inner surface is 1.3 μm, so we would expect this design to ignite.

Figure 79.13 shows the combined effect of different laser-uniformity levels and inner-ice-surface roughness for two different outer-surface finishes on the perturbation amplitude

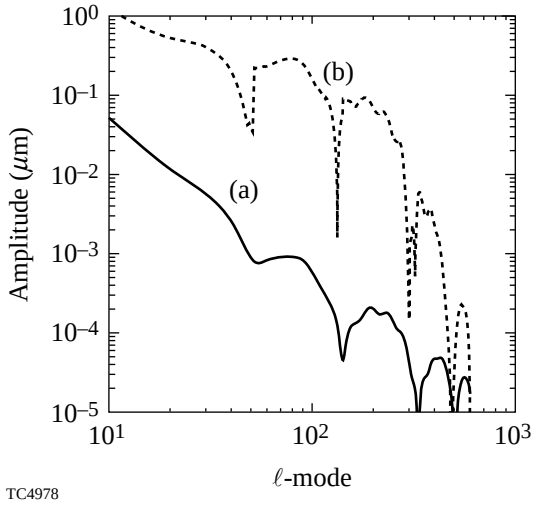

Figure 79.11
The mode spectrum of the outer ablation surface at (a) the start of the acceleration phase and (b) the start of the deceleration phase.

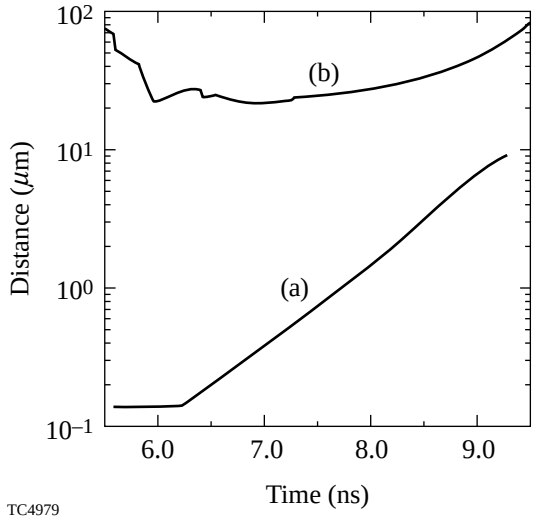

Figure 79.12
The (a) ablation-surface amplitude and (b) the shell thickness as a function of time up to the end of the acceleration phase for the baseline, α = 3, all-DT target design with 1-THz, 2-D SSD and 0.5-μm initial inner surface, DT-ice finish.

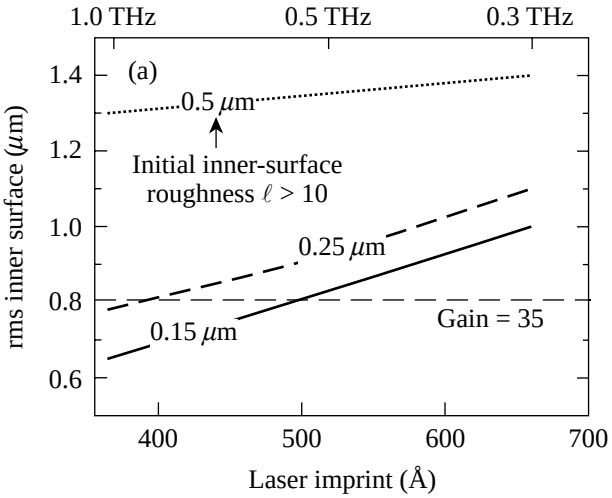

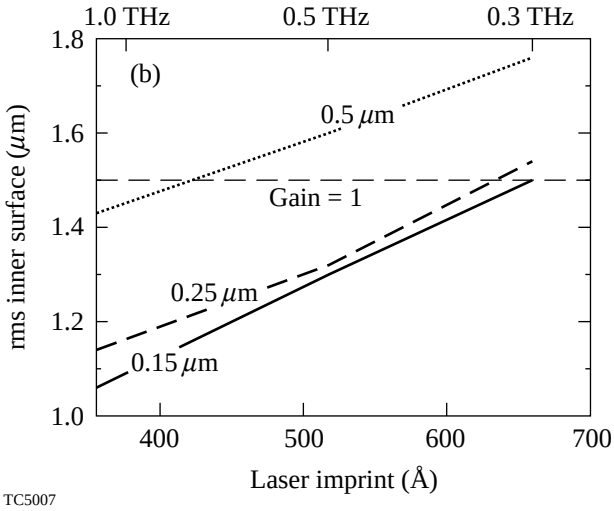

Figure 79.13
The combined effect of laser uniformity and inner DT-ice surface roughness (for modes greater than 10) on the rms inner-surface amplitude at the end of the acceleration phase for (a) 0-Å outer-surface finish and (b) 840-Å outer-surface roughness.

of the inner surface at the time of deceleration. For example, 0.5 THz of bandwidth is equivalent (from *ORCHID* simulations) to 520 Å of initial outer-surface perturbation. This is combined with 0.5 μm of inner-surface roughness and with a perfect outer-surface finish [Fig. 13(a)]. The resultant amplitude at deceleration is 1.35 μm. When there is 840 Å [Fig. 13(b)] of outer-surface roughness, the amplitude of the inner surface at deceleration rises to 1.45 μm. These final amplitudes are very close to the maximum tolerable, so we conclude for safety that for a successful ignition campaign using direct drive we will need 1 THz of bandwidth, < 0.25 μm of DT-ice nonuniformity in mode $\ell > 10$, and < 800 Å of outer-surface perturbation.

Conclusions

Based on the calculations described in the previous section we have established specifications required on the NIF to ensure a successful direct-drive ignition campaign. Table 79.I summarizes these requirements. It should be noted that independent calculations by Weber,[12] using the 2-D *LASNEX* code, confirm our calculations that the $\alpha = 3$ continuous-pulse design will survive the acceleration phase and should achieve ignition.

ACKNOWLEDGMENT

This work was supported by the U.S. Department of Energy Office of Inertial Confinement Fusion under Cooperative Agreement No. DE-FC03-92SF19460, the University of Rochester, and the New York State Energy Research and Development Authority. The support of DOE does not constitute an endorsement by DOE of the views expressed in this article.

Table 79.I: Summary of the specifications for our current modeling of the baseline "all-DT" target design.

Parameter	Requirements
Laser energy	1.5 MJ
Pulse shape	50:1 contrast, 10-ns duration [see Fig. 79.3(b)]
Beam-to-beam power balance	8% in 500 ps
Quad-to-quad power balance (assuming independent quads)	4% in 500 ps
Laser bandwidth	1 THz
Individual beam nonuniformity	3% in 500 ps (all modes)
Outer CH	<2 μm
Outer-surface target finish	<800 Å
Inner DT-ice thickness	340 μm±5 μm
Inner DT-ice-layer uniformity	<0.25 μm ($\ell > 10$) (for $\ell < 10$ exact value to be determined)
Shock-timing accuracy	<50 ps
Preheat	<0.1% of incident laser energy

REFERENCES

1. J. D. Lindl, Phys. Plasmas **2**, 3933 (1995).

2. S. E. Bodner, D. G. Colombant, J. H. Gardner, R. H. Lehmberg, S. P. Obenschain, L. Phillips, A. J. Schmitt, J. D. Sethian, R. L. McCrory, W. Seka, C. P. Verdon, J. P. Knauer, B. B. Afeyan, and H. T. Powell, Phys. Plasmas **5**, 1901 (1998).

3. S. Skupsky, R. W. Short, T. Kessler, R. S. Craxton, S. Letzring, and J. M. Soures, J. Appl. Phys. **66**, 3456 (1989).

4. H. Takabe *et al.*, Phys. Fluids **28**, 3676 (1985); R. Betti, V. N. Goncharov, R. L. McCrory, and C. P. Verdon, Phys. Plasmas **2**, 3844 (1995).

5. M. Tabak, D. H. Munro, and J. D. Lindl, Phys. Fluids B **2**, 1007 (1990); C. P. Verdon, R. L. McCrory, R. L. Morse, G. R. Baker, D. I. Meiron, and S. A. Orszag, Phys. Fluids **25**, 1653 (1982); J. H. Gardner, S. E. Bodner, and J. P. Dahlburg, Phys. Fluids B **3**, 1070 (1991).

6. J. P. Knauer, C. P. Verdon, D. D. Meyerhofer, T. R. Boehly, D. K. Bradley, V. A. Smalyuk, D. Ofer, P. W. McKenty, S. G. Glendinning, D. H. Kalantar, R. G. Watt, P. L. Gobby, O. Willi, and R. J. Taylor, in *Laser Interaction and Related Plasma Phenomena*, edited by G. H. Miley and E. M. Campbell (American Institute of Physics, New York, 1997), Vol. 406, pp. 284–293; J. Knauer, R. Betti, D. K. Bradley, T. R. Boehly, T. J. B. Collins, V. N. Goncharov, P. W. McKenty, D. D. Meyerhofer, V. A. Smalyuk, C. P. Verdon, S. G. Glendinning, D. H. Kalantar, and R. G. Watt, "Single-Mode Rayleigh-Taylor Growth-Rate Measurements with the OMEGA Laser System," to be published in Physics of Plasmas; J. Grun *et al.*, Phys. Rev. Lett. **58**, 2672 (1987); S. G. Glendinning, S. N. Dixit, B. A. Hammel, D. H. Kalantar, M. H. Key, J. D. Kilkenny, J. P. Knauer, D. M. Pennington, B. A. Remington, R. J. Wallace, and S. V. Weber, Phys. Rev. Lett. **78**, 3318 (1997).

7. C. P. Verdon, Bull. Am. Phys. Soc. **38**, 2010 (1993).

8. V. N. Goncharov, "Self-Consistent Stability Analysis of Ablation Fronts in Inertial Confinement Fusion," Ph.D. thesis, University of Rochester, 1998.

9. V. N. Goncharov, Phys. Rev. Lett. **82**, 2091 (1999).

10. S. W. Haan, Phys. Rev. A **39**, 5812 (1989).

11. A. R. Piriz, J. Sanz, and L. F. Ibanez, Phys. Plasmas **4**, 1117 (1997).

12. S. V. Weber *et al.*, *ICF Quarterly Report* **7**, 43, Lawrence Livermore National Laboratory, Livermore, CA, UCRL-LR-105821-97-2 (1997).

Numerical Investigation of Characterization of Thick Cryogenic-Fuel Layers Using Convergent Beam Interferometry

The effect of hydrodynamic instabilities on the performance of inertial confinement fusion (ICF) experiments is well known. Hydrodynamic instabilities affect ICF capsules during the initial acceleration and final deceleration phases of the implosion. Nonuniformities in the applied drive coupled with imperfections at the target surface seed Rayleigh–Taylor (RT) unstable growth at the ablation front. In addition, the shock wave reflecting off a perturbed inner ice surface returns to the ablation region and also seeds the instability (feed-out). These perturbations grow since low-density, ablated material accelerates the unablated, dense shell. Further growth of these perturbations eventually feeds through the shell and couples with existing perturbations on the inner ice surface. Together these seed RT growth at the ice–gas interface when the ice layer begins to decelerate around the spark plug region near the target's center. As the RT instabilities grow, the cold, dense fuel is mixed into the hot core leading to cooling of the core and reduced target performance.

The success of the ICF program depends on targets designed to limit the amount of RT growth to an acceptable value or whose performance is insensitive to the presence of such perturbations. A good understanding of all nonuniformity sources in the implosion is required to design such targets. Nonuniformity sources include the laser or holhraum drive, the coupling of this energy to the target (imprint), and the initial surface finish of both the outer ablator surface and the inner DT ice. To date, significant progress has been made in understanding the role of the first three nonuniformity sources. Characterization of the inner ice surface, however, remains a serious challenge. The ability to accurately characterize this surface is especially critical in light of recent work by Betti[1] in which the feed-out contribution to the ablation region has been shown to be a major factor in overall RT growth during an implosion.

Overview

Cryogenic targets imploded with OMEGA will consist of polymer capsules several micrometers thick with diameters ranging from 900 to 1100 μm. These capsules will be filled with condensed D_2 or DT fuel up to 100 μm thick. Historically, the fuel content and fuel-layer uniformity of cryogenic targets at LLE have been interferometrically characterized using plane-wave illumination.[2–7] A capsule with a thick cryogenic layer condensed on its interior behaves as a strong negative lens, which has several adverse effects on an interferogram created with plane-wave illumination. Computer simulations of typical interferograms are shown in Fig. 79.14. The highly divergent and spherically aberrated wavefront created by the target cannot be effectively collected and imaged by optics with convenient numerical apertures (<0.2), resulting in loss of information near the perimeter of the target's image. Additionally, interfering this highly curved wavefront with a planar reference wavefront results in an interferogram with a fringe spatial frequency that increases radially to very high values near the perimeter of the target's image. The phase sensitivity

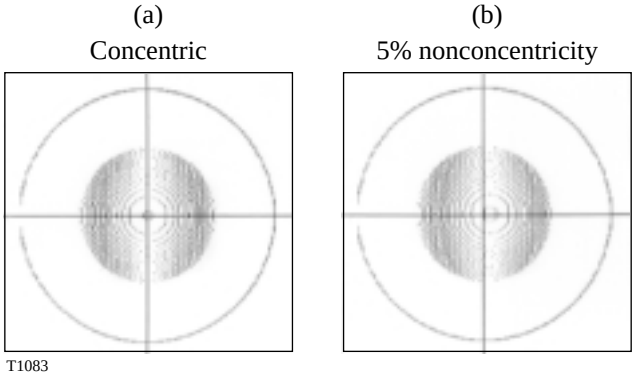

Figure 79.14
Computer-generated interferograms of a 1120-μm-diam, 10-μm-thick capsule that contains 100 μm of condensed fuel. These interferograms were created assuming that both the object and reference beams consisted of planar wavefronts with a 514-nm wavelength, and that *f*/6 optics were used to image the target. All of the surfaces in (a) were perfectly concentric with one another, whereas (b) displays a 5% fuel nonconcentricity, i.e., the center of the spherical inner surface of the condensed fuel layer has been displaced to the right in the figure by 5% of its total thickness. Obviously, a 5% nonconcentricity can be easily detected, but higher-order nonuniformities are much more difficult to detect due to the very high fringe frequency. In addition, information regarding the state of the fuel near the perimeter of the target's image has been lost due to refraction of the object beam outside of the imaging optics' finite collection aperture.

is reduced dramatically when the fringe frequency approaches the Nyquist limit of the detector. As the fringe frequency nears the frequency of pixels in the CCD array, aliasing occurs and the fringes become unresolved.

These limitations can be compensated for by focusing the object beam of a Mach–Zehnder interferometer near the rear focal point of the filled target, causing a nearly collimated beam to emerge. A complete description of this interferometer has been published elsewhere.[8] The optical system used to create an interferogram of a cryogenic target with convergent-beam illumination is shown in Fig. 79.15.

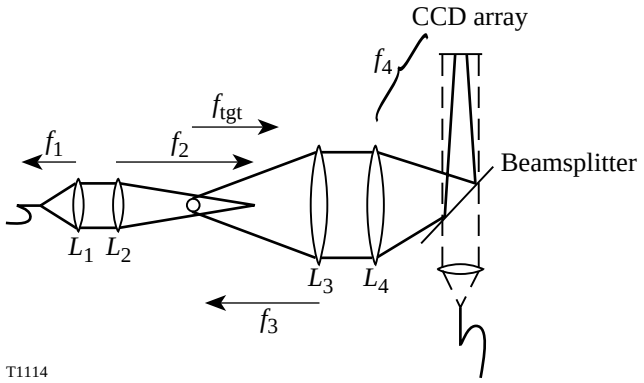

Figure 79.15
Schematic of the optical system used to create an interferogram of a cryogenic target with convergent-beam illumination. The optics that control the point of focus of the convergent beam and those that image the target are shown. The dashed line denotes the collimated reference beam.

Phase sensitivities of the order of a few hundredths of a wave can be achieved by phase-shifting techniques.[9–11] This involves sequentially acquiring multiple interferograms, each with a unique phase offset caused by introducing a slight path-length change in one of the interferometer's arms. The phase of each point in the interferogram is then obtained, modulo 2π, by performing simple mathematical operations on the set of interferograms. One advantage of phase-shifting methods is that the phase resolution depends primarily on the dynamic range of the CCD array and the contrast of the interferogram, not the number of pixels per fringe.

Methodology

Characterizing a nonuniform cryogenic-fuel layer by interpreting the phase of a wavefront perturbed by passing through it is, unfortunately, not straightforward. Evident in Fig. 79.16, the majority of rays traveling through the target have probed two independent ice surfaces on opposite sides of the target. Unique measurement of a perturbation on either surface is impossible without collecting an enormous number of interferograms.

The method we propose is very similar to the technique implemented by Wallace[12] to characterize surface perturbations on the outside of ICF capsules. Data is first collected using atomic force microscopy (AFM) along great circles on the target surface. This information is Fourier-analyzed to produce an average one-dimensional (1-D) power spectrum. The 1-D Fourier power spectrum is then mapped into the two-dimensional (2-D) spherical-harmonic spectrum by using an Abel transformation derived by Pollaine.[13] Pollaine showed that a 1-D Fourier power spectrum, representative of the entire surface, could be transformed into the corresponding 2-D power spectrum using

$$P_{2\text{-D}}(l) = \frac{\mathrm{d}}{\mathrm{d}l}\int P_{1\text{-D}}\left(\sqrt{l^2+n^2}\right)\mathrm{d}n.$$

MacEachern[14] showed that a representative 1-D power spectrum could be obtained by averaging nine independent, experimental 1-D power spectra together. These nine traces are

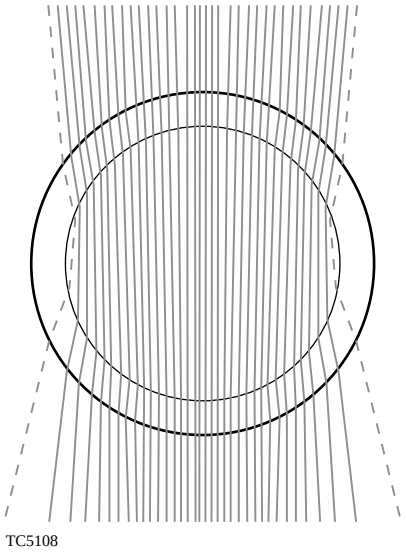

Figure 79.16
Ray trace of an *f*/5 laser through an OMEGA cryogenic capsule. The method uses rays very near the perimeter of the target similar to the dashed rays in the figure. Such rays probe two points on the inner surface, which, when averaged, represent two of the scans used in the outer-surface-measurement technique described in the text.

arranged in groups of three and are taken along great circles that lie on the three orthogonal planes that intersect the target's center. Each set of three traces samples an approximately 40-μm-wide swath on the target's surface. The geometry used in this data-acquisition method is shown in Fig. 79.17 with the three traces within a set labeled A, B, and C.

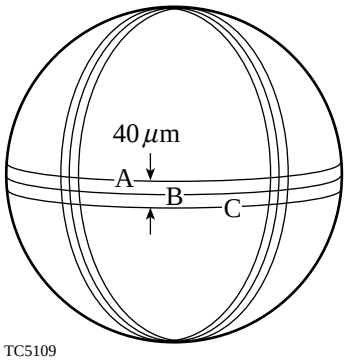

Figure 79.17
Geometry of data-acquisition traces used in the surface-characterization method. Each of the three sets of traces lies along an orthogonal direction on the sphere. The width between outer traces is approximately 40 μm.

Reexamining Fig. 79.16, it can be seen that there is a subset of rays, traveling very near the equator of the target, where a small cord (~40 μm long) probes two points of the inner ice surface. Such a ray is shown dashed in Fig. 79.16. The perturbed optical-path difference (OPD) along this path represents an average at the two positions. Collecting all of these rays from the overall phase map yields a great circle of data, coming out of the paper, sampling the inner ice surface near the equator at this orientation. This is essentially the same as averaging traces A and C in the method described above and shown in Fig. 79.17. The target is rotated and data is collected along several great circles. This data is analyzed using the process described above for characterizing an outer-surface perturbation spectrum.

Implementation

To implement the characterization method described above, the phase of the wavefront passing through the cryogenic target must be acquired by interferometrically measuring the OPD between it and a planar reference wavefront. Eventually, when the cryogenic filling station at LLE is in operation, this information will be provided by measuring real ICF capsules. Initial analysis, however, has been done using synthetic OPD maps produced using the ray-trace simulation code *Ring*s. *Ring*s, which was written by Craxton[15] to simulate three-dimensional (3-D) planar interferometric probes, was modified to provide for a convergent *f*/5 probe at 670 nm. The capsule used in our analysis is equivalent to that of a cryogenic target designed to be used in initial experiments on OMEGA. The capsule consists of a thick shell of DT ice (100 μm) surrounded by a single, thin layer of plastic (1 to 5 μm). Fully independent perturbations can be applied to any or all interfaces within the target. Originally, these perturbations were limited to simple geometric terms of the order of less than 4. Routines have since been added that allow perturbations to be imposed based on their complete spherical-harmonic spectrum. Normalization routines control the total applied ice-surface roughness (rms) and spectral dependency of the modal pattern. Multiple, independent great circles can be simulated by aligning the probe axis with respect to selected points on the target.

Rings determines the intersection of a ray at every physical interface within the target to within 1 Å. Once the intersections are determined, the total optical path is calculated for the transit through the preceding layer. Snell's Law is then applied to produce the proper change in direction cosines for transit into the next layer. *Rings* traces many rays through the target and into a collection optic. The resulting phase map is then projected back to an image plane located at the center of the target, which is conjugate to the detector plane in the actual interferometer.

The OPD map must first be analyzed to identify a radius that corresponds to the inner ice surface. As can be seen in Fig. 79.16, this information is near the very edge of the map. Rays that intersect the target at steeper angles are refracted outside of the collection aperture of the interferometer's *f*/5 imaging system. Once identified, this information is not necessarily uniformly spaced along a circle; it must then be interpolated to a great circle of 2^n evenly spaced points to be analyzed by standard FFT routines. Many interpolation schemes were tested. A solution was found that imports the data into the commercially available graphics package Tecplot.[16] Tecplot runs on Pentium PC's and has extensive capabilities to interpolate data to a variety of physical grids, including evenly spaced circles. The interpolated data is then Fourier-analyzed to recover a 1-D power spectrum. The overall procedure to analyze a given OPD takes only a few minutes per view. It is anticipated that an averaged 1-D power spectrum, evaluating six views (as shown in Fig. 79.18), could be obtained in less than one-half hour. The final step—transforming the averaged 1-D power spectrum into the 2-D spectrum—is accomplished using a Fortran program and requires only a few minutes of computer time.

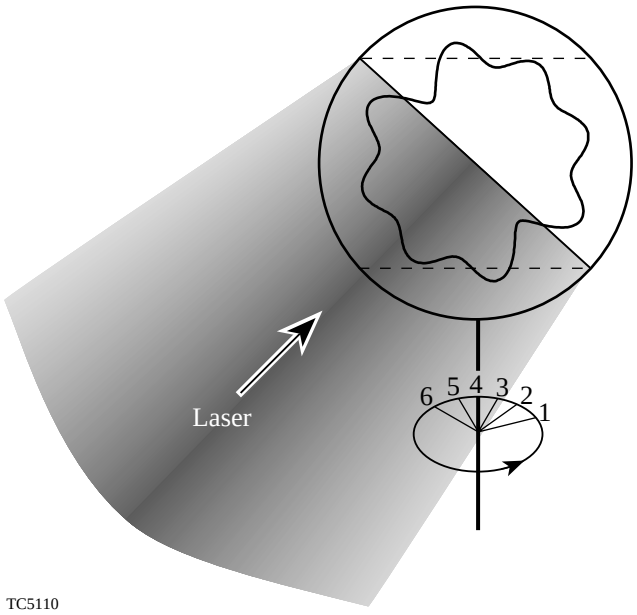

Figure 79.18
Schematic indicating the data-acquisition procedure. The probe laser is incident on the target at an angle of 17.72° below the equator. After collecting data for the position, the target is rotated on-axis 30° and scanned again. The procedure is repeated until six scans are completed.

Numerical Results

The first test of the method described above was to perturb the inner ice layer with pure sinusoidal modes to determine whether the FFT of the great circle of the synthetic OPD would return the applied value. Such a test does not require the Abel transformation. Initially, only single sinusoidal modes ($m = 20$, 40, and 80) were modeled. The results, shown in Fig. 79.19, demonstrate that the method is able to reproduce the applied perturbation quite well. The next step was to perturb the target with a whole spectrum of sinusoidal modes given by

$$R_1 = R_0 + \sum a_0 m^{-1.1} \cos\{m[\varphi + 2\pi b(m)]\},$$

where $a_0 = 0.739\ \mu$m and $b(m)$ is a random number used to distribute random phase among the modes. The result of these tests, shown in Fig. 79.20, indicate that the method is able to recover the applied sinusoidal spectrum very well.

Building on these results, tests were constructed that would more closely match what one would expect in nature. The pertinent values that are required for numerical simulation of ICF capsules are the total rms and the modal dependency of the overall spherical-harmonic spectrum. As such, several examples were constructed using a variety of total roughness and spectral dependency. The applied perturbations took the form

$$R_1 = R_0 + \sum_{\ell=2}^{n} \left(\frac{a_0 \ell^{-\beta}}{\sqrt{2\ell+1}} \sum_{m=-\ell}^{\ell} Y_{\ell,m} \right),$$

where n is the number of applied modes, β is the modal dependence of the applied spectrum, and a_0 has been normal-

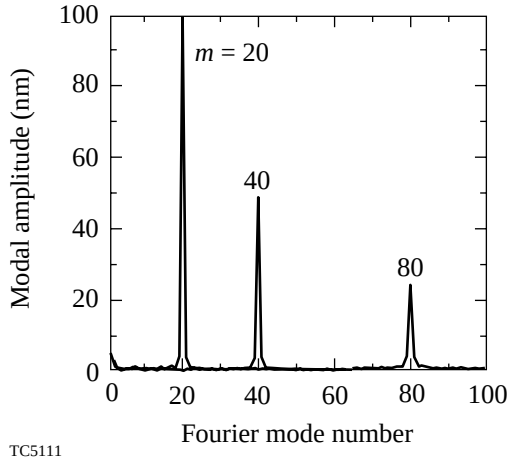

Figure 79.19
Mode amplitudes of OPD determined through ray trace of targets with inner-ice surface perturbed with an individual sinusoidal mode. The amplitudes of the applied perturbations were chosen to scale as 2000/m nm.

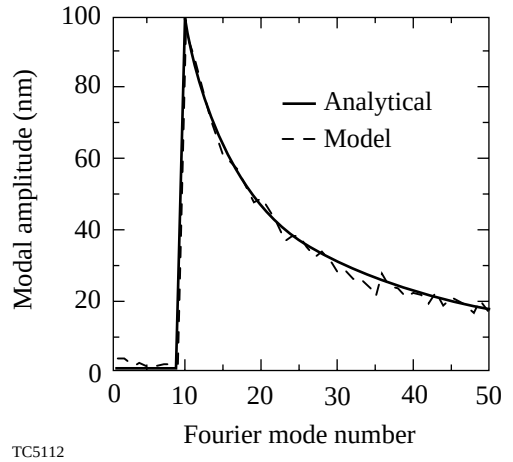

Figure 79.20
Mode amplitudes of OPD determined through ray trace of targets with inner-ice surface perturbed with a spectrum of sinusoidal modes between mode $m = 10$ and $m = 50$. The solid curve represents the exact modal spectrum that was applied to the surface.

ized to return the desired surface rms. The spectral amplitudes were modified in the high-frequency range by applying a Blackman filter[17] to avoid Gibb's phenomenon behavior in the numerical reconstruction of the applied spectrum.

An important point to these calculations is the determination of a cutoff frequency above which any additional modes make little contribution to the overall perturbation at stagnation and, as such, need not be resolved. This cutoff is generally taken to be near mode 50. This cutoff comes from stability arguments of target designs that assume monotonically decreasing perturbation spectra of the order of $\ell^{-\beta}$ at the beginning of the deceleration phase of the implosion. For $\beta = 1.5$, the relative mode amplitudes at about mode 40 and beyond are one to several orders of magnitude lower than the amplitudes of mode numbers below 10. When Haan saturation effects[18] are considered, however, it can be shown that such a cutoff is applicable for perturbation spectra that are even flat ($\beta = 0$) at the onset of deceleration (see Appendix A). Therefore, our analysis, while examining targets with perturbations using modes 2 to 192, resolves only the modal region of the ice roughness between modes 2 and 50.

Similar to the above sinusoidal perturbation tests, our first test with spherical harmonics was to perform an analytical check of the method. Knowing the analytic form of the perturbation spectrum placed on the inner ice layer, we could immediately take the Fourier transform of the resulting perturbed radius representing the inner target equator. This 1-D power spectrum was then transformed to give back the applied 2-D spectrum. The results of this case are shown in Fig. 79.21, where it can be seen that the method gives very good reconstruction of the applied spectrum except in the very high frequency range. Here the method experiences slight trouble in reconstructing the spectrum. The numerical results here are being strongly influenced by the unphysical termination of the spectrum. The results of this test confirmed that a good approximation of the 2-D spectrum of the inner ice surface could be obtained from ray-trace data that correctly maps a great circle of the inner ice surface.

We then examined ray-trace tests that spanned both the rms of the surface and the modal dependency of the spectrum. The results of one of these tests are reported here. When the spherical harmonics are applied, the amplitude of all *m*-components of a particular ℓ-mode is assumed constant. Additionally, a base-line total rms value used here is defined to include only the power in modes 10 to 50. Several examples, comparing the numerically obtained modal amplitude spectrum with the exact applied perturbation, are shown in Fig. 79.22. The

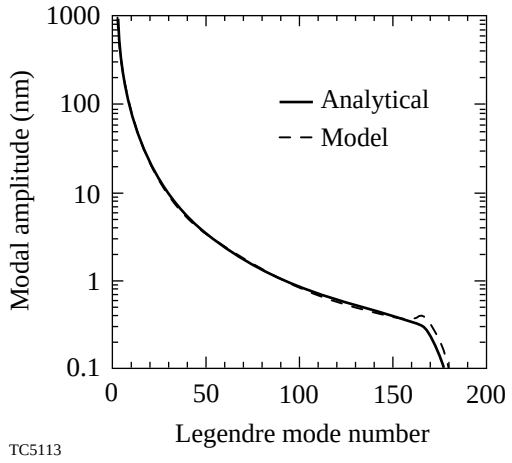

Figure 79.21
Evaluation of an analytical representation of a spherically perturbed inner ice surface. The solid curve represents the exact modal spectrum applied to the surface. The dashed curve is obtained by taking the FFT of the perturbed radius and transforming the 1-D power spectrum into the 2-D power spectrum. Except for the high-frequency regime, the method can be very accurate in resolving the 2-D applied perturbation using 1-D data.

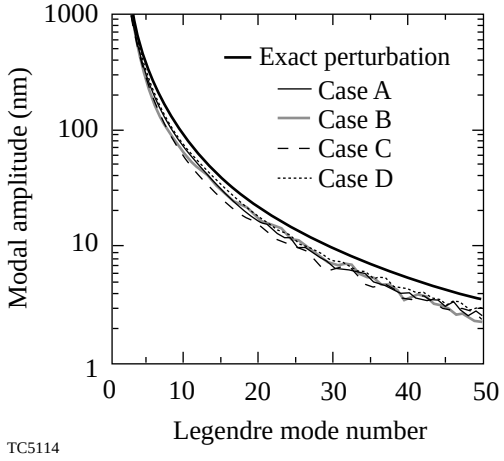

Figure 79.22
Comparison of several ray-trace evaluations of an OMEGA cryogenic capsule with a spherically perturbed inner ice surface. The thick solid curve represents the exact modal spectrum applied to the inner surface. The other curves are obtained by averaging a set (six numerical ray traces) of 1-D power spectra of perturbed OPD and then transforming that average into the 2-D power spectrum. Each curve represents the resulting modal amplitudes obtained at a separate orientation on the target. These orientations are given in Table 79.II.

capsule was perturbed with a full spectrum of modes from $\ell = 2$ to $\ell = 192$. The baseline total rms was set to be 0.25 μm with a spectral parameter $\beta = -1.5$. Four tests (Cases A–D) were performed, representing the acquisition of data at different spherical orientations on the capsule. Each case used six acquired ray traces taken about the capsule to produce the average 1-D power spectrum for the analysis. The spherical orientations are given in Table 79.II. Examining Fig. 79.22, it can be seen that each of the tests provides a very good representation of the modal dependency of the applied perturbation. Case B recovered 89% of the total rms defined from modes 2 to 50, while Case C recovered only 73%. From these results, it can be seen that the method provides good resolution of the perturbations on the inner ice surface.

Future Work

The method we have described will provide a detailed analysis of the inner-ice-surface roughness; however, more work must be performed to determine the sensitivity of the method under a variety of physical constraints. Aberrations in the wavefront caused by the optical system have not been included in the model so far. These can potentially be subtracted from the target's phase map by taking a phase map of the wavefront passing though the interferometer without a target present. The shot noise and finite resolution of the CCD array detector (i.e., their role in limiting the phase sensitivity of the interpolation routine) should also be examined. Finally, the limitation that perturbations on the surfaces of the capsule impose on the sensitivity of ice-surface measurements should be examined.

ACKNOWLEDGMENT

This work was supported by the U.S. Department of Energy Office of Inertial Confinement Fusion under Cooperative Agreement No. DE-FC03-92SF19460, the University of Rochester, and the New York State Energy Research and Development Authority. The support of DOE does not constitute an endorsement by DOE of the views expressed in this article.

Appendix A

To determine the critical modes that make up the perturbed interface between the cold, dense fuel and the hot spark-plug region, the RT growth that all modes experience during the deceleration phase in an ICF implosion must be examined. We start by assuming a modal dependency between the modes that is of the form

$$\sigma_\ell = \frac{C_1}{\ell^\beta}.$$

Given the total surface perturbation σ_{rms}, one can integrate over the modes (from 2 to 500) to arrive at the constant C_1 as

$$C_1 = \frac{\sigma_{\text{rms}}}{\sqrt{\sum \frac{1}{\ell^{2\beta}}}}.$$

Lindl[19] has shown that during deceleration any unsaturated modes will grow roughly as

$$a_\ell^{\text{lin}} = \left(a_\ell\right)_0 e^\eta,$$

where

$$\eta = \sqrt{\frac{2\ell}{1 + 0.2\ \ell}}.$$

One can see that η asymptotes quickly to the value $\eta \cong \sqrt{10}\ (\sim 3)$ at about mode 20. As such, in the absence of saturation, all modes above 20 will grow roughly the same. If one assumes the initial perturbation spectrum to be comparable to the initial ice surface, the spectral parameter β can be set to be ~1.5. While most of the modes will grow the same, the final amplitudes of modes greater than 40, as shown in Fig. 79.A1, are relatively

Table 79.II: Orientation angles used in numerical ray-trace tests. Cases A and B represent scans at two orthogonal positions on the sphere. Case C was chosen as a neutral position between A and B. Finally, Case D is for scans along the optical axis proposed for the experimental characterization station at LLE.

	Orientation Angles (θ,Φ)					
Case	Scan 1	Scan 2	Scan 3	Scan 4	Scan 5	Scan 6
A	90, 0	90, 30	90, 60	90, 90	90, 120	90, 150
B	90, 90	60, 90	30, 90	0, 90	30, 180	90, 150
C	90, 0	75, 30	60, 60	45, 90	60, 120	75, 150
D	72.28, 0	72.28, 30	72.28, 60	72.28, 90	72.28, 120	72.28, 150

very small. As such, these modes lend no significant contribution to the overall perturbation at stagnation; however, the initial spectrum involved must also include contributions from perturbations feeding through from the ablation surface. These perturbations will add in quadrature with the ice layer, and the resulting perturbation rms will probably no longer obey $\beta = 1.5$. As shown in Fig. 79.A1, the final amplitude spectrum of these perturbations increases monotonically with decreasing β. While it is hard to conceive of β ever being negative, having β approach zero must be considered.

Of course, as the spectral parameter does approach zero, more power is shifted out of the low-order modes and into the higher-frequency modes. These modes will then become candidates for saturation. Haan has shown[18] that, for a specific mode, as the amplitude approaches its saturation amplitude

$$\left(a_\ell^{\text{sat}} = \frac{2R}{\ell^2}\right),$$

its RT growth undergoes a transition and stops growing exponentially. The amplitude of this perturbation then grows linearly in time and is given by

$$a_\ell = a_\ell^{\text{sat}}\left[1 + \ln\left(\frac{a_\ell^{\text{lin}}}{a_\ell^{\text{sat}}}\right)\right].$$

Therefore, such modes will grow much slower than unsaturated ones and will not contribute significantly to the overall perturbation at stagnation.

A threshold for saturation can be calculated by comparing the Haan saturation amplitude at a given radius to the given perturbation rms at that point:

$$\frac{2R}{\ell_c^2} = \sqrt{\frac{4\pi}{(2\ell_c + 1)}}\,\sigma_\ell = C_1\sqrt{\frac{4\pi}{(2\ell_c + 1)}}\,\ell_c^{-\beta},$$

where ℓ_c is defined as the modal saturation threshold. Performing some algebra, assuming $2\ell_c >> 1$, and defining

$$C_2 = \frac{2}{\sqrt{2\pi C_1}},$$

we have

$$\ell_c = (RC_2)^{1/(1.5-\beta)}.$$

Assuming $R \sim 200$ μm, we can graph the saturation threshold for a variety of initial perturbation rms and spectral parameter β. Such results are plotted over the spectral behavior in Fig. 79.A1. From this graph it can be seen that for β below 1.0, saturation can be expected to play a role in determining the perturbation spectrum at stagnation. For values of β above 1.0, saturation no longer aids in limiting the growth of modes below 100; however, as was pointed out above, in this regime the modal amplitudes fall off quickly with increasing mode number and, as such, will not contribute at stagnation.

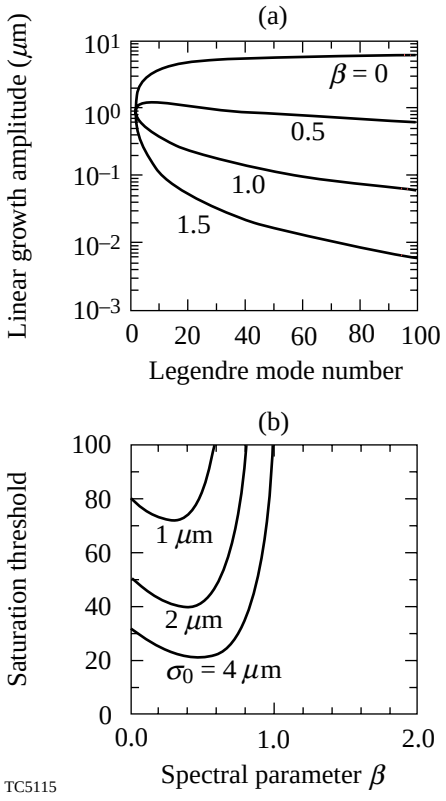

Figure 79.A1
(a) Final linear-growth-amplitude spectrum of perturbations with initial amplitudes of the form $\sigma_\ell = C_1/\ell^\beta$. Here C_1 has been normalized to give 1 μm at $\ell = 2$ for all cases of β. (b) Saturation threshold (mode number) for various cases of total σ_{rms} as a function of the spectral parameter β. Note that for $\beta > 1$, only modes $\ell > 100$ are candidates for saturation. As the initial spectrum flattens and more power is shifted from lower mode numbers into higher ones, modes above $\ell = 20$ can become candidates for saturation. As β falls below 1.0, saturation can be expected to play an increasing role in determining the final perturbation spectrum at stagnation.

A fully integrated measure of the importance of the modal spectrum can be attained by examining the mode number at stagnation at which the integral of power up to that mode represents 95% of the total perturbed power. A full stability analysis was performed for a variety of spectral parameters β and initial perturbation rms to obtain such a cutoff. The results, shown in Fig. 79.A2, clearly show that, for expected values of β (0.5 to 1.5), 95% of the total power resides in modes less than 50. For values of β below 0.5, the cutoff mode number does climb above 50, but it is well contained below mode 100 for expected rms values.

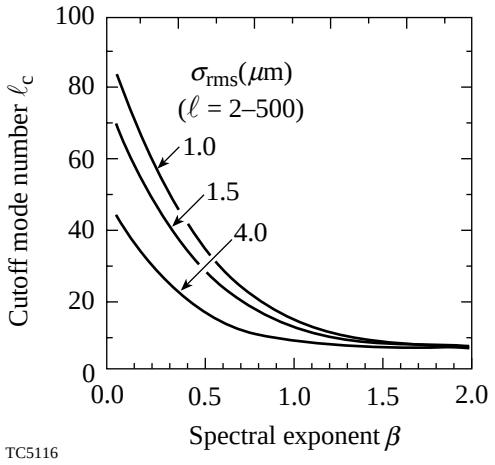

Figure 79.A2
Cutoff mode number at stagnation at which the integral of perturbed power up to that mode represents 95% of the total perturbed power. For expected values of total σ_{rms} (0–4 μm) and β (0.5–1.5), 95% of the total power resides in modes less than 50. For values of β below 0.5 the cutoff mode number does climb above 50, but it is well contained below mode 100 for expected rms values.

REFERENCES

1. R. Betti, V. Lobatchev, and R. L. McCrory, Phys. Rev. Lett. **81**, 5560 (1998).
2. J. A. Tarvin *et al.*, in *Interferometry*, edited by G. W. Hopkins (SPIE, Bellingham, WA, 1979), Vol. 192, pp. 239–243.
3. T. P. Bernat, D. H. Darling, and J. J. Sanchez, J. Vac. Sci. Technol. **20**, 1362 (1982).
4. K. Kim *et al.*, J. Vac. Sci. Technol. A **3**, 1196 (1985).
5. K. Kim and D. L. Krahn, J. Appl. Phys. **61**, 2729 (1987).
6. T. R. Pattinson and W. J. Felmlee, J. Vac. Sci. Technol. A **6**, 1882 (1988).
7. H. J. Kong, M. D. Wittman, and H. Kim, Appl. Phys. Lett. **55**, 2274 (1989).
8. Laboratory for Laser Energetics LLE Review **58**, 83, NTIS document No. DOE/SF/19460-17 (1994). Copies may be obtained from the National Technical Information Service, Springfield, VA 22161.
9. K. Creath, in *Surface Characterization and Testing*, edited by K. Creath (SPIE, Bellingham, WA, 1986), Vol. 680, pp. 19–28.
10. K. Kinnstaetter *et al.*, Appl. Opt. **27**, 5082 (1988).
11. K. Creath, in *Progress in Optics XXVI*, edited by E. Wolf (North-Holland, Amsterdam, 1988), pp. 351–393.
12. S. M. Pollaine, S. P. Hatchett, and S. H. Langer, *ICF Annual Report 1994*, 87, Lawrence Livermore National Laboratory, Livermore, CA, UCRL-LR-105820-94 (1994).
13. R. J. Wallace, R. L. McEachern, and W. W. Wilcox, *ICF Annual Report 1994*, 79, Lawrence Livermore National Laboratory, Livermore, CA, UCRL-LR-105820-94 (1994).
14. R. L. McEachern, C. E. Moore, and R. J. Wallace, J. Vac. Sci. Technol. A **13**, 983 (1995).
15. R. S. Craxton, LLE, unpublished.
16. Tecplot Data Visualization Software, ©1996 by Amtec Engineering, Inc., P.O. Box 3633, Bellevue, WA 98009-3633.
17. A. V. Oppenheim and R. W. Schafer, *Discrete-Time Signal Processing* (Prentice-Hall, Englewood Cliffs, NJ, 1989).
18. S. W. Haan, Phys. Rev. A **39**, 5812 (1989).
19. J. D. Lindl, *Inertial Confinement Fusion: The Quest for Ignition and Energy Gain Using Indirect Drive* (Springer-Verlag, New York, 1998), pp. 66–67.

Studies of Target Implosion Using *K*-Shell Absorption Spectroscopy of an Embedded Titanium Layer

In laser-imploded target studies, the measurement of shell compression and uniformity is essential to understand target performance. Previously we have used targets in which a titanium-doped layer was incorporated into the target shell. The doped layer provided a variety of diagnostic signatures (absorption lines, *K*-edge absorption, Kα imaging) for determining the areal density and density profile of the shell around peak compression.[1–5] In this article we apply some of these methods to demonstrate the improvement in target performance when implementing SSD[6] (smoothing by spectral dispersion). In particular, we study slow-rising laser pulses (for low-adiabat implosions), where the effect of SSD smoothing is more pronounced. In addition, we introduce a new method for studying the uniformity of imploded shells: using a recently developed[5] pinhole-array x-ray spectrometer we obtain core images at energies below and above the *K*-edge energy of titanium. The nonuniformity of such images depends on the nonuniformity of both the emitting core and the absorbing shell; however, the ratio between the images above and below the *K* edge essentially depends on the nonuniformity of the shell alone. Finally, we compare the results with those of 1-D *LILAC* simulations, as well as 2-D *ORCHID* simulations, which allow for the imprinting of laser nonuniformity on the target. The experimental results are replicated much better by *ORCHID* than by *LILAC*.

Areal-Density Measurement Using *K*-Shell Absorption

To demonstrate the effect of SSD on target performance we chose two pairs of laser shots from two different series; for each pair all conditions were nearly identical except for the presence of SSD. The target and laser conditions for these shots are listed on the first four lines of Table 79.III. The two target shots with SSD are almost identical as are the two shots without SSD and they can be used interchangeably. The pulse shape in these four shots was the 2.5-ns, slow-rising pulse shape ALPHA306: starting with a flat, 0.5-ns foot at 2.5% of the peak, followed by a 1.1 ns of a slowly rising ramp, then a 0.2 ns of a faster-rising ramp, it finally reaches a 0.7-ns flat top. This pulse has been shown to place the colder part of the shell during the laser irradiation of typical CH shells on an adiabat of $\alpha \sim 3$. It is particularly suitable for studying the effect of SSD smoothing on reducing imprinting because faster-rising pulses cause early decoupling of laser and shell, which reduces the imprint even without SSD. All four targets were voided, to

Table 79.III: Experimental parameters for the laser shots discussed in this article. The first four shots demonstrate improvement in performance due to SSD; the fifth shot is discussed in the last section of this article. All shots had a Ti-doped layer embedded in the shell (atom concentration of Ti is given in brackets). ALFA306 is a slow-rising, 2.5-ns pulse shape.

Shot No.	Inner radius (μm)	Inner CD layer (μm)	CH(Ti) layer (μm)	Outer CH layer (μm)	Total shell thickness (μm)	Fill gas (atm)	2-D SSD bandwidth (Å)	Pulse shape	Laser energy (kJ)
13151	444.5	5.8	4.8 (4%)	14.3	24.9	void	1.25 × 1.65	ALFA306	21.0
13152	445.0	5.7	5.1 (4%)	14.3	25.1	void	–	ALFA306	21.7
13936	448.5	5.0	5.7 (4.3%)	15.7	26.4	void	1.28 × 1.7	ALFA306	19.5
13939	442.5	5.0	5.7 (4.3%)	15.7	26.4	void	–	ALFA306	22.6
15156	438.5	0.8	2.6 (6.2%)	16.6	20.0	DD (3)	1.26 × 1.76	1-ns square	26.2

resemble the implosion of future cryogenic targets. The structure of the targets was chosen so that the doped layer would become nearly identical with the cold layer at peak compression. The thickness of the overcoat CH layer was chosen so as to be ablated away during the laser pulse; indeed, the laser burned through it toward the end of the pulse. The inner layer was thick enough to constitute the hot, compressed core. This conclusion is based on the observation of Ti plasma lines emitted at the center of the target. In the last section we describe measurements of shell nonuniformity obtained with a different pulse shape: a 1-ns square pulse.

The x-ray spectra were recorded by a space-resolving, time-integrating spectrograph and a streak spectrograph. The first spectrograph used a Ge(111) crystal and a 25-μm-wide spatially resolving slit. The continuum core emission was clearly visible above the much-weaker radiation of larger extent from the interaction region (see Fig. 4 in Ref. 3; also, Fig. 79.28 below); thus, for measuring the absorption of core radiation within the shell, the radiation from the interaction region can be easily subtracted. The crystal calibration curve (see Fig. 4 in Ref. 1) is relatively flat in the 3- to 6-keV region. The streak spectrograph used a RbAP crystal with the image recorded on film. The sensitivity of the film is determined with a density wedge developed simultaneously with the data; however, because the photocathode is not uniformly sensitive across its surface, we used the streak data to monitor the temporal changes but the areal-density determinations relied on the time-integrated spectra. This point is further discussed below.

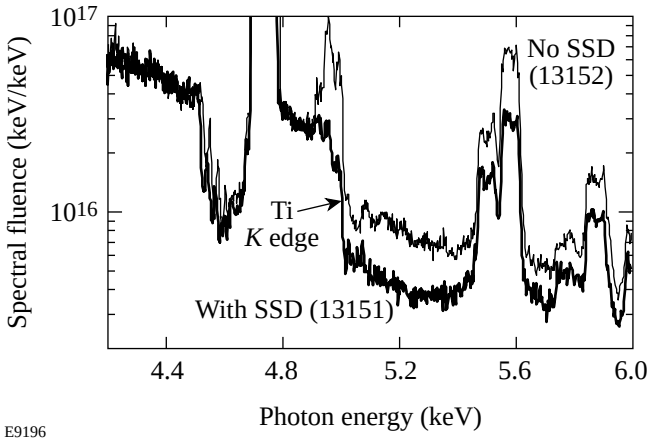

Figure 79.23
Comparison of spectra from two shots (conditions listed in Table 79.III). The main difference is the larger drop above the *K* edge of Ti (around ~ 5 keV) due to SSD smoothing, indicating a higher cold-shell areal density.

Figure 79.23 shows a comparison of the calibrated, time-integrated spectra from shots 13151 and 13152. Figure 79.24 shows lineouts through the streak spectrum for shot 13152 at three different times; the streak spectra for shot 13151 are qualitatively similar. The upper spectrum is emitted during the laser irradiation, and the lower two spectra are emitted at two instances during the compression; the complete record shows that when the laser irradiation terminates, the x-ray emission falls and then rises again during compression. For clarity, the upper curve in Fig. 79.24 was raised by 30. Figure 79.24 clearly shows that the lines of highly ionized Ti ions are emitted during the laser irradiation; their large width (in both Figs. 79.23 and 79.24) is due to source broadening, corresponding to emission from the laser-interaction region. This is also evident from the spatially resolved spectra (e.g., see Fig. 79.28 below). Figure 79.23 shows a higher intensity of these Ti lines when SSD was not implemented. This is consistent with the results of burnthrough experiments[7] that show a faster burnthrough when SSD is absent, due to a higher level of laser imprint.

Turning to the core emission, we see that continuum radiation from the imploded core (formed by the inner layer of the shell) is absorbed when traversing the cold titanium-doped layer. Two types of absorption are evident: 1*s*–2*l* absorption lines in Ti ions with successive *L*-shell vacancies (around

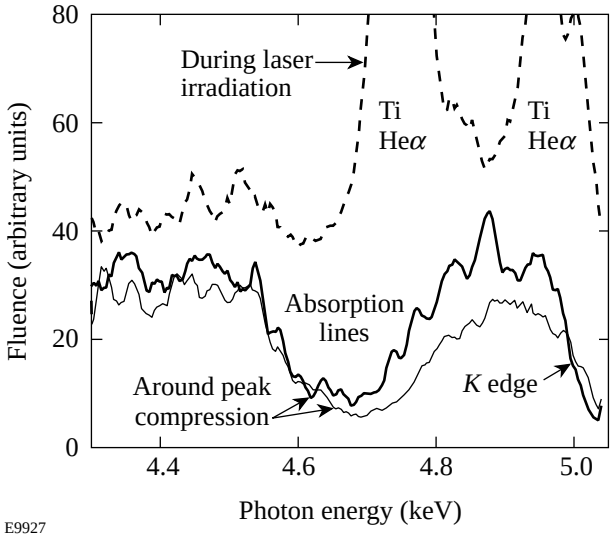

Figure 79.24
Lineouts through the streak spectrum at three different times. The upper spectrum is emitted during the laser irradiation, the lower two spectra at different instances during the compression. Ti lines are seen to be emitted during the laser irradiation. The absorption lines and *K*-edge absorption are seen to occur simultaneously. For clarity the upper curve was raised by 30.

4.6 keV) and Ti *K*-edge absorption (at ~5 keV). We show in the next section that the lines are absorbed in a layer of temperature in the range of ~200 to ~400 eV surrounding the core (the "cool" shell layer), whereas the radiation above the Ti *K* edge is absorbed in a colder layer of temperature in the range of ~150 to ~220 eV surrounding the former layer (the "cold" shell layer).

The drop in intensity across the Ti *K* edge yields the areal density of the titanium alone, using standard tables of absorption in titanium foils; calculations[8] show that at higher temperatures, when *M*- and *L*-shell electrons are successively removed, the *K* edge shifts to higher energies but at a given energy above the edge the absorption hardly changes with ionization. The intensity ratio $R_K = I(< E_K)/I(> E_K)$, where $< E_K$ means an energy just below and $> E_K$ just above the Ti *K* edge, is related to the difference in opacity $\Delta\tau = \tau(> E_K) - \tau(< E_K)$: $R_K = \exp(\Delta\tau)$. More precisely, this value is used as an initial guess in calculating the spectrum above the *K* edge before its absorption and adjusting it to join smoothly the measured spectrum below the *K* edge (see Fig. 6 in Ref. 1). For shot 13151 (with SSD) the Ti areal density is found to be 1.7 mg/cm^2, and for shot 13152 (without SSD) it is 0.78 mg/cm^2. Knowing the Ti concentration, the areal density of the cold doped layer is found to be 7.3 mg/cm^2 and 3.4 mg/cm^2, respectively. These values of $\rho\Delta R$ were obtained from the time-integrated spectra because of their higher spectral resolution as compared with the streak-spectra data; however, the streak data provide additional support for these results. During the time when the core emission is intense, the absorption seen in the streak data does not change appreciably so that the peak $\rho\Delta R$ does not exceed the average $\rho\Delta R$ by more than a factor of ~1.3. It should be noted that the background continuum emitted by the laser-interaction region is distinct from the core continuum in both time and space. Thus, in determining the continuum absorption the background can be removed through either time resolution or space resolution (see Fig. 4 in Ref. 3).

In addition to the *K*-edge absorption, the absorption lines around 4.6 keV yield the areal density of the cool region. Using the method explained in Ref. 9 and used in Ref. 1, we derive ~3.5 mg/cm^2 for the $\rho\Delta R$ of that region. The total areal density of the doped layer is the sum of the $\rho\Delta R$ derived from the *K*-edge absorption and the $\rho\Delta R$ derived from the absorption lines since, as Fig. 79.24 shows, *the two absorptions for the most part occur simultaneously*. Thus, the total areal density of the doped layer with and without SSD becomes 10.8 mg/cm^2 and 6.9 mg/cm^2, respectively. Applying a correction derived from the streak spectra, the *peak* $\rho\Delta R$ *values* are ~14 mg/cm^2 and 9 mg/cm^2, respectively. The uncertainty in these values is ±25%.

Figure 79.23 shows that, whereas the *K*-edge jump differs appreciably for the two spectra, the line absorption as well as the core continuum emission is very similar. The two are related because the lines are absorbed on the fringes of the hot core; thus, the energy dumped into the core depends more on the absorbed laser energy and less on the irradiation uniformity.

The total areal density of the compressed shell can be obtained approximately by multiplying the measured $\rho\Delta R$ of the doped layer by a factor $Q = (\rho\Delta R)_{0,\text{unablated}}/(\rho\Delta R)_{0,\text{doped}}$, where $(\rho\Delta R)_{0,\text{ unablated}}$ is the areal density of the part of the shell that is not ablated (i.e., is imploded) and $(\rho\Delta R)_{0,\text{doped}}$ is the areal density of the doped layer, both in the initial target. The former is known from burnthrough experiments.[7] To demonstrate the validity of this procedure we show in Fig. 79.25(a) the *LILAC*-calculated ratio $R = \rho\Delta R(\text{shell})/\rho\Delta R(\text{doped layer})$ as a function of time for various separations *S* of the doped layer from the inner shell surface (in the original target). For each curve the target is that of shot 13151, except that *S* was assigned a different value in each case. The calculated shell $\rho\Delta R$ is also shown (the peak $\rho\Delta R$ is ~0.5 g/cm^2). During the first 3 ns of the pulse the ratio *R* decreases because of ablation but during the following compression, especially for $S \sim 1$ μm, it changes only slightly. Since an outer layer of about 13 μm is ablated in shot 13151, the value of *Q* is ~2.5; as Fig. 79.25(a) shows, when $S \sim 1$ μm, this value, when multiplied by the measured doped-layer $\rho\Delta R$, would yield the correct total shell $\rho\Delta R$ at peak compression. Thus, for targets with $S < 1$ μm the procedure would overestimate the total shell $\rho\Delta R$, whereas for $S > 1$ μm it would underestimate it. We further calculate *R* by a model that assumes a constant-density shell that converges radially without compression. Figure 79.25(b) shows the results as a function of the compression ratio; the various curves correspond to the curves of Fig. 79.25(a). The initial target in Fig. 79.25(b) is a 12-μm-thick shell, which corresponds to the unablated target in shot 13151. As seen, the corresponding curves in the two figures are very similar, even though the $\rho\Delta R$ values in the incompressible model are much smaller than in the *LILAC* calculations. This indicates that the procedure is insensitive to the details of the implosion.

The separation of the doped layer in the targets listed in Table 79.III is larger than the optimal; thus, this method will underestimate the total shell $\rho\Delta R$ by about a factor of 2. Since

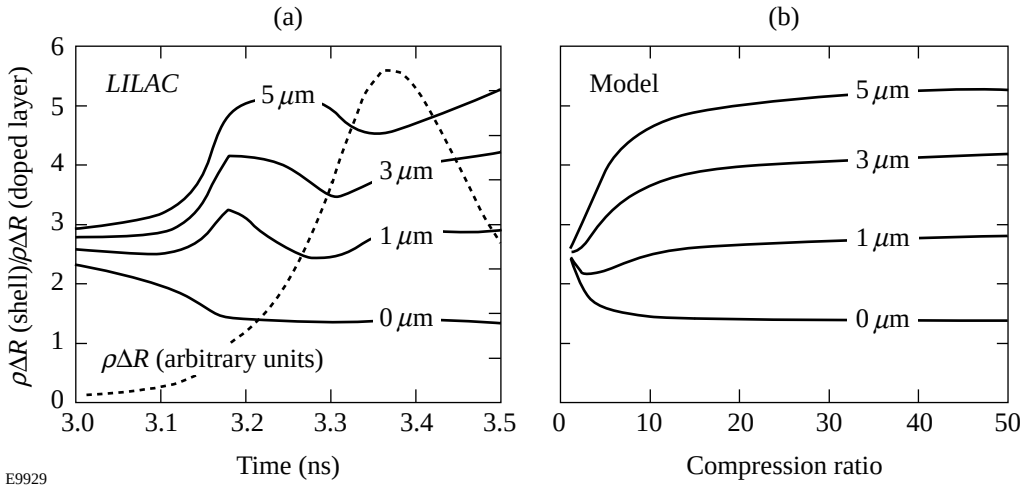

Figure 79.25
The calculated ratio $R = \rho\Delta R(\text{shell})/\rho\Delta R(\text{doped layer})$ for various separations S of the doped layer from the inner shell surface (in the original target). (a) *LILAC*-calculated R as a function of time; the curves correspond to shot 13151 except that S is different for each curve. The calculated shell $\rho\Delta R$ is also shown. (b) Model-calculated R as function of compression ratio; the initial target is assumed to correspond to shot 13151 after the ablation (of 13 μm CH) has been completed.

the value of Q is ~2.5 for the shots of Fig. 79.23 and accounting for this factor-of-2 underestimate, the total shell $\rho\Delta R$ is found to be 70 mg/cm^2 for shot 13151 and 45 mg/cm^2 for shot 13152. The peak shell $\rho\Delta R$ simulated by the 1-D code *LILAC* is ~500 mg/cm^2. This value is higher by a factor of ~7 than what was measured on shot 13151 (with SSD) and by a factor of ~11 on shot 13152 (without SSD). On the other hand, *ORCHID* simulations yield a peak total $\rho\Delta R$ of ~100 mg/cm^2, which is much closer to the experimental value. Further comparisons between the experimental results and code simulations are given below.

The areal-density values obtained above assume a uniform $\rho\Delta R$ over the shell surface. For a shell with modulations in $\rho\Delta R$, *the value* $\rho\Delta R_M$ *measured by opacity will always underestimate the average* $\langle\rho\Delta R\rangle$ because low-opacity regions have more weight in an integral opacity measurement. For example, if we assume that a fraction α of the shell area consists of radial holes (i.e., opacity $\tau = 0$) and the rest has a constant opacity τ, we find

$$\rho\Delta R_M / \langle\rho\Delta R\rangle = -\ln\left[\alpha + (1-\alpha)\exp(-\tau)\right]/(1-\alpha)\tau, \quad (1)$$

which is always less than 1. Also, it can be shown that for a given measured opacity τ_M, the relation $\alpha < \exp(-\tau_M)$ holds. In Fig. 79.23 the opacity of the absorption lines reaches the value 1.6 from which it follows that $\alpha < 0.2$. In the last section we describe a method for actually measuring the modulations in the areal density of the shell.

The Temperature of the Compressed Shell

The temperature of the shell at peak compression is an additional important parameter characterizing the implosion. We first use the absorption lines in Fig. 79.23 to deduce the temperature of the cool layer. These absorption lines each correspond to a Ti ion with an increasing number of L-shell vacancies; thus, the intensity distribution within the absorption-lines manifold corresponds to a distribution of ionization states from Ti^{+13} to Ti^{+20}. This distribution depends mostly on the temperature but also on the density. We use the collisional-radiative code *POPION*[10] to calculate the distribution of Ti ionization states as a function of temperature and density (for the experimental case of a 6% atom concentration of Ti in CH). Figure 79.26 shows as an example the average charge Z of Ti ions as a function of temperature for two density values: 1 g/cm^3 and 10 g/cm^3. As shown later, the shell density at peak compression is found to be within this range. *POPION* calculations show that for densities within this range, the measured absorption-line intensity distribution indicates a temperature in the range ~250 to ~350 eV. Additionally, the absorption-line intensity distribution is actually wider than that calculated for any single temperature, indicating absorption over a temperature gradient. Including this effect, the total range of possible temperatures indicated by the absorption lines is ~200 to ~400 eV.

We next turn to the determination of the cold-shell temperature. Unlike the cool layer where absorption lines are formed, no absorption lines are available for measuring the temperature

of the cold shell (where there are no *L*-shell vacancies into which absorption can take place). Instead, we can use the fluorescent Kα lines that are emitted following photoionization of *K*-shell electrons. To observe these lines more readily we use an off-center view that misses the core emission. We show in Fig. 79.27 the spectrum for shot 13151 in two views: through the center of the target and off the center. Indeed, the off-center view reveals a fluorescent Kα line emitted by *F*-like ions, coinciding in energy with the lowest-energy, *F*-like absorption feature. In the axial view this fluorescence cannot be seen because of the overlapping absorption at the same energy. For a colder shell the Kα line would appear at a slightly lower-energy position, indicating ionization of *M*-shell but not of *L*-shell electrons (the lowest-energy, or cold, Kα line is at 4.508 keV). In that case the Kα line would appear even in the axial view, not being subject to absorption, as has been the case in thicker-shell implosions.[3] The *F*-like Kα line is emitted following the *K*-shell photoionization of the Ne-like ions; thus, the bulk of the cold layer is in the closed-shell, Ne-like state; however, the width of the Kα line indicates that a smaller fraction of the Ti ions may be in lower ionizations. Using this result and *POPION* calculations we estimate the temperature of the cold shell as T ~150 to ~250 eV. For shot 13152 (without SSD) the cold-shell temperature is essentially the same.

It should be noted that in addition to the Kα line emitted in the cold shell, fluorescent Kα lines corresponding to each of the absorption lines of Fig. 79.27 should also be emitted within the cool layer. They cannot be seen in the spectrum because the $\rho\Delta R$ associated with each species having *L*-shell vacancies is only a fraction of the total cool-shell $\rho\Delta R$, which in turn is smaller than the cold-shell $\rho\Delta R$.

The position of the *K* edge can in principle provide an additional signature of the cold-shell temperature because for successive ionizations the *K* edge shifts to higher energies (see Fig. 72.8 in Ref. 2). For Ne-like Ti ions the *K*-edge shift is ~300 eV. This shift, however, is calculated for an isolated ion; at high densities *the K edge shifts to lower energies* due to interaction with neighboring ions. Using the model of Stewart and Pyatt,[11] assuming T ~ 200 eV and a density that changes over the range of 1 to 10 times solid density, the *K* edge of Ne-like Ti should shift toward lower energies by ~120 to ~300 eV; thus, the two effects partly cancel each other. Indeed, no significant *K*-edge shift is seen in Fig. 79.23. Accordingly, the *K*-edge shift is not a very useful diagnostic of shell temperature.

Kα Imaging of the Cold Shell

Previously we have shown that Kα emission constitutes an image of the cold shell around the time of peak compression.[3,5] Using this method we show here that shell compression improves with the implementation of SSD. In Ref. 5 a pinhole-array spectrometer was used to obtain two-dimensional images, whereas here a slit spectrograph is used to obtain essentially one-dimensional images; for shaped-pulse implosions the core

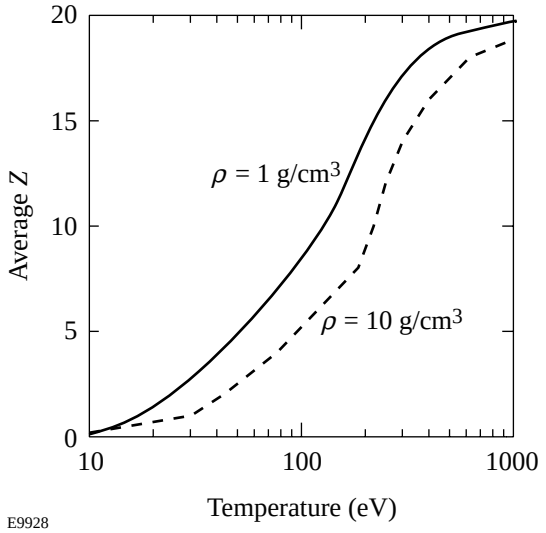

Figure 79.26
The average charge *Z* of Ti ions as calculated by the collisional-radiative code *POPION*. It is assumed that the titanium forms a 4% mixture (by atom) in CH.

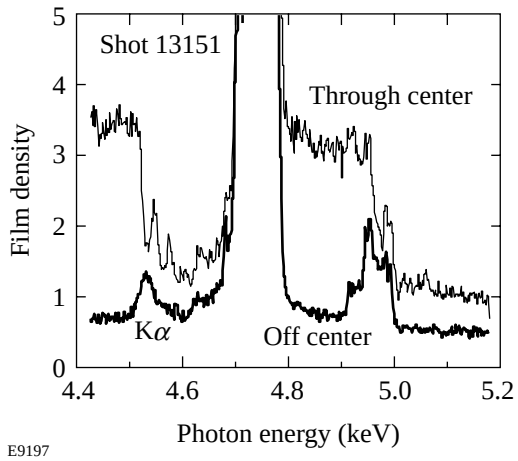

Figure 79.27
Determination of the cold-shell temperature through the fluorescing Kα lines. Only a view off the target center clearly shows the fluorescing line; its state of ionization (*F*-like Ti) indicates a cold-shell temperature of ~200 eV.

images are typically too weak to obtain high-quality images with the former instrument. In Fig. 79.28 we show part of the image obtained with the spatially resolving spectrograph, on two comparable shots, with and without SSD. The slit provides one-dimensional resolution in the vertical direction. In addition, the crystal provides low spatial resolution in the direction of dispersion (due to the Bragg's law); thus, the emission of Ti lines caused by burnthrough, because of their large extent, appears as two-dimensional images. This is important for separating Kα emission pumped by coronal radiation traveling inward during laser irradiation from Kα emission pumped by core radiation traveling outward during peak compression (Kα lines can only be emitted following pumping by a source located in a hotter region). The images of the Ti Heα line and its nearby satellites are elliptically shaped because there is no magnification in the direction of dispersion, whereas magnification in the perpendicular direction is provided by the slit. As in the spectra of Fig. 79.23, we see a much higher intensity of burnthrough radiation (e.g., the Ti Heα lines) in the no-SSD case, indicating a faster (and thus deeper) burnthrough due to instability growth. In fact, the Ti Heα line and its satellites appear as three limb-effect rings in the upper spectrum but are totally saturated in the lower spectrum. The lower spectrum also shows ring images of shifted Kα lines in the range of 4.6 to 4.7 keV. Their size is slightly smaller than that of the Ti Heα rings, indicating that they are pumped by radiation from the burnthrough region during the laser irradiation (see Fig. 75.30 in Ref. 12 and discussion thereof). The species emitting these lines are of relatively high ionization (e.g., B-like and Be-like Ti), indicating that radiation emitted during the burnthrough preheats the outer layer of the cold shell, ahead of the heat front, to ~300 to ~600 eV. These ring images show that *the accelerating shell does maintain its integrity with no large-scale breakup seen*. Such images can be used to study the uniformity of the accelerating shell. As in these target shots, the doping level can be made low enough so as not to greatly modify the behavior of the target and the doped layer can be placed deep enough that a burnthrough occurs at the end of the laser pulse. In this way the radiation from the doped layer does not interfere with the laser interaction and acceleration that occur earlier. *The radiation from the burnthrough thus provides a "flash" photography of the shell at the end of the acceleration phase.*

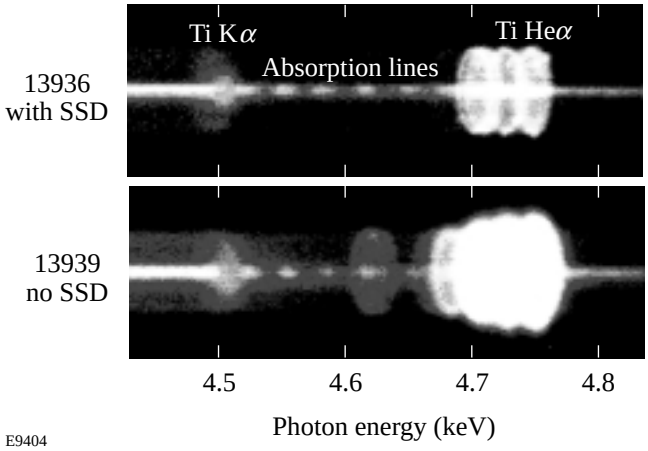

Figure 79.28
Effect of SSD as evidenced by x-ray spectra. A slit provides one-dimensional spatial resolution in the vertical direction; the crystal provides a low spatial resolution in the dispersion direction. Low-temperature Kα line (at ~4.52 keV) is pumped by core radiation; higher-temperature Kα lines (4.6 to 4.7 keV) are pumped by burnthrough to the Ti-doped layer.

In addition to these emission rings of Kα lines, a much stronger Kα line seen at ~4.52 keV (similar to that in Fig. 79.27) is emitted around the core and is clearly pumped by core radiation. The Kα lines are difficult to see in the streak spectra (which would further prove this point) because the integration over the target volume precludes an off-center view; on the other hand, the emission of the cold Kα line at peak compression was previously observed in streak data[5] because, as explained above, it is not absorbed in the shell. Also, related simulations described in Ref. 12 (Fig. 75.30) strongly support this conclusion. The temperature indicated by this feature has been estimated above to be ~150 to ~250 eV. Thus, the outer part of the doped layer is heated by the laser burnthrough to a temperature >1 keV (sufficient to excite Ti^{+20} and Ti^{+21} lines); radiation from this heated region flows inward and causes heating of additional material to ~300 to ~600 eV, all of which is ablated. The bulk of the doped layer, however, remains colder and implodes, reaching temperatures of ~150 to ~250 eV at peak compression. It should be noted that most of the radiative preheating is caused by sub-keV radiation whose range is smaller than the areal density of the initially ~5-μm-thick doped layer. Vertical lineouts through the Kα feature at ~4.52 keV have been Abel inverted,[13] separately for the two branches above and below the core image. The results (Fig. 79.29) clearly show that SSD smoothing results in both *a higher convergence and a higher shell compression*. This is consistent with the conclusion from Fig. 79.23 that SSD smoothing leads to a higher shell $\rho\Delta R$.

The Kα profiles in Fig. 79.29 can be converted to density profiles by requiring that the integral of the normalized profiles yields the measured $\rho\Delta R$ of the doped layer. Using this procedure we obtain peak density of ~1.2 g/cm^3 for shot 13936 and

~0.5 g/cm^3 for shot 13939. These values underestimate the density because time integration broadens the Kα spatial profiles. On the other hand, if the opacity above the *K* edge is much larger than 1, the Kα profile will be narrower than the density profile because of depletion of the pumping radiation; this is not the case in the present results.

1-D *LILAC* and 2-D *ORCHID* Simulations

The shots listed in Table 79.III were simulated with both the 1-D code *LILAC* and the 2-D code *ORCHID*. Present low-adiabat, shaped-pulse implosions perform below 1-D predictions (even with SSD),[14] and their replication is a stringent test for 2-D simulations. A particularly sensitive parameter characterizing target performance is the density profile of the cold shell around peak compression. As explained above, this density profile is determined by normalizing the Ti Kα fluorescence profiles (Fig. 79.29) to the shell $\rho\Delta R$ as measured by the *K*-edge absorption and the 1*s*–2*l* absorption lines. These profiles correspond to the part of the shell that is both doped and cold. As noted above, the target parameters were chosen so that all of the cold shell at peak compression would be doped so the Kα profile would correspond to the entire cold shell. Since we observe burnthrough of the laser into the doped layer (see Figs. 79.23 and 79.28), we can safely assume that none of the CH overcoat is cold during the compression. In Fig. 79.28, in addition to the ring-shaped images of the Ti Heα line at 4.75 keV (and its nearby satellites), a strong emission of these lines is also seen at the center of the target. To see this more clearly, we show in Fig. 79.30 the spatial profile of the calibrated intensity at the energy of the Ti Heα line, and at a nearby energy of the continuum; comparing the two lineouts clearly indicates a strong central emission of the Ti Heα line. Thus, the inner part of the doped layer must be part of the hot core, and the cold part of the shell contains only doped material. If the shell becomes highly distorted during either the acceleration or the deceleration, some of the Ti Heα emission may be due to mixing; in this case, some of the cold material will be undoped and the measured $\rho\Delta R$ through Ti absorption will underestimate the true cold-shell $\rho\Delta R$.

ORCHID simulations include the imprint of laser nonuniformity. For each beam, the known mode spectrum due to the phase plates was used, and modes up to $\ell = 300$ were added with random relative phases. The effect of multiple-beam overlap was calculated separately and accounted for. The effect of SSD was simulated by randomly reversing the phase of the laser modes at intervals equal to the coherence time (which is inversely proportional to the bandwidth and decreases with increasing mode number). Figure 79.31(a) shows typical profiles, azimuthally averaged, at peak compression; the averaged temperature was weighted by the density. A hot core is seen to be surrounded by a dense, colder layer. Before

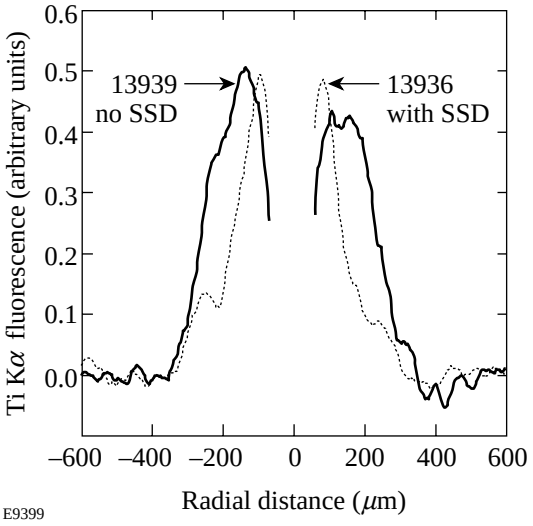

Figure 79.29
Abel inversion of image lineouts (from Fig. 79.28) at the *F*-like Kα line. The curves delineate the position and thickness of the cold shell around the time of peak compression. Higher convergence and compression due to SSD smoothing are evident.

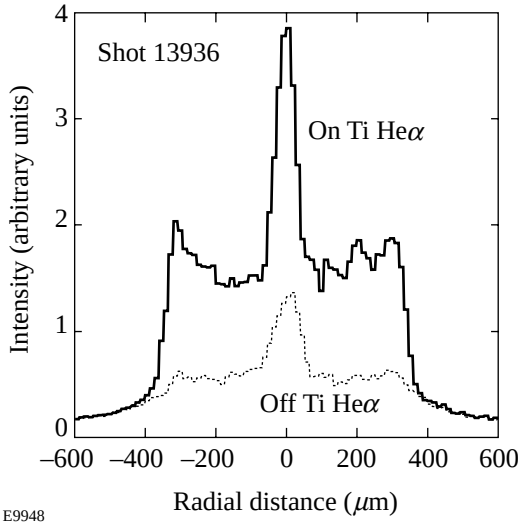

Figure 79.30
Spatial profile of the intensity at the energy of the Ti Heα line and at a nearby energy of the continuum (shot 13936) showing central emission of the line. This demonstrates that the cold shell around peak compression, detected by absorption, is mostly titanium doped.

comparing the *ORCHID* results to the experiment we note that the Ti Kα emission measures only the cold part of the shell. More specifically, the Kα line was shown in Fig. 79.27 to be emitted by neon-like and possibly lower ionizations. Thus, the density profile measured by the Kα line fluorescence refers only to that part of the total density that is cold enough to have a charge state $Z \le 12$. To compare the *ORCHID* density profiles to the experiment we multiply the former by the fraction of Ti ions in charge states $Z \le 12$, calculated by the collisional-radiative *POPION* code.[10] For the most part, the Ti in these calculations is in the neon-like state with only a small contribution from lower ionizations. In Fig. 79.31(b) we show typical cold-shell density profiles obtained in this way at three times around peak compression. Finally, to allow for comparison with the time-integrated Kα profiles, we calculate the time-averaged *ORCHID* density profile. We note that the Kα line intensity is proportional to the intensity of pumping core radiation (in addition to being proportional to the cold-shell $\rho\Delta R$ or, after Abel inverting, to ρ). Therefore, the average density profile was obtained by weighting the instantaneous density profiles by the core intensity just below the Ti *K* edge, obtained from the streak spectrograph data. Good agreement is seen in *both the shape and absolute magnitude* of the two density profiles: the time-averaged *ORCHID* profile and the profile measured through the Ti Kα fluorescence. On the other hand, the 1-D code *LILAC* shows a much narrower profile of vastly higher density (most of the sharp density peak in that profile is cold and should have been measured by the Kα profile in a 1-D implosion).

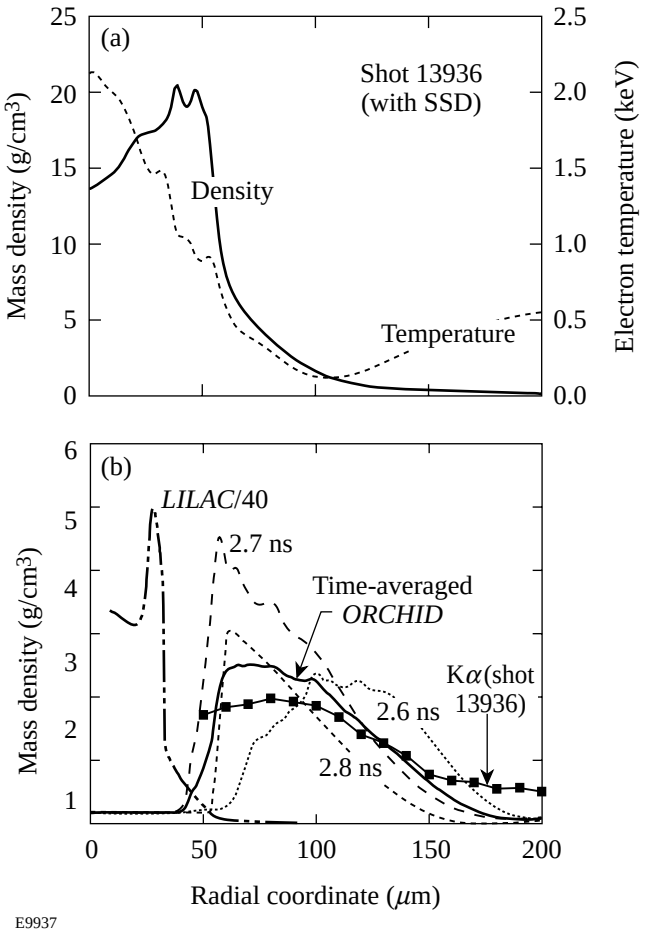

Figure 79.31
(a) Azimuthally averaged density and electron temperature profiles at peak compression calculated by *ORCHID* for shot 13936 (with SSD). (b) Density profiles of the cold shell for shot 13936. The 1-D *LILAC* profile shown is at peak compression. Three typical 2-D *ORCHID* profiles during different times of the compression are also shown. Using such profiles, the time-averaged density profile was obtained, weighted by the core intensity. The experimental time-integrated cold-shell density profile was obtained from the Ti Kα image.

In spite of the inherent inaccuracies in both the experiment and simulations, Fig. 79.31 shows that the cold-shell imaging diagnostics employed here provides a sensitive signature for testing the performance of 2-D codes in simulating unstable implosions. Further comparisons of measured and *ORCHID*-calculated modulations in compressed-shell $\rho\Delta R$ are underway.

Measurement of Shell $\rho\Delta R$ Modulation Through *K*-Edge Imaging

In addition to the integral measurements of shell $\rho\Delta R$ described above, we introduce a new method for *imaging the shell* $\rho\Delta R$ at peak compression, effectively using the core radiation as a backlighter for the shell. Such images are the final product of shell deformation due to the Rayleigh–Taylor instability and the Bell–Plesset effect and are thus of great interest in laser-fusion studies. Spatial modulations in a core image viewed through an absorbing shell depend on both the modulations in core emission as well as the modulations in shell $\rho\Delta R$. To isolate the latter, we use targets with a Ti-doped layer embedded within the shell and take the ratio of an image $I_{<K}$ just below the Ti *K* edge (at 4.96 keV) and an image $I_{>K}$ just above it. Since the absorption $\mu_{>K}$ above the *K* edge is much higher (by a factor of ~9.5) than the absorption $\mu_{>K}$ below it, the $\rho\Delta R$ image can be obtained through

$$\rho\Delta R = \ln\left(I_{<K}\right)/I_{>K}/\left(\mu_{>K} - \mu_{<K}\right). \qquad (2)$$

The method relies on the fact that the emitted continuum intensity (before absorption) changes very little between the two images. The thickness and doping level of the doped layer

can be conveniently adjusted to result in an opacity $\rho\Delta R\ \mu_{>K}$ ~1 to 2.

A particularly convenient way of obtaining such images is by employing the recently developed pinhole-array spectrometer.[5] Several hundred narrow-bandwidth images in the range of ~4 to ~7 keV are obtained at ~10-eV energy shifts between adjacent images. This device is particularly useful for *K*-edge imaging because monochromatic images provide high sensitivity to $\rho\Delta R$ modulations; also, the large number of images obtained close to either side of the *K* edge enables an improved noise analysis and consistency checks.

As a first test of the proposed method we applied it to an implosion (shot 15156) using a 1-ns square laser pulse. This choice was made because fast-rising pulses produce more-intense core radiation. The target and laser conditions are listed on the last line in Table 79.III. We use a pinhole-array spectrometer with 10-μm holes, giving a spatial resolution of ~16 μm. Figure 79.32 shows part of the image around the Ti *K* edge (4.964 keV); the crystal dispersion is in the horizontal direction. Each image is a monochromatic image of the core (of ~100-μm diameter), at a slightly different energy. In the vertical direction successive images are at energies separated by ~10 eV; in the horizontal (dispersion) direction the separation is ~100 eV. The energy bandwidth for each image is ~5 eV.[5] The six images on the left [Fig. 79.32(a)] are at energies just below the Ti *K* edge; the six images on the right [Fig. 79.32(b)] are just above the edge. The emission from the laser-interaction region is not seen in these images because, unlike the shots shown in Figs. 79.23 and 79.27, there has been no burnthrough to the Ti-doped layer in shot 15156. This is because of the thicker CH overlayer and the shorter laser pulse in this shot. The images below the *K* edge show structure on a scale length of about 20 to 30 μm. The images above the *K* edge show a similar structure. As explained, the structure in images below the edge is caused by nonuniformities in the core emission; the structure in the images above the edge reflects those same nonuniformities, plus any nonuniformities in the $\rho\Delta R$ of the absorbing shell. The purpose of the analysis described here is to separate the two sources of nonuniformity. To that end we perform 2-D Fourier analysis of the images in optical-density units and azimuthally average the results. In most other shots under similar conditions the core emission is more uniform; however, this shot was chosen to test the method's capability. The images in Fig. 79.32 are in optical-depth units [i.e., OD ~ ln(I), where the intensity I was deduced from the DEF-film density]. First, we must obtain the spatial spectrum of the noise (both in the images and in the film); to that end we subtract the Fourier spectra of two core images at energies below the *K* edge. Since the gross structure in all the images just below the *K* edge is the same, the difference between such images is caused only by the noise. Figure 79.33 shows the noise spectrum (thin solid line) thus obtained as an

(a) Below the Ti *K* edge (b) Above the Ti *K* edge

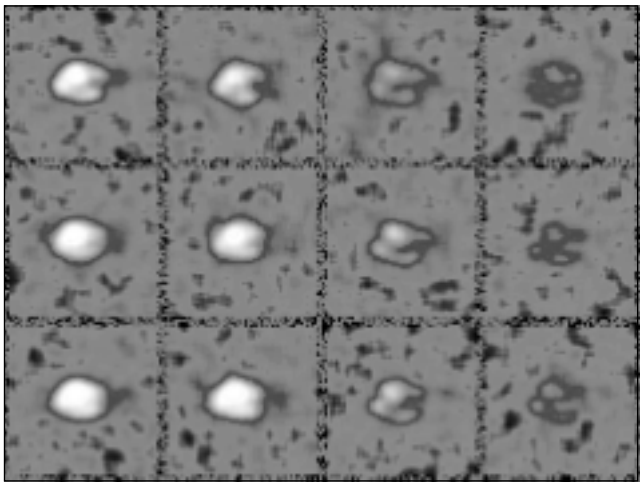

E9930

Figure 79.32
Sample of time-integrated monochromatic images of the core radiation obtained with a pinhole-array spectrometer, at energies (a) below the titanium *K* edge and (b) above the titanium *K* edge.

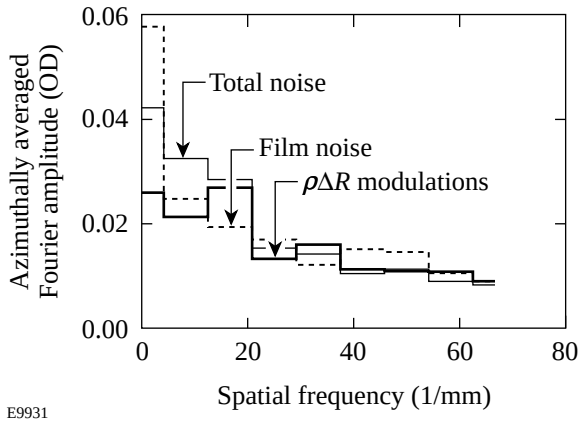

E9931

Figure 79.33
The azimuthally averaged Fourier amplitude of the measured optical depth versus spatial frequency for (a) the noise in the images below the *K* edge (thin solid line), (b) the film noise taken in an area between the images (dashed line), and (c) the modulations in $\rho\Delta R$ of the titanium-doped layer (thick solid line).

azimuthally averaged Fourier amplitude of optical-depth modulations versus spatial frequencies, using two of the images shown in Fig. 79.32(a); the results of using different image pairs from the same figure are very similar. The maximum spatial frequency corresponds to the spatial resolution of ~16 μm. Next we deduce the spectrum of film noise by analyzing in the same way a region on the film between the images, of equal area to that of the images; the dashed line in Fig. 79.33 shows the results. Finally, we derive the modulations in shell $\rho\Delta R$ by analyzing the difference in optical depth between two images at energies below and above the *K* edge. The spectrum of this difference, shown by the thick solid line in Fig. 79.33, contains noise plus modulations in the opacity of the titanium-doped layer. As seen in Eq. (2), the modulations in optical depth are proportional to the areal-density modulations of the doped layer. The three curves in Fig. 79.33 are very close for spatial frequencies above ~10 mm^{-1} or wavelengths shorter than 100 μm (the latter being about equal to the core size), indicating that *the film noise accounts for all the modulations in the images*; thus, there are no measured modulations in the shell areal density above the noise level for wavelengths between ~16 and ~100 μm. The sensitivity of this measurement was estimated using the noise spectrum obtained above. Assuming that modulations of the shell $\rho\Delta R$ are contained in the region of wavelengths from 10 to 80 μm, the σ_{rms} amplitude of the layer modulations must be more than a third of its thickness to become distinguishable from the noise. Thus, this analysis does not show modulations exceeding ~30% in the $\rho\Delta R$ of the doped layer, of wavelengths longer than ~16 μm and smaller than ~100 μm. We attribute this to the fast-rising square laser pulse, which reduces laser imprint and thus target distortions. Slower-rising pulse shapes (such as the ALPHA306 pulse used to obtain Fig. 79.23 data) are known to produce less-stable implosions, but the core intensity in such target shots was insufficient to perform meaningful analysis with this method. In future experiments we plan to increase the sensitivity of the measurement by replacing the diffracting crystal in the pinhole-array spectrometer with filters for sampling the spectrum below and above the Ti *K* edge. The loss in spectral definition can be partly offset by accounting for the spectrum, independently measured from a target without a doped layer.

ACKNOWLEDGMENT

This work was supported by the U.S. Department of Energy Office of Inertial Confinement Fusion under Cooperative Agreement No. DE-FC03-92SF19460, the University of Rochester, and the New York State Energy Research and Development Authority. The support of DOE does not constitute an endorsement by DOE of the views expressed in this article.

REFERENCES

1. B. Yaakobi, F. J. Marshall, D. K. Bradley, J. A. Delettrez, R. S. Craxton, and R. Epstein, Phys. Plasmas **4**, 3021 (1997).

2. Laboratory for Laser Energetics LLE Review **72**, 168, NTIS document No. DOE/SF/19460-199 (1997). Copies may be obtained from the National Technical Information Service, Springfield, VA 22161.

3. B. Yaakobi and F. J. Marshall, J. Quant. Spectrosc. Radiat. Transfer **61**, 465 (1999).

4. D. K. Bradley, J. A. Delettrez, R. Epstein, R. P. J. Town, C. P. Verdon, B. Yaakobi, S. Regan, F. J. Marshall, T. R. Boehly, J. P. Knauer, D. D. Meyerhofer, V. A. Smalyuk, W. Seka, D. A. Haynes, Jr., M. Gunderson, G. Junkel, C. F. Hooper, Jr., P. M. Bell, T. J. Ognibene, and R. A. Lerche, Phys. Plasmas **5**, 1870 (1998).

5. B. Yaakobi, F. J. Marshall, and D. K. Bradley, Appl. Opt. **37**, 8074 (1998).

6. Laboratory for Laser Energetics LLE Review **37**, 29, NTIS document No. DOE/DP40200-83 (1998). Copies may be obtained from the National Technical Information Service, Springfield, VA 22161.

7. D. K. Bradley, J. A. Delettrez, and C. P. Verdon, Phys. Rev. Lett. **68**, 2774 (1992); J. Delettrez, D. K. Bradley, and C. P. Verdon, Phys. Plasmas **1**, 2342 (1994).

8. D. J. Botto, J. McEnnan, and R. H. Pratt, Phys. Rev. A **18**, 580 (1978).

9. B. Yaakobi, R. S. Craxton, R. Epstein, and Q. Su, J. Quant. Spectrosc. Radiat. Transfer **58**, 75 (1997).

10. R. Epstein, S. Skupsky, and J. Delettrez, J. Quant. Spectrosc. Radiat. Transfer **35**, 131 (1986).

11. J. C. Stewart and K. D. Pyatt, Jr., Astrophys. J. **144**, 1203 (1966).

12. Laboratory for Laser Energetics LLE Review **75**, 182, NTIS document No. DOE/SF/19460-246 (1998). Copies may be obtained from the National Technical Information Service, Springfield, VA 22161.

13. C. M. Vest and D. G. Steel, Opt. Lett. **3**, 54 (1978).

14. Laboratory for Laser Energetics LLE Review **78**, 82, NTIS document No. DOE/SF/19460-295 (1999). Copies may be obtained from the National Technical Information Service, Springfield, VA 22161.

Experimental Investigation of Smoothing by Spectral Dispersion

In the direct-drive approach to inertial confinement fusion (ICF), capsules are irradiated directly by a large number of symmetrically arranged laser beams.[1,2] Nonuniformities in the laser irradiation may seed the Rayleigh–Taylor hydrodynamic instability, which degrades target performance;[3] therefore, a combination of beam-smoothing techniques is employed to achieve the high irradiation uniformity required for direct-drive laser-fusion experiments. These techniques, which include two-dimensional smoothing by spectral dispersion (2-D SSD),[4–6] distributed phase plates (DPP's),[7,8] polarization smoothing (DPR's),[9–11] and multiple-beam overlap, will also be implemented on the 1.8-MJ, 351-nm, 192-beam National Ignition Facility (NIF),[12] which is currently under construction at the Lawrence Livermore National Laboratory. Direct-drive laser fusion requires a high degree of laser-irradiation uniformity on target: the rms irradiation nonuniformity must be below 1% when the laser intensity has been averaged over a few hundred picoseconds.[2,5]

Characterization of the laser-irradiation nonuniformity is essential for ICF research since the efficiency with which the nonuniformities in the laser-irradiation imprint target mass perturbations (i.e., laser imprint) depends on the early-time intensity history and the spatial wavelength of the nonuniformity.[13] The strategy of 2-D SSD with phase plates, which is the preferred mechanism for reducing laser-beam irradiation nonuniformity in glass lasers, is to vary the interference (speckle) pattern of the phase plate on a time scale that is short compared to the characteristic hydrodynamic response time of the target (i.e., imprinting time). (An alternate technique, ISI, has been developed for KrF lasers.[14]) Predictions show that 2-D SSD smoothing with $\Delta\nu_{UV} \approx 1$ THz will smooth the spherical-harmonic modes of $\ell = 20$ through 150 to acceptable levels for ICF.[5] The bandwidth on OMEGA[15] will be increased from 0.2 to 1 THz during this year, which will decrease the smoothing time by a factor of 5.

In this research the temporal rate of beam smoothing produced by 2-D SSD with the current bandwidth of $\Delta\nu_{UV} \approx 0.2$ THz is quantified by analyzing measured ultraviolet equivalent-target-plane (UVETP) images of a single OMEGA laser beam. The next three sections describe (1) laser-beam smoothing with 2-D SSD and phase plates, (2) 2-D SSD model calculations, and (3) the diagnostic used to record UVETP images of laser pulses having constant peak power and varying duration (100 ps to 3.5 ns). Power spectra calculated from the measured UVETP images along with the measured smoothing rate of 2-D SSD are presented and compared with theoretical predictions in the **Experimental Results and Analysis** section. This work shows that the theoretical predictions of 2-D SSD laser-beam smoothing are in excellent agreement with the measured temporal smoothing rates.

Background

Smoothing of laser beams using SSD has been described in Ref. 4. On OMEGA the phase plates are placed before the focusing lens and produce far-field spots with highly reproducible spatial intensity envelopes and speckle distributions. Smoothing by spectral dispersion is achieved by frequency modulating the phase of a laser beam, wavelength dispersing the beam, and passing it through a phase plate so that the spectral components are separated in the target plane by at least one-half the beam's diffraction-limited width. The reduction in laser-irradiation nonuniformity is wavelength dependent. The longest wavelength of nonuniformity that can be smoothed by SSD is twice the maximum spatial shift $S_{max} = F\Delta\theta$ of the speckle pattern that can be produced by the laser, where $\Delta\theta$ is the angular spread of the wavelength-dispersed light propagating through the laser and F is the focal length of the OMEGA lens. (The ultimate limit of S is given by the maximum allowable angular spread in the spatial filter in the laser system.) Thus, spherical-harmonic modes of nonuniformity down to $l_{cut} = 2\pi R/(2S_{max})$, where R is the target radius, can be smoothed with 2-D SSD.[5] Spherical targets on OMEGA have $R \simeq 500$ μm, and the present 2-D SSD system has $S_{max} = 100$ μm; hence $l_{cut} = 16$.

Model Calculations

The time-integrated far field is calculated by temporal integration of the modulus squared of a two-dimensional

spatial Fourier transform of the UV near field. The complex-valued electric field that describes the UV near field can be written as

$$E(x,y,t) \equiv E_0(x,y,t)e^{i\phi_{2\text{-D SSD}}(x,y,t)}e^{i\phi_B(x,y,t)}e^{i\phi_{\text{DPP}}(x,y)}, \quad (1)$$

where $E_0(x,y,t)$ defines the temporal and spatial beam shapes, $\phi_{2\text{-D SSD}}(x,y,t)$ is the 2-D SSD phase contribution, $\phi_B(x,y,t)$ is the intensity-dependent phase contribution of the *B*-integral,[16] and $\phi_{\text{DPP}}(x,y)$ is the static phase-plate contribution, which depends on the particular phase-plate design.

The spatially and temporally varying phase due to 2-D SSD is[17]

$$\phi_{2\text{-D SSD}}(x,y,t) \equiv 3\delta_{Mx}\sin\left[\omega_{Mx}\left(t+\xi_x x\right)\right] + 3\delta_{My}\sin\left[\omega_{My}\left(t+\xi_y y\right)\right], \quad (2)$$

where the *x* and *y* subscripts denote the two smoothing dimensions, $\delta_{Mx,y}$ is the modulation depth, $\nu_{Mx,y} = \omega_{Mx,y}/2\pi$ is the RF modulation frequency, and $\xi_{x,y}$ is the angular grating dispersion. The factor of 3 in Eq. (2) indicates that the electric field has undergone frequency tripling from the IR to UV. The 2-D SSD system parameters on OMEGA for the UVETP measurements are $\delta_{Mx} = 5.12$, $\nu_{Mx} \equiv 3.3$ GHz, $\xi_x = 1.11$ ns/m, $\Delta\lambda_{Mx} = 1.25$ Å, $\delta_{My} = 7.89$, $\nu_{My} \equiv 3.0$ GHz, $\xi_y = 1.11$ ns/m, and $\Delta\lambda_{My} = 1.75$ Å, assuming a nominal beam diameter of 27.5 cm. The modulation depths and the bandwidths are given for the IR. The maximum angular spread $\Delta\theta$ is given by $\Delta\theta = \xi(c/\lambda)\Delta\lambda$, where *c* is the speed of light and $\lambda = 1053$ nm. Cases without frequency modulation are modeled by setting modulation depths equal to zero, i.e., $\delta_{Mx} = 0$ and $\delta_{My} = 0$.

Our simulations indicate that *B*-integral effects are negligible for all cases except when the frequency modulation is turned off.

UVETP Diagnostic

The layout of the diagnostic used to acquire the UVETP images of a single OMEGA beam is shown in Fig. 79.34. Time-integrated UVETP images were recorded with a CCD camera. All of the measurements presented in this article exploit the low noise level and the large dynamic range of the CCD to extract power spectra from the UVETP images with negligible noise levels. The UV-sensitive CCD camera is a back-thinned SITe 003B chip in a Photometrics Series 300 camera.[18] The sensor has an array of 1024 × 1024 photosensitive elements with a pixel size of 24 μm × 24 μm. The spatial sampling rate is ~2 pixels/μm, which is approximately five times the *f*-number-limited spatial frequency $f_0 \equiv \Delta/\lambda F$, where *D* is the beam diameter of the OMEGA lens and $\lambda = 351$ nm.

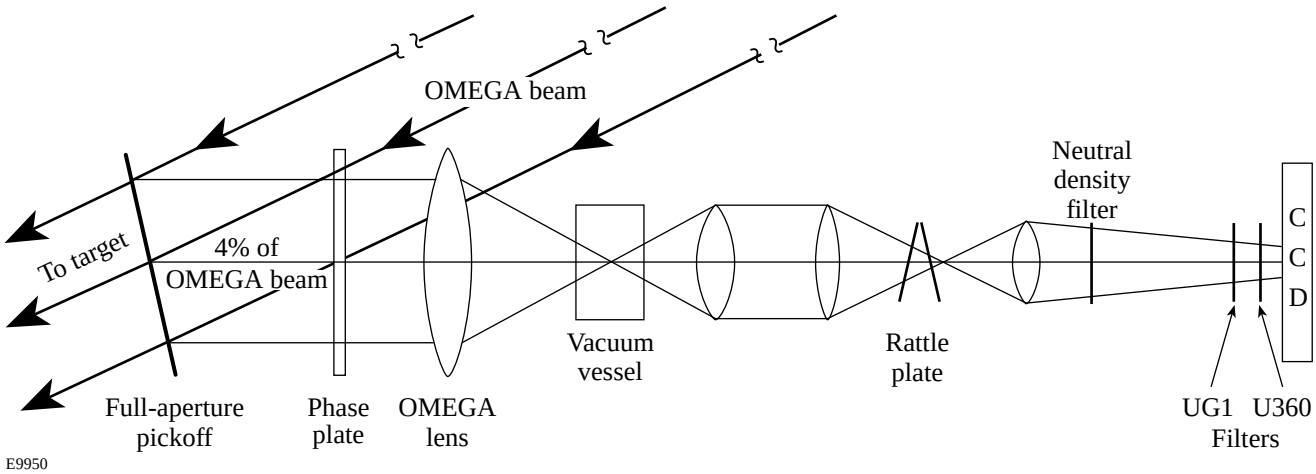

Figure 79.34
Schematic of the UVETP diagnostic. The on-target spot size is magnified by $M = 46$ on the CCD camera.

A full-aperture optical wedge in one of the 60 laser beams (BL-19) directs 4% of the laser light to an OMEGA focusing lens (see Fig. 79.34). The phase plate is placed directly in front of the lens, mimicking the target/beam configuration. The beam is brought through focus in a vacuum tube, down collimated with a doublet lens, brought to focus with a 2-m lens, and relayed to the CCD camera with the final lens. The beam intensity is reduced with three 4% reflections (not shown in Fig. 79.34) and the fifth-order reflection of a rattle plate (consisting of two surfaces with R = 70% per surface). The optical background is reduced to negligible levels with a light shield surrounding the CCD optics and the CCD camera. The light levels incident on the CCD are optimized by attenuating the beam with a neutral density filter that is placed after the final lens. Background-visible and IR signals are blocked with broadband UG1[19] and U360[20] UV bandpass filters mounted in front of the CCD camera. Compared with the laser spot size on target the UVETP image on the CCD camera is magnified by a factor of ~46.

Small-scale and whole-beam *B*-integral effects were found to provide smoothing of beams without frequency modulation. (The detailed analysis of beams without frequency modulation will be presented in a later publication.) A UVETP image of a laser pulse with zero accumulated *B*-integral (*B*-integral <1.0 rad in the UV) and no frequency modulation was measured to quantify the amount of beam smoothing due to the *B*-integral at higher laser powers. The power spectrum is the azimuthal sum at each spatial frequency of the square of the Fourier amplitudes. The power spectrum is normalized to the dc component, and the single-beam irradiation nonuniformity σ_{rms} is defined as the square root of the ratio of the power in the high frequencies (i.e., $k \geq 0.04\ \mu m^{-1}$ in the OMEGA target plane) to the power in the low frequencies (i.e., $k < 0.04\ \mu m^{-1}$). The highest (cutoff) wave number $k = 2.68\ \mu m^{-1}$ corresponds to the *f*-number-limited spatial frequency. A spectrum for a zero-*B*-integral laser pulse without frequency modulation is presented in Fig. 79.35 and its irradiation nonuniformity, σ_{rms} = 93.4%, is the highest measured under any condition and is near the 100% value expected from theory. The theoretical power spectrum simulated with the time-dependent code (described in the previous section) is also shown in Fig. 79.35 and includes the spatiotemporal near-field irradiance and small-scale and whole-beam *B*-integral effects. The higher value of σ_{rms} predicted by the model is caused by the discrepancy between the model and the measurement in the low wave numbers (see Fig. 79.35). Nevertheless, the predicted speckle structure shows excellent agreement with the measurement; hence, the zero accumulated *B*-integral shot serves as a calibration that demonstrates the capability of the UVETP diagnostic to measure highly modulated spatial intensity profiles of pulses with no frequency modulation.

Experimental Results and Analysis

Measured UVETP images of 3.5-ns square laser pulses without frequency modulation and with 2-D SSD are presented in Figs. 79.36(a) and Fig 79.36(b), respectively. These images qualitatively illustrate the effect of laser-beam smoothing with 2-D SSD. The images with 2-D SSD show a smooth spatial intensity envelope [see single pixel lineout overplotted on

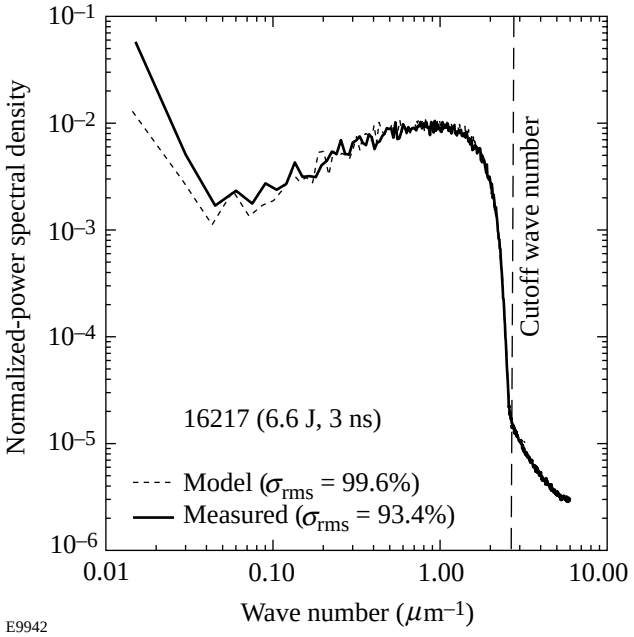

Figure 79.35
Power spectra obtained from a UVETP image of a laser pulse with zero accumulated *B*-integral (*B*-integral < 1.0 radian in the UV) without frequency modulation. The power spectrum is the azimuthal sum at each frequency of the square of the Fourier amplitudes, and the cutoff wave number corresponds to the *f*-number-limited spatial frequency. The power spectra are normalized to the dc component, and the σ_{rms} is defined as the square root of the ratio of the power in the high frequencies (i.e., $k \geq 0.04\ \mu m^{-1}$ in the OMEGA target plane) to the power in the low frequencies (i.e., $k < 0.04\ \mu m^{-1}$). Solid/dashed lines represent measured/modeled power spectra. The predicted speckle structure shows excellent agreement with the measurement; hence, the zero accumulated *B*-integral shot serves as a calibration that demonstrates the capability of the UVETP diagnostic to fully resolve individual speckles.

image in Fig. 79.36(b)], while the pulses without frequency modulation have a highly modulated spatial intensity profile [see single pixel lineout overplotted on image in Fig. 79.36(a)]. The spatial resolution and overall detector size of the CCD restrict the UVETP measurement to slightly more than one-half of the laser-beam profile. As seen in Fig. 79.36, the laser beam is centered nominally on the photodetector, and 550 μm of the 950-μm (defined as the 95% enclosed energy contour) laser spot is sampled.

The temporal rate of 2-D SSD smoothing is deduced from the power spectra of the measured UVETP images of laser pulses having constant peak power and pulse lengths ranging from 100 ps to 3.5 ns. Power spectra calculated from measured UVETP images of (a) 100-ps and (b) 3-ns laser pulses smoothed with 2-D SSD are presented in Fig. 79.37. The time-dependent nature of 2-D SSD smoothing is evident in the measured results with lower measured values of σ_{rms} for the longer pulse lengths. The low-wave-number power spectrum is determined by the spatial intensity envelope of the far field. The UVETP diagnostic was configured with a phase plate that produced a far-field spot with a super-Gaussian spatial intensity envelope $\left[I \sim \exp\left(r/r_0\right)^{2.5}\right]$ for these pulses.

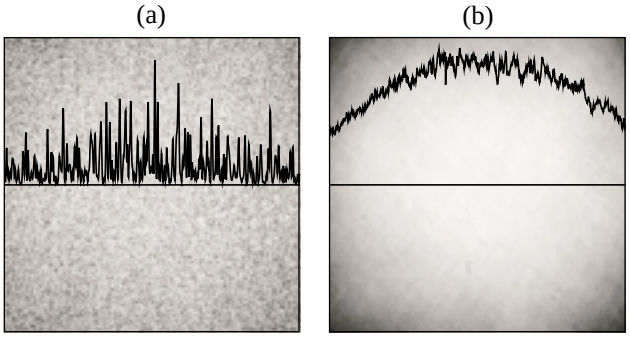

Figure 79.36
Measured UVETP images of 3.5-ns square laser pulses (a) without frequency modulation and (b) with 2-D SSD at $\Delta\nu_{UV} \approx 0.2$ THz. As demonstrated with the single pixel lineout through the center of the beam, the laser pulse with 2-D SSD has a smooth spatial intensity envelope, while the pulse without frequency modulation has a highly modulated spatial intensity profile. The spatial resolution and overall detector size of the CCD restrict the UVETP measurement to slightly more than one-half of the laser-beam profile. The laser beam is centered nominally on the photodetector, and 550 μm of the 950-μm laser spot (defined as the 95% enclosed energy contour) is sampled.

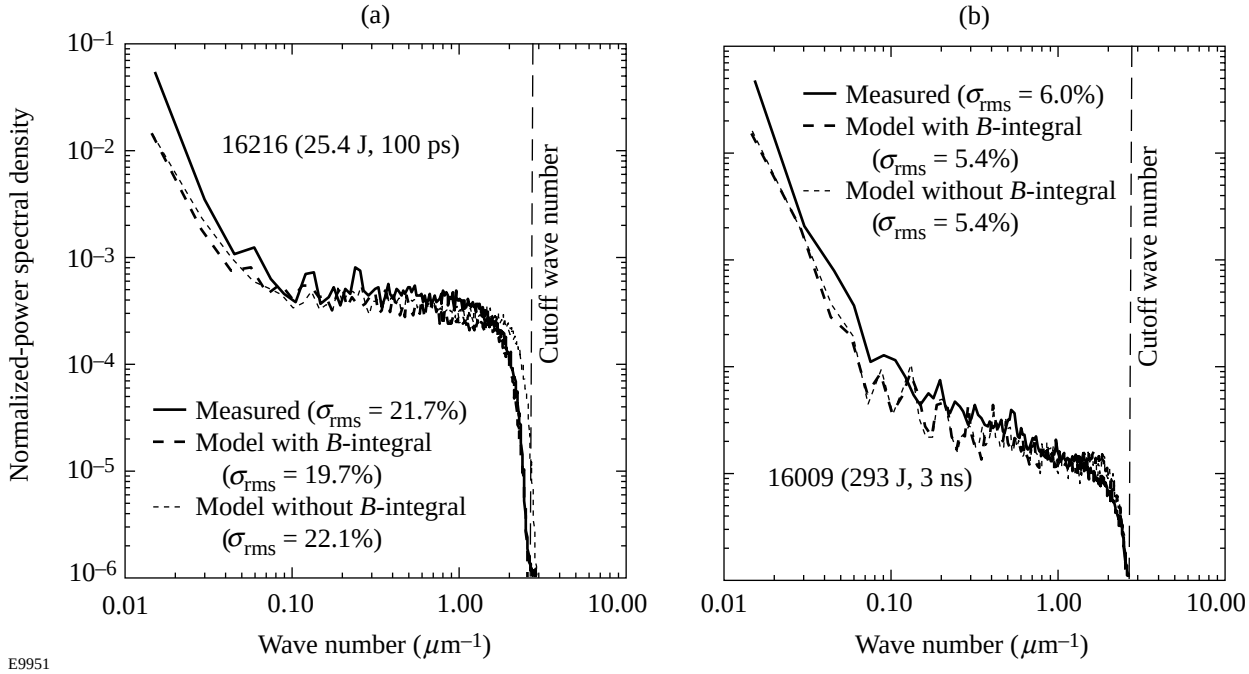

Figure 79.37
Power spectra calculated from UVETP images of (a) 100-ps and (b) 3-ns laser pulses with 2-D SSD. The thick, solid line represents the measured power spectrum. The thick, dashed line represents the time-dependent simulation that includes both the spatiotemporal behavior of the near-field irradiance and small-scale and whole-beam *B*-integral effects. The thin, dashed line represents a time-dependent model neglecting *B*-integral effects. Both models are in agreement with the measured results, and *B*-integral effects are negligible for all cases except for pulses without frequency modulation.

The 2-D SSD power spectra simulated with the time-dependent code (described in a previous section) with and without *B*-integral effects are plotted in Fig. 79.37. The *B*-integral effects are completely negligible as shown in this figure. The excellent agreement between the simulated power spectra and the measured spectra is clearly apparent in Fig. 79.37.

The measured temporal rate of 2-D SSD smoothing is shown in Fig. 79.38, which is a compilation of data from over 150 laser shots that clearly demonstrates the decrease in the measured σ_{rms} with increasing pulse length. Statistical error bars are smaller than the symbols. The 3.5-ns pulse has the lowest measured $\sigma_{\text{rms}} = 6.0\%$. The measurement of the laser-irradiation nonuniformity for the 3.5-ns pulses without frequency modulation is also presented for comparison. The thin line is the time-integrated simulation of the single-beam irradiation nonuniformity σ_{rms} that neglects the *B*-integral effects and assumes a static near field with a uniform irradiance. It is in agreement with the measured results (black circles), and it predicts that an asymptotic level of smoothing is reached just after 3 ns. The thick, solid line in Fig. 79.38 represents model predictions for the σ_{rms}:

$$\sigma_{\text{rms}} = \sqrt{\sigma_0^2\left(\frac{t_c}{t+t_c}\right)+\sigma_{\text{asymp}}^2}\,, \tag{3}$$

where $t_c = 1/\Delta\nu_{\text{UV}} = 5$ ps is the coherence time, $\Delta\nu_{\text{UV}}$ = 0.2 THz is the UV bandwidth, t is the averaging time (i.e., pulse length), σ_0 is the initial laser nonuniformity, and σ_{asymp} is the asymptotic level of 2-D SSD smoothing calculated from the time-integrated far-field simulation. This prediction adds the asymptotic levels of smoothing in quadrature to the model given in Ref. 14. The dashed line in Fig. 79.38 is a plot of Eq. (3) with the σ_{asymp} set to zero. The deviation of the thick, solid line from the dashed line around 1 ns signifies that the beam smoothing is approaching its asymptotic limit. The asymptotic behavior can be observed in the measured values of σ_{rms}.

The dependence of the rate of smoothing on the wave number k is examined in Fig. 79.39, where σ_{rms} is plotted as a function of pulse length for the spectral wavelength ranges of λ = 20-μm, λ = 30-μm, λ = 60-μm, and λ = 150-μm wavelengths, corresponding to k = 0.31 μm^{-1}, k = 0.21 μm^{-1}, k = 0.10 μm^{-1}, and k = 0.04 μm^{-1}. Statistical error bars are again smaller than the symbols for the majority of the data. For OMEGA, this corresponds to spherical-harmonic modes of ℓ = 20 through 150, which are considered the most dangerous for ICF implosions.[5] Again the time-integrated 2-D SSD predictions are in good agreement with the experimental observations (*B*-integral effects are negligible here, too). The data have also been fitted using Eq. (3) with the approximation[5,21]

$$t_c = \left[\Delta\nu_{\text{UV}} \times \sin\left(k\delta/2\right)\right]^{-1}, \tag{4}$$

where δ is the separation between spectral modes. (For one color cycle δ corresponds to one-half of a speckle width,

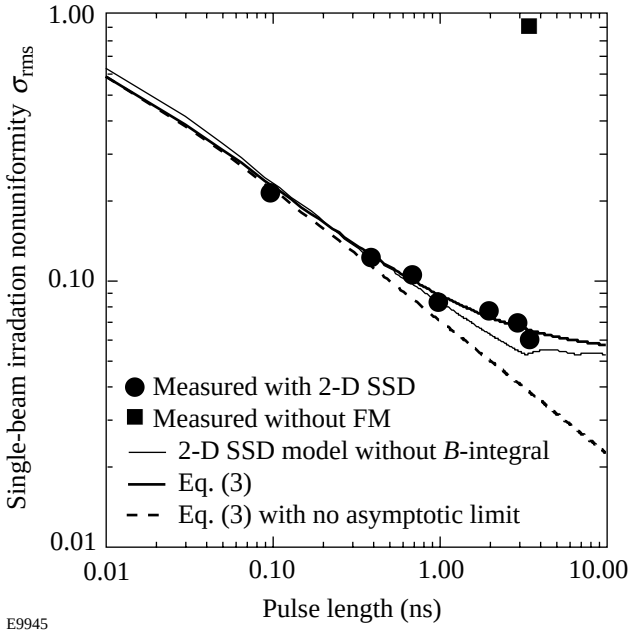

Figure 79.38
A compilation of data from over 150 laser shots demonstrates the temporal smoothing rates of 2-D SSD. Statistical error bars are smaller than the symbols. The 3.5-ns pulse has the lowest measured σ_{rms} = 6.0%. The 3.5-ns pulse without frequency modulation is shown for comparison. The thin, solid line is the time-integrated simulation of the single-beam irradiation nonuniformity σ_{rms} that neglects the *B*-integral effects and assumes a static near field with a uniform irradiance. The thick, solid line represents the model predictions for σ_{rms} using Eq. (3). The dashed line is the model prediction for σ_{rms} with $\sigma_{\text{asymp}} = 0$.

i.e., $\delta = F\lambda/D = 2.35\ \mu$m.) In a manner similar to Fig. 79.38, the case neglecting the asymptotic behavior of Eq. (3) is also plotted in Fig. 79.39. The initial value of the laser nonuniformity σ_0 for each spectral range was determined by taking the average value of the measured σ_{rms} for shots without frequency modulation. The data in Fig. 79.39 demonstrate that the shorter wavelengths ($\lambda = 20\ \mu$m) are smoothed more effectively than the longer wavelengths. It can also be observed that the longer-wavelength modes approach their asymptotic limits sooner than the shorter ones. Only a small amount of smoothing is observed for $\lambda = 150$-μm wavelength (corresponding to $l \approx 20$), which is in agreement with the prediction.

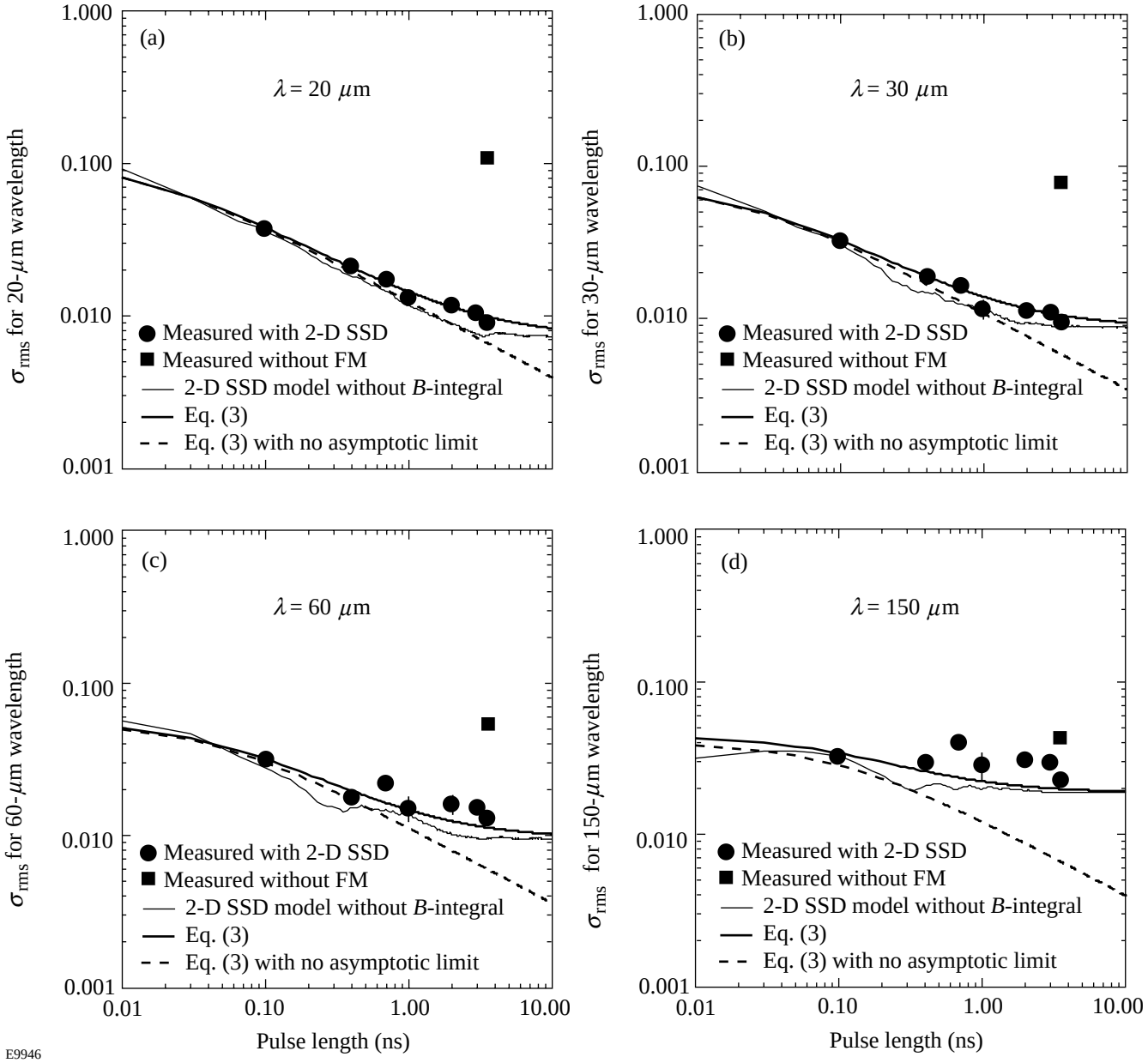

Figure 79.39
Temporal smoothing rates for specific spatial wavelengths (a) $\lambda = 20\ \mu$m ($k = 0.31\ \mu$m^{-1}), (b) $\lambda = 30\ \mu$m ($k = 0.21\ \mu$m^{-1}), (c) $\lambda = 60\ \mu$m ($k = 0.10\ \mu$m^{-1}), and (d) $\lambda = 150\ \mu$m ($k = 0.04\ \mu$m^{-1}). Statistical error bars are smaller than the symbols for the majority of the data. The 2-D SSD predictions are in good agreement with the experimental observations. The thick, solid line represents the model predictions for σ_{rms} using Eqs. (3) and (4). The dashed line is a model prediction for $\sigma_{asymp} = 0$. The thin, solid line is the predicted σ_{rms} from a 2-D SSD simulation using a static near field with a uniform irradiance and neglecting *B*-integral effects.

Conclusion

Direct-drive ICF experiments require a laser system with excellent irradiation uniformity. Two-dimensional smoothing by spectral dispersion is currently the best mechanism for reducing laser-beam nonuniformities for high-power/energy glass lasers. UVETP images of a single OMEGA laser beam were recorded to quantify the single-beam irradiation nonuniformity. The smoothing rate of 2-D SSD (with the current UV bandwidth of $\Delta\nu_{UV} \approx 0.2$ THz) was determined by analyzing the power spectra of measured UVETP images of laser pulses having constant peak power and pulse lengths ranging from 100 ps to 3.5 ns. Simulated 2-D SSD power spectra and temporal smoothing rates are in excellent agreement with the experimental data and permit confident extrapolation to larger laser systems and higher UV bandwidths.

ACKNOWLEDGMENT

The authors appreciate the support of Sam Morse and the entire OMEGA engineering staff, especially Chris Cotton for the design of the CCD optics, Charles Kellogg for the installation of the diagnostic, and Keith Thorp, Per Adamson, Ray Huff, Matt Kamm, Dave Kuhn, and Howard Ammenheuser for the operation and alignment of the diagnostic. This work was supported by the U.S. Department of Energy Office of Inertial Confinement Fusion under Cooperative Agreement No. DE-FC03-92SF19460, the University of Rochester, and the New York State Energy Research and Development Authority. The support of DOE does not constitute an endorsement by DOE of the views expressed in this article.

REFERENCES

1. C. P. Verdon, Bull. Am. Phys. Soc. **38**, 2010 (1993).

2. S. E. Bodner, D. G. Colombant, J. H. Gardner, R. H. Lehmberg, S. P. Obenschain, L. Phillips, A. J. Schmitt, J. D. Sethian, R. L. McCrory, W. Seka, C. P. Verdon, J. P. Knauer, B. B. Afeyan, and H. T. Powell, Phys. Plasmas **5**, 1901 (1998).

3. D. K. Bradley, J. A. Delettrez, and C. P. Verdon, Phys. Rev. Lett. **68**, 2774 (1992); J. Delettrez, D. K. Bradley, and C. P. Verdon, Phys. Plasmas **1**, 2342 (1994); J. D. Kilkenny, S. G. Glendinning, S. W. Haan, B. A. Hammel, J. D. Lindl, D. Munro, B. A. Remington, S. V. Weber, J. P. Knauer, and C. P. Verdon, Phys. Plasmas **1**, 1379 (1994); R. Epstein, J. Appl. Phys. **82**, 2123 (1997); V. A. Smalyuk, T. R. Boehly, D. K. Bradley, V. N. Goncharov, J. A. Delettrez, J. P. Knauer, D. D. Meyerhofer, D. Oron, and D. Shvarts, Phys. Rev. Lett. **81**, 5342 (1998).

4. S. Skupsky, R. W. Short, T. Kessler, R. S. Craxton, S. Letzring, and J. M. Soures, J. Appl. Phys. **66**, 3456 (1989).

5. Laboratory for Laser Energetics LLE Review **69**, 1, NTIS document No. DOE/SF/19460-152 (1996); S. Skupsky and R. S. Craxton, Phys. Plasmas **6**, 2157 (1999).

6. J. E. Rothenberg, J. Opt. Soc. Am. B **14**, 1664 (1997).

7. T. J. Kessler, Y. Lin, J. J. Armstrong, and B. Velazquez, in *Laser Coherence Control: Technology and Applications*, edited by H. T. Powell and T. J. Kessler (SPIE, Bellingham, WA, 1993), Vol. 1870, pp. 95–104.

8. Y. Lin, T. J. Kessler, and G. N. Lawrence, Opt. Lett. **21**, 1703 (1996).

9. Y. Kato, unpublished notes (1984); K. Tsubakimoto *et al.*, Opt. Commun. **91**, 9 (1992); K. Tsubakimoto *et al.*, Opt. Commun. **103**, 185 (1993).

10. Laboratory for Laser Energetics LLE Review **45**, 1, NTIS document No. DOE/DP40200-149 (1990); T. E. Gunderman, J.-C. Lee, T. J. Kessler, S. D. Jacobs, D. J. Smith, and S. Skupsky, in *Conference on Lasers and Electro-Optics*, Vol. 7, 1990 OSA Technical Digest Series (Optical Society of America, Washington, DC, 1990), p. 354.

11. T. R. Boehly, V. A. Smalyuk, D. D. Meyerhofer, J. P. Knauer, D. K. Bradley, R. S. Craxton, M. J. Guardalben, S. Skupsky, and T. J. Kessler, J. Appl. Phys. **85**, 3444 (1999).

12. J. Paisner *et al.*, Laser Focus World **30**, 75 (1994).

13. M. Desselberger *et al.*, Phys. Rev. Lett. **68**, 1539 (1992); S. G. Glendinning, S. V. Weber, P. Bell, L. B. DaSilva, S. N. Dixit, M. A. Henesian, D. R. Kania, J. D. Kilkenny, H. T. Powell, R. J. Wallace, P. J. Wegner, J. P. Knauer, and C. P. Verdon, *ibid*. **69**, 1201 (1992); D. H. Kalantar, M. H. Key, L. B. DaSilva, S. G. Glendinning, J. P. Knauer, B. A. Remington, F. Weber, and S. V. Weber, *ibid*. **76**, 3574 (1996); S. G. Glendinning, S. N. Dixit, B. A. Hammel, D. H. Kalantar, M. H. Key, J. D. Kilkenny, J. P. Knauer, D. M. Pennington, B. A. Remington, R. J. Wallace, and S. V. Weber, Phys. Rev. E **54**, 4473 (1996); R. J. Taylor *et al.*, Phys. Rev. Lett. **79**, 1861 (1997); D. H. Kalantar, M. H. Key, L. B. Da Silva, S. G. Glendinning, B. A. Remington, J. E. Rothenberg, F. Weber, S. V. Weber, E. Wolfrum, N. S. Kim, D. Neely, J. Zhang, J. S. Wark, A. Demir, J. Lin, R. Smith, G. J. Tallents, C. L. S. Lewis, A. MacPhee, J. Warwick, and J. P. Knauer, Phys. Plasmas **4**, 1985 (1997); S. G. Glendinning, S. N. Dixit, B. A. Hammel, D. H. Kalantar, M. H. Key, J. D. Kilkenny, J. P. Knauer, D. M. Pennington, B. A. Remington, J. Rothenberg, R. J. Wallace, and S. V. Weber, Phys. Rev. Lett. **80**, 1904 (1998); T. R. Boehly, V. A. Smalyuk, O. Gotchev, J. P. Knauer, D. D. Meyerhofer, D. K. Bradley, J. A. Delettrez, S. Skupsky, and R. P. J. Town, Bull. Am. Phys. Soc. **43**, 1664 (1998).

14. R. H. Lehmberg and S. P. Obenschain, Opt. Commun. **46**, 27 (1983); R. H. Lehmberg, A. J. Schmitt, and S. E. Bodner, J. Appl. Phys. **62**, 2680 (1987).

15. T. R. Boehly, D. L. Brown, R. S. Craxton, R. L. Keck, J. P. Knauer, J. H. Kelly, T. J. Kessler, S. A. Kumpan, S. J. Loucks, S. A. Letzring, F. J. Marshall, R. L. McCrory, S. F. B. Morse, W. Seka, J. M. Soures, and C. P. Verdon, Opt. Commun. **133**, 495 (1997).

16. D. C. Brown, in *High-Peak-Power Nd:Glass Laser Systems*, edited by D. L. MacAdam, Springer Series in Optical Sciences (Springer-Verlag, Berlin, 1981), Vol. 25, p. 45.

17. Laboratory for Laser Energetics LLE Review **78**, 62, NTIS document No. DOE/SF/19460-295 (1999). Copies may be obtained from the National Technical Information Service, Springfield, VA 22161.

18. Photometrics Ltd., Tucson, AZ 85706.

19. Color filter glass, Schott Glass Technologies, Inc., Duryea, PA 18642.

20. Color filter glass, Hoya Corporation, Tokyo 161-8525, Japan.

21. S. Skupsky, LLE, private communication (1999).

Nonlinear Evolution of Broad-Bandwidth, Laser-Imprinted Nonuniformities in Planar Targets Accelerated by 351-nm Laser Light

In an inertial confinement fusion (ICF) implosion, the target is hydrodynamically unstable, and, as a result, mass modulations in the target (either existing or created by the drive) can grow sufficiently large to disrupt the implosion, reducing its thermonuclear yield.[1] In direct-drive ICF, the nonuniformities in the drive laser can create mass modulations in the target by a process called laser imprinting. It is, therefore, important to understand the evolution of three-dimensional (3-D) broadband initial spectra produced by laser imprinting. Target designs[2,3] rely on the saturation of unstable growth of these broadband spectra by nonlinear effects (predicted by Haan's model[4]), so it is critical to the success of ICF that this saturation be measured and understood.

The linear growth of the Rayleigh–Taylor (RT) instability has been extensively studied in planar targets accelerated by direct drive (laser irradiation).[5–8] These experiments, generally performed with preimposed two-dimensional (2-D) sinusoidal perturbations, were well simulated by hydrocodes, providing confidence that both the energy coupling and the amount of unstable growth are well modeled. The experiments discussed in this article are closely related to those that measure the growth of preimposed mass perturbations.[5,8] The latter provide a baseline calibration for various hydrodynamic effects that occur in the broadband imprinting experiments.

Nonlinear effects are inherent and very important to the evolution of broadband spectra. Several works[9–13] that used laser imprint as the initial perturbation for RT growth have shown the nonlinear evolution of broadband imprinted features. Because of the complexity of nonlinear physics, however, only a qualitative analysis of broadband saturation was shown.[9–13] In recent years several models have been developed to explain nonlinear RT evolution in Fourier[4,14–18] and real space.[17] Multimode nonlinear behavior has been measured in indirect-drive RT experiments with preimposed 3-D, multimode initial perturbations in planar targets.[19,20]

Recent work has shown experimentally[21] that three-dimensional broadband imprinted features exhibit growth that saturates at amplitudes consistent with Haan's model.[4] Here we extended that work to provide a more-detailed analysis of the RT nonlinear evolution of the broadband spectra seeded by laser nonuniformities. In our experiments we used predominantly 20-μm-thick CH targets, which closely resemble the target shells typically used on OMEGA spherical implosions. On OMEGA,[22] the planar targets were accelerated by 351-nm laser beams. Various experiments were performed by different beam-smoothing techniques including distributed phase plates (DPP's),[23] smoothing by spectral dispersion (SSD),[24] and distributed polarization rotators (DPR's).[9,10] Through-foil x-ray radiography was used to measure mass modulations created in planar targets as a result of imprinting and subsequent growth.[25,26] Experimental data are compared with predictions of the Haan model for the evolution of broadband perturbation spectra. The limitations of RT growth by finite target thickness and target "bowing" due to decreased drive toward target edges are also discussed in this article.

It should be noted that the RT instability studied here exists primarily at the ablation surface, the point where the steep temperature front meets the cold overdense material of the shocked target. Perturbations in the target result from both mass modulations (ripples at the ablation surface) and density modulations produced in the bulk of the target. The latter are created primarily by the propagation of nonuniform shocks[5,27,28] produced by intensity nonuniformities in the laser drive that modulate the drive pressure. Through-foil radiographic systems are sensitive to the density–thickness product (optical depth) of the target and, as such, cannot distinguish between mass and density modulations.[5,8] After about 1 ns of acceleration in these experiments, the variations in optical depth produced by the nonuniform shocks become negligible compared to those produced by the ablation-front amplitude. At this point, it is reasonable to ascribe most of the modulation in measured optical depth to the amplitude of the perturbations at the ablation surface.[5]

The next four sections of this article describe experimental configuration, Haan's model for nonlinear saturation of broad-

band nonuniformities, data analysis techniques, and measurements of saturation levels for broadband spectra. The last four sections discuss late-time evolution of broadband spectra, target bowing, limitations of RT growth by finite target-thickness effects, and, finally, results.

Experimental Configuration

Initially smooth, 20- and 40-μm-thick CH targets (ρ = 1.05 g/cm^2) were irradiated at 2×10^{14} W/cm^2 in 3-ns square pulses by five overlapping UV beams (see Fig. 79.40). All five beams had distributed phase plates (DPP's)[23] to enhance the on-target uniformity. Each of the drive beams was focused to a ~900-μm-diam spot size (at the 5% intensity contour) with an on-target intensity distribution measured to be $I \sim \exp\left[-\left(r/r_0\right)^4\right]$.[8] The energy per beam delivered on a target was ~400 J. For some shots SSD[24] and DPR's[9,10] were used. The 2-D SSD had IR bandwidths of 1.25 Å × 1.75 Å producing a 0.25-THz bandwidth at 351 nm. The resultant, five-beam overlapped spot (time integrated) had a constant-intensity region of ~600-μm diameter. The experiments were conducted with three different configurations of beam-smoothing techniques: (1) with DPP's, (2) with DPP's and SSD, and (3) with DPP's, SSD, and DPR's. The on-target uniformity for these cases can be estimated by dividing the time-integrated, single-beam nonuniformities (98%, 8.5%, and 6%) by the square root of 5 (for five beams), yielding 44%, 3.8%, and 2.7%, respectively, for the three configurations.[9,10] The targets were backlit with x rays produced by a uranium backlighter located 9 mm from the driven target and irradiated at ~1×10^{14} W/cm^2 (using 12 additional beams). X rays transmitted through the target and a 3-μm-thick aluminum blast shield (located between the backlighter and drive foils) were imaged by 8-μm pinholes on an x-ray framing camera filtered with 6 μm of aluminum. This yielded the highest sensitivity for an average photon energy of ~1.3 keV. The distance between the target and the pinhole array was 2.9 cm, and the distance between the pinhole array and the framing camera was 35 cm, resulting in a magnification of ~12. The framing camera produced eight temporally displaced images, each of ~80-ps duration. The use of optical fiducial pulses coupled with an electronic monitor of the framing camera output produced a frame-timing precision of ~70 ps. The framing camera images were captured on Kodak T-Max 3200 film, which was digitized with a Perkin-Elmer PDS microdensitometer with a 20-μm-square scanning aperture. The measured target optical depth is the natural logarithm of the intensity-converted images of a target.

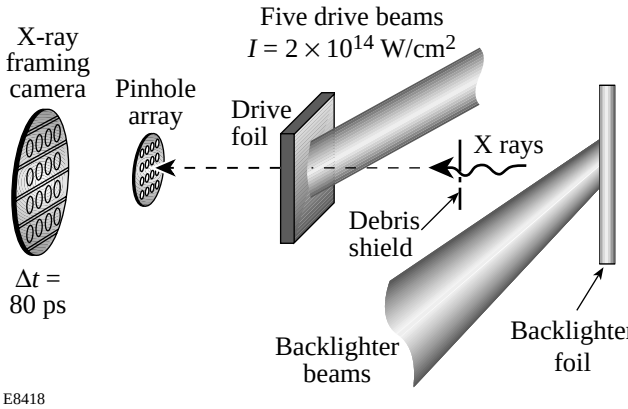

Figure 79.40
Experimental configuration. Five overlapped beams drive a 20-μm-thick CH foil. An additional 12 beams produce x rays from a uranium backlighter foil. X rays traverse the target and are imaged by a pinhole array on a framing camera.

The experiment involved multiple shots where radiographs were obtained at different times. For each shot, up to six images of the same area (400 μm square) of the target (found by the cross-correlation method described later in this article) were analyzed. These images were acquired in time intervals 1.0 to 2.8 ns after the beginning of the drive. The backlighter shape was removed by subtracting a fourth-order, two-dimensional envelope fit to data. The resulting images were the measured modulations of optical depth $D_m(\mathbf{f})$. Using the measured system resolution, noise, and sensitivity, we applied a Wiener filter to reduce noise and deconvolved the system's modulation transfer function (MTF) to recover the target's areal-density modulations $D_t(\mathbf{f})$.[26] The noise in these measurements was dominated by photon statistics of the backlighter x rays, and the system resolution was limited by an 8-μm pinhole.[26]

The primary objective of this experiment is to recover the amplitude of the perturbation at the ablation surface using the measured optical-depth modulations. To do this rigorously requires significant effort. One approach is to use computer simulations of the experiment and detection system to quantify the relationship between modulations in the radiographs and perturbations in the target.[29] Since three-dimensional simulations of laser-imprinted perturbations are difficult, it is advantageous to obtain this relationship experimentally. We simplify the latter process by establishing several reasonable assumptions about the detection system. First, as a result of Al filters, a relatively narrow band ($\Delta E \simeq 200$ eV) of x rays around 1.3 keV is used for radiography. Around 3.5 keV (uranium M-band emission) the spectral component's effect on system

sensitivity and resolution was measured and calculated to be negligible.[26] Second, the backlighter spectrum and filter transmission remain constant during the measurement. Third, the backlighter is produced by 12 beams with phase plates, resulting in a very uniform and predictable backlighter shape. Fourth, there is little heating of the solid part of the target; therefore, the mass absorption coefficient μ is constant in time. Fifth, the amplitudes of the growing imprinted features are large enough that the propagation of a nonuniform shock has little effect on the total optical depth of the target.[5] Given these assumptions, the measured optical depth and the optical depth of the target (areal density) are linearly related as

$$D_m(\mathbf{r},t) = \int d\mathbf{r}' R_{\text{sys}}(\mathbf{r}-\mathbf{r}') D_t(\mathbf{r}',t), \tag{1}$$

where R_{sys} is the point spread function (PSF) of the entire system. The latter is the convolution of the PSF's of the pinhole, the framing camera, the film, and the digitizing aperture of the densitometer. In frequency space, the total system modulation transfer function (MTF) is the product of the MTF's of each of these components. Equation (1) has been derived assuming that the amplitude of the target's optical-depth modulations is small compared to unity. Since Eq. (1) is a linear approximation, it does not treat the generation of harmonics and coupling of modes produced by nonlinearities in the detection system. We have simulated these nonlinearities for modulation amplitudes greater than those measured routinely in our experiments and found that nonlinear effects were negligible compared to the noise in the system. This knowledge was used to create a Weiner filter that uses a linear approximation to the detection system in order to recover the target areal-density modulations.[26]

As an example, Fig. 79.41 shows a fully processed image of the target optical depth at 2.4 ns for a shot with all of the laser-smoothing techniques (DPP's, SSD, and DPR's) employed. The range of 3.6 OD corresponds to a target areal-density (ρR) modulation of about 3.6×10^{-3} g/cm^2. For comparison, the areal density (ρR) of the undriven target is about 2×10^{-3} g/cm^2.

At early times, the contribution to areal-density modulations in the bulk of a target, produced by the propagation of nonuniform shocks, is comparable to those from amplitude modulation at the ablation surface.[5] After ~1 ns of drive, however, the ablation-front modulations with spatial frequencies in the region 10 to 100 mm^{-1} (where measurements are performed) experience sufficient RT growth to dominate any density modulation produced by nonuniform shocks. Thus, at times >1 ns, the amplitude at the ablation surface is well represented by measured modulations.

Once the modulation in target optical depth $D_t(\mathbf{r},t)$ is obtained, the perturbation amplitude in the target $\xi(\mathbf{r},t)$ can be found using spectrally weighted attenuation length λ_{CH},[26] which is inversely proportional to the mass absorption coefficient and the target density:

$$\xi(\mathbf{r},t) = D_t(\mathbf{r},t)\,\lambda_{\text{CH}}. \tag{2}$$

λ_{CH} can be constructed using the target compression C_p calculated by 1-D hydrocode *LILAC*[30] and the measured attenuation length λ_x of the undriven target:

$$\lambda_{\text{CH}} = \frac{\lambda_x}{C_p}. \tag{3}$$

This relation can be used as long as the driven target maintains the cold value of its mass absorption coefficient. Typically, during our experiments the calculated target temperature ($T < 10$ eV) is far below the values that could change the mass absorption coefficient to ~1-keV x rays. λ_x was measured by radiographing undriven, 20-μm-thick CH targets that had

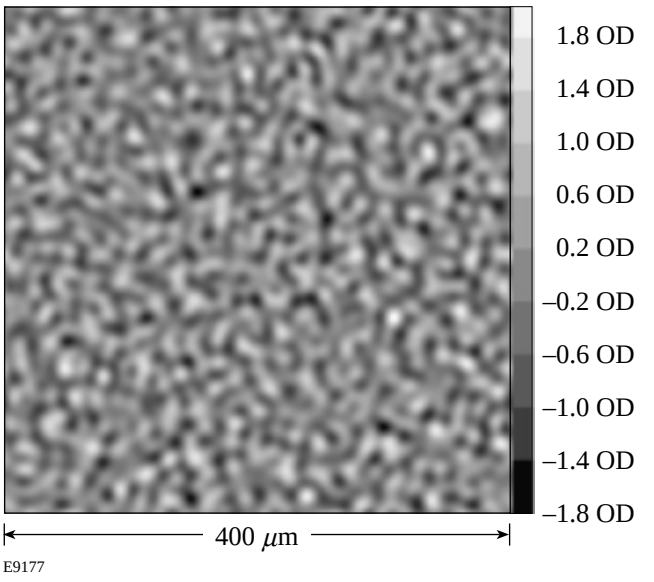

Figure 79.41
Fully processed image of the target optical depth (OD) perturbations captured at 2.4 ns for one of the six shots with all smoothing techniques including DPP's, SSD, and DPR's.

preimposed, low-amplitude (0.5-μm) sinusoidal modulations with wavelengths of 60 and 30 μm. Using these modulations as control references, λ_x was determined to be 10±2 μm. These experiments also showed that both backlighter spectrum and filter transmission remained constant during the measurements.

Haan's Model for Broadband Spectra

In the linear regime of the RT instability, individual modes do not interact and therefore grow exponentially at rates determined by the dispersion relation[31–33]

$$\gamma = \alpha\sqrt{\frac{kg}{1+L_m k}} - \beta k V_a , \tag{4}$$

where γ is the instability growth rate, k is the wave number of the perturbed mode, g is the target acceleration, L_m is the minimum density-gradient scale length, and V_a is the ablation velocity. For CH targets L_m ~1 μm and the constants have values of $\alpha \sim 1$ and $\beta \sim 1.7$. Equation (4) determines how the actual growth rate differs from the classical rate $\gamma \sim \sqrt{kg}$ as a result of density scale length and ablation. For a single-mode initial perturbation, nonlinear effects cause the exponential growth of the mode to saturate at an amplitude $\xi_k \simeq 0.1\,\lambda$ and to subsequently grow linearly in time.[4] Harmonics of the fundamental mode are generated by mode coupling[14] during the exponential growth (in linear phase), leading to the formation of bubbles (penetration of lighter fluid into heavier) and spikes (penetration of heavier fluid into lighter).

The evolution of 3-D broadband perturbations is more complicated. The fastest-growing modes rapidly drive harmonics and coupled modes. The contribution of the mode coupling becomes comparable to the exponential growth for some of the modes, even at small (in the linear regime) amplitudes. As a result, some modes grow faster than others, while some shrink and change their phase;[18] however, the average amplitude of all of the modes at a given spatial frequency grows exponentially at a rate given by Eq. (4).[4,14] Saturation occurs due to the collective behavior of modes because adjacent modes can constructively interfere to create local structures with amplitudes much larger than those of individual modes. As these features experience saturation, the individual modes saturate at amplitudes much less than 0.1 λ. After reaching this saturation level, the modes grow, on average, linearly in time. The transition from the linear (exponential growth) to the nonlinear stage (linear growth) is continuous. Haan formulated a model[4] for the saturation of a 3-D broadband spectrum and found a saturation level of the azimuthally averaged amplitude given by[15,16]

$$S(k) = 2/Lk^2 , \tag{5}$$

where L is the size of the analysis box. The L dependence occurs because the individual Fourier amplitudes of the broadband features depend on the size of analysis region; whereas the rms amplitude $\sigma_{\rm rms}$, a measure of the deviation of the function $\xi(\mathbf{x})$ from its average value $\bar{\xi}$, does not. Using the Fourier transform $\xi(\mathbf{k})$ of the function $\xi(\mathbf{x})$, the rms amplitude $\sigma_{\rm rms}$ is defined as

$$\sigma_{\rm rms} = \sqrt{\sum_k \left|\xi(\mathbf{k})\right|^2 - \left|\xi(\mathbf{k}=0)\right|^2} . \tag{6}$$

The rms amplitude is the physically measurable quantity and therefore must have the same value independent of how it is derived. The number of Fourier modes decreases as the box size is reduced. The nonuniformity's $\sigma_{\rm rms}$ is the square root of the sum of all modes' absolute values squared, as shown by Eq. (6), so the amplitudes of the modes must, concomitantly, increase to keep the nonuniformity's $\sigma_{\rm rms}$ constant.

After it reaches the saturation level $S(k)$, the evolution of the average amplitude $\xi_k(t)$ is given by[4]

$$\xi_k(t) = S(k)\left[1 + \ln\left(\frac{\xi_k^{\rm exp}(t)}{S(k)}\right)\right], \tag{7}$$

where $\xi_k^{\rm exp}(t) = \xi_k(t=0)\exp(\gamma t)$ is the exponential growth in the linear stage of instability. This is equivalent to growth at a constant velocity $V(k)$ in the saturation regime

$$V(k) = S(k)\gamma(k). \tag{8}$$

The behavior predicted by this model is shown in Fig. 79.42 for an initial perturbation spectrum that had constant power per mode as a function of spatial frequency. This is representative of the broadband features imprinted by irradiation nonuniformities that arise primarily from the speckle pattern produced by DPP's and SSD.[34] The evolution of this spectrum (plotted as the average amplitudes versus spatial frequency for seven different times between t = 1.3 to 2.2 ns) is modeled simply by applying the growth-rate dispersion relation [Eq. (4)], the saturation level [Eq. (5)], and the evolution in the saturation regime [Eq. (7)], where the target acceleration g = 50 μm/ns^2, ablation velocity V_a = 2.5 μm/ns, and the

nonuniformity's initial σ_{rms} = 0.09 μm. The amplitudes are converted to target optical depth by dividing by the measured, spectrally weighed, attenuation length λ_x = 10±2 μm and multiplying by the simulated compression of the target (about 2 for 1.5 ns). The simulated target density at the ablation surface is shown in Fig. 79.43. The high-frequency modes grow most rapidly and saturate at the level given by Eq. (5), while the low-frequency modes grow more slowly. As a result, the mid-frequency modes experience the largest growth factors, producing a peak in the spectrum. As the evolution progresses, the mid-frequency modes begin to saturate, and the peak moves to longer wavelengths. This behavior is relatively insensitive to the initial spectrum or drive conditions; therefore, most broad-bandwidth initial spectra will evolve similarly given sufficient time. Variations in growth rates of up to 50%, or in the σ_{rms} of the initial spectrum of up to two orders of magnitude, have little effect on the predicted spectral evolution; the only requirement is that the spectrum be broadband. For example, according to Haan's model the initial perturbation spectrum that has constant Fourier amplitude and σ_{rms} = 0.5 μm undergoes similar evolution to that shown in Fig. 79.42 but it occurs at earlier times (between t = 0.8 to 1.6 ns) if the drive conditions are the same. This behavior has been tested experimentally by varying amplitudes of initial perturbation using a variety of laser-smoothing techniques.

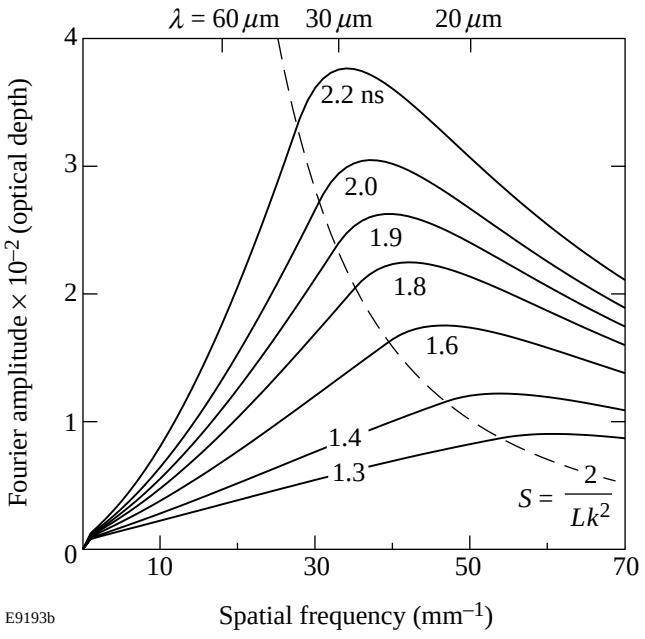

Figure 79.42
Predicted Fourier amplitudes of optical depth using Haan's model for an assumed spectrum of perturbations with initial flat power per mode (σ_{rms} = 0.09 μm) spectrum, target acceleration of g = 50 μm /ns^2, ablation velocity of V_a = 2.5 μm /ns, and L = 400 μm at times 1.3, 1.4, 1.6, 1.8, 1.9, 2.0, and 2.2 ns. Haan's saturation amplitude S is shown by the dashed line.

Image Cross-Correlations

The experiment involves multiple shots with CH targets and with different smoothing techniques applied. For each shot, up to six unfiltered images of the same area of the target, found with a cross-correlation technique, were processed with a 400-μm analysis box. Figure 79.44 shows two images of the target acquired at 2.4 ns and 2.5 ns for a shot with all smoothing techniques employed. The same 400-μm-sq area of the target was found in each of these images when the cross-correlation between the two analysis regions was maximized. The cross-

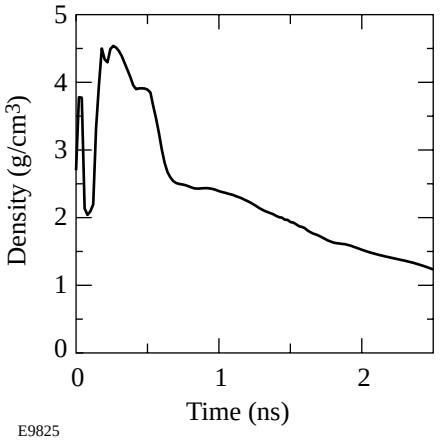

Figure 79.43
Calculated target density at the ablation surface as a function of time.

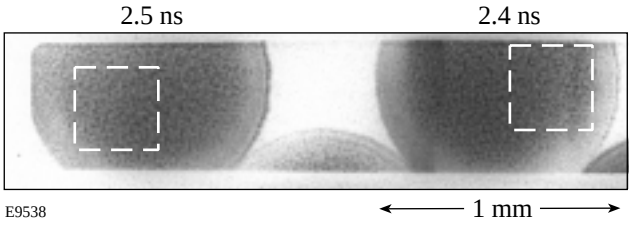

Figure 79.44
Two images of the target acquired at 2.4 ns and 2.5 ns for a shot with all smoothing techniques employed. Two 400-μm-square regions indicated by the square boxes were taken for cross-correlation analysis.

correlation function for two images with target optical depths $D_{t1}(\mathbf{r})$ and $D_{t2}(\mathbf{r})$ is given by

$$C(\mathbf{r}) = \frac{\int d\mathbf{r}' D_{t1}(\mathbf{r}' + \mathbf{r}) D_{t2}(\mathbf{r}')}{\sqrt{\int d\mathbf{r} D_{t1}(\mathbf{r})^2 \int d\mathbf{r} D_{t2}(\mathbf{r})^2}}. \quad (9)$$

If two images of the target are shifted by some distance a, then the maximum of the cross-correlation function $C(\mathbf{r})$ will be shifted by the same distance from the center of coordinates ($\mathbf{r} = 0$), as can be seen from Eq. (9). For example, if two images at 2.4 ns and 2.5 ns are misaligned by $a_x = 133$ μm in horizontal and $a_y = 67$ μm in vertical directions, the peak of the cross-correlation function between these two images is shifted from the center of coordinates by the same distances a_x and a_y as shown in Fig. 79.45(a). When one of the images is moved by the distances a_x and a_y, aligning these two images, the peak of the cross-correlation function moves toward the center of coordinates as shown in Fig. 79.45(b). At the same time, the cross-correlation coefficient between these two images, which is defined as the maximum of $C(\mathbf{r})$, increases from 17% for misaligned images to 34% for aligned images because larger areas of the target overlap for two aligned images.

The details of target nonuniformity structure are unique and specific only to images taken at the same shot. It is therefore expected that the cross-correlation technique should find little correlation between two images taken from different shots. The typical cross-correlation function of two images taken on different shots is shown in Fig. 79.45(c). This function has no

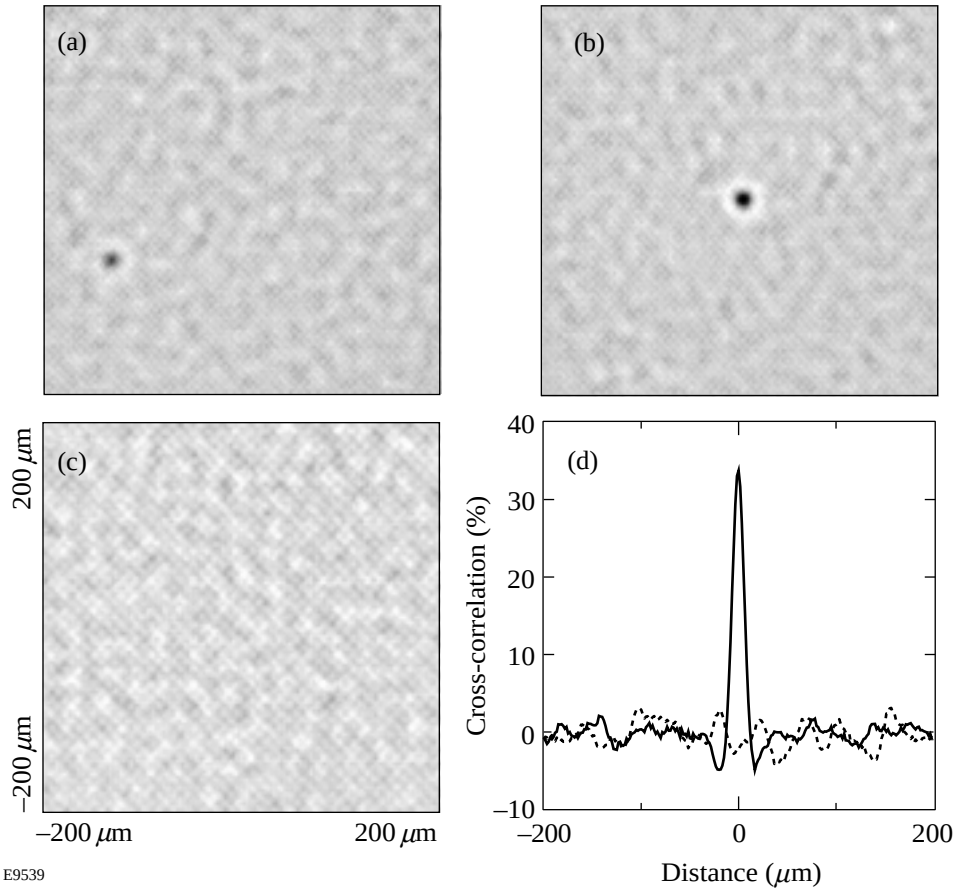

Figure 79.45
The cross-correlation function between two images. (a) Two images are shifted by 133 μm in the horizontal direction and 67 μm in the vertical direction, respectively. The cross-correlation coefficient between the two images is 17%. (b) When two images are aligned, the maximum of the cross-correlation function is then located at the center of coordinates at $\mathbf{r} = 0$. The cross-correlation coefficient between the two images increases to 34%. (c) The cross-correlation function between the two images taken on different shots showing little correlation. (d) The lineout through the center of coordinates of the cross-correlation function shown in (c) for two images taken at different shots (dashed line). The lineout through the center of coordinates of the cross-correlation function shown in (b) for 2.4-ns and 2.5-ns images taken during the same shot (solid line).

pronounced peaks; it fluctuates around zero, as shown by the dashed line in Fig. 79.45(d), which is the lineout of this function through the center of coordinates. This indicates that there is no correlation between features in images from different shots. In contrast, images taken on the same shot (such as those acquired at 2.4 and 2.5 ns and shown in Fig. 79.44) are well correlated. This is shown by the lineout through the center of their cross-correlation function as shown in Fig. 79.45(d) by the solid line. The cross-correlation between images greatly increased after they were Wiener filtered: for example, the cross-correlation coefficient between these images increased from 34% to 70%. This indicates that the image processing efficiently reduced the noise in these images. The upper limit of the cross-correlation is determined by the amount of evolution the target perturbations experienced between the times the images were captured.

The accuracy of the image alignment using the cross-correlation technique has been defined in the following way: For a particular shot, five images (A, B, C, D, and E) were aligned with a sixth image (F) by moving the peaks of all five cross-correlation functions toward their centers of coordinates. Then each of the five images was cross-correlated to each other. It was found that the peaks of all these cross-correlation functions were located no farther than 1 pixel (1.67 μm) from the centers determined by the first step. This indicates that the accuracy of the alignment is not worse than 2 μm.

Figure 79.46 shows six fully processed (Wiener-filtered) sub-images (L = 100 μm) of the target optical depth for one of the shots with full smoothing (DPP's, SSD, and DPR's applied) captured at 1.6, 1.9, 2.0, 2.2, 2.4, and 2.5 ns and aligned by the cross-correlation technique. The temporal evolution to longer-scale structures is evident. All images are well correlated indicating that the evolution is of the same features. Figure 79.47 shows the cross-correlation coefficients $C(\mathbf{r}=0)$ between these different images. The solid line shows that the cross-correlation C ($\mathbf{r}$ = 0) of the image at 2.5 ns with itself equals 1 (at 2.5 ns) and its cross-correlation with other images (at other times) decreases as a time separation between images increases. The dashed line in Fig. 79.47 shows the same behavior for the cross-correlation of the image at 2.2 ns with the other images. In fact, the same behavior has been observed for each time frame in all six shots, i.e., the cross-correlation between neighboring images is always higher than with more-distant images, which confirms that the image processing allows an observation of the evolution of the same features of target perturbations.

Nonlinear Saturation of RT Growth

As was pointed out earlier, predictions by the Haan's model for the shape of the late-time spectrum are relatively insensitive to the initial perturbation spectrum; therefore, most broad-bandwidth initial spectra evolve similarly. Variations of up to two orders of magnitude in the initial amplitudes of the spectrum have little effect on the predicted spectral evolution. This prediction has been tested experimentally by varying the amplitudes of initial perturbation using different laser-smoothing techniques. The primary experiment involves multiple shots with planar, 20-μm-thick CH targets taken with different smoothing techniques employed: with DPP's, SSD, and DPR's (six shots), with DPP's and SSD (three shots), and with DPP's only (two shots).

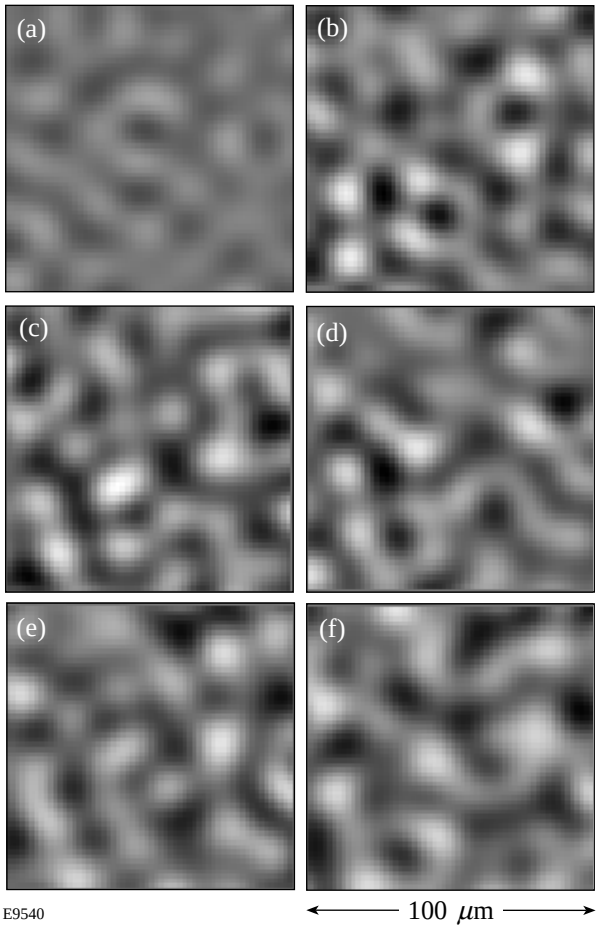

Figure 79.46
Fully processed sub-images (with a box size of 100 μm) of the target optical depth captured at (a) 1.6, (b) 1.9, (c) 2.0, (d) 2.2, (e) 2.4, and (f) 2.5 ns for one of the six shots taken with laser conditions that include DPP's, SSD, and DPR's. The evolution in time to longer-scale structures is evident.

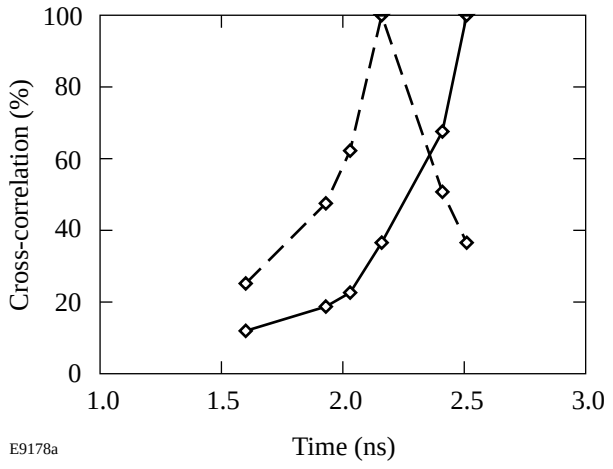

Figure 79.47
Cross-correlation of different time images for one of the six shots taken with laser conditions that include DPP's, SSD, and DPR's. The cross-correlation coefficients of images captured at 2.5 ns and 2.2 ns with all other images are shown by the solid line and the dashed line, respectively.

The evolution of the averaged amplitudes (obtained by azimuthally averaging the Fourier amplitudes at each spatial frequency) of the measured target's optical-depth modulation as a function of spatial frequency with planar, 20-μm-thick CH targets is shown in Fig. 79.48(a) for one shot at times of 1.4 to 2.2 ns and in Fig. 79.48(b) for another shot at somewhat later times of 1.6 to 2.4 ns. In these shots laser beams had full smoothing techniques employed (i.e., DPP's, SSD, and DPR's). Figures 79.48(c) and 79.48(d) show the evolution of nonuniformity spectra for shots with DPP's and SSD for times of 1.6 to 1.9 ns for one shot and of 1.6 to 2.0 ns for the other, and Figs. 79.48(e) and 79.48(f) for shots with DPP's only for times of 1.3 to 1.5 ns for one shot and of 1.6 to 1.8 ns for the other. The initial amplitudes of imprinted perturbations are expected to be higher in shots with less laser uniformity.

One can readily see that the measured spectra are peaked and that the peak shifts toward longer wavelengths as time progresses, similar to the predicted behavior shown in Fig. 79.42. Moreover, the dashed line, which shows the Haan saturation level, is in good agreement with the position of the spectral peak. The saturation level was converted to optical depth using the spectrally weighed attenuation length λ_x and the predicted compression (about 2 at times ~1 to 2 ns). Similar behavior was observed for all shots taken under all drive conditions with different smoothing techniques employed. For the data with less laser uniformity [Figs. 79.48(e) and 79.48(f), DPP's only], the initial imprinted amplitudes are higher, and as a result, the RT evolution is observed earlier in time than in the case with more-uniform drive, which includes SSD and DPR's [Figs. 79.48(a) and 79.48(b)].

Figure 79.48 shows that the measured growth of the amplitudes at 20-μm wavelength is much less pronounced than that of 30 μm for all shots. This is because the amplitudes at 20 μm are predicted to be already above Haan's saturation level at about 0.01 OD, while amplitudes at 30 μm experience a transition from exponential growth to the saturated growth with constant velocity at about 0.022 OD. The amplitude at 60 μm is predicted to be below the saturation level and therefore should grow exponentially during this time interval. To support these assertions, we measured the growth of low-amplitude, preimposed, 2-D, 60-μm-wavelength and 30-μm-wavelength, single-mode, sinusoidal perturbations on 20-μm-thick CH foils driven with the irradiation conditions that included DPP's, SSD, and DPR's. Targets with initial perturbation amplitudes of 0.05 and 0.125 μm at 60-μm wavelength and 0.025 μm at 30-μm wavelength were used. These initial amplitudes are sufficiently low that they are expected to be in the linear regime for at least 2.5 ns, yet have high enough amplitudes that mode coupling from the broadband spectrum has no effect on their evolution. Figure 79.49(a) shows that the broadband features at 60 μm (the combined data from six shots) grow at a similar rate as the preimposed 60-μm modulations (upper data points for two shots). Exponential fits to these data (three solid lines) indicate growth rates of 0.96 $\pm$0.02 ns^{-1} and 1.02$\pm$0.02 ns^{-1} for the preimposed modulations and 0.91$\pm$0.05 ns^{-1} for the broadband modulations. Figure 79.49(b) shows that the broadband features at 30 μm (the combined data from six shots) experience a transition from linear to nonlinear phases at an amplitude of about 0.02 OD, which is 30 times lower than the single-mode saturation value of 0.6 OD (0.1 λ). At the same time, the two preimposed 30-μm modulations (upper data points) grow exponentially with growth rates of 1.45$\pm$0.02 ns^{-1} and 1.54$\pm$0.02 ns^{-1}, respectively. These data clearly show the wavelength-dependent saturation level.

The preimposed 30-μm and 60-μm modulations were fitted with an exponential in order to compare growth rates with those measured for early times[5,8] (see later in the **Finite Target Thickness Effect** section). For broadband modulations, both exponential and polynomial fits have been used to quantify the transition from the exponential to saturated growth. Figure 79.49(b) shows that for broadband modulations at 60 μm, the exponential fit (solid line) closely matches the third-order polynomial fit (dashed line). The standard deviations are 0.0021 OD and 0.0022 OD, respectively. For 30-μm broadband modulations shown in Fig. 79.49(b), however, the expo-

nential (dashed line) does not fit data well (the standard deviation is 0.0039 OD) compared to the polynomial fit (solid line; the standard deviation is 0.0022 OD), which closely follows the saturated evolution of these broadband data.

Figure 79.50 summarizes data from 11 shots performed with (1) DPP's, SSD, and DPR's [six shots, Figs. 79.50(a), 79.50(d), and 79.50(g) for the average broadband amplitudes at wavelengths of 60 μm, 30 μm, and 20 μm, respectively],

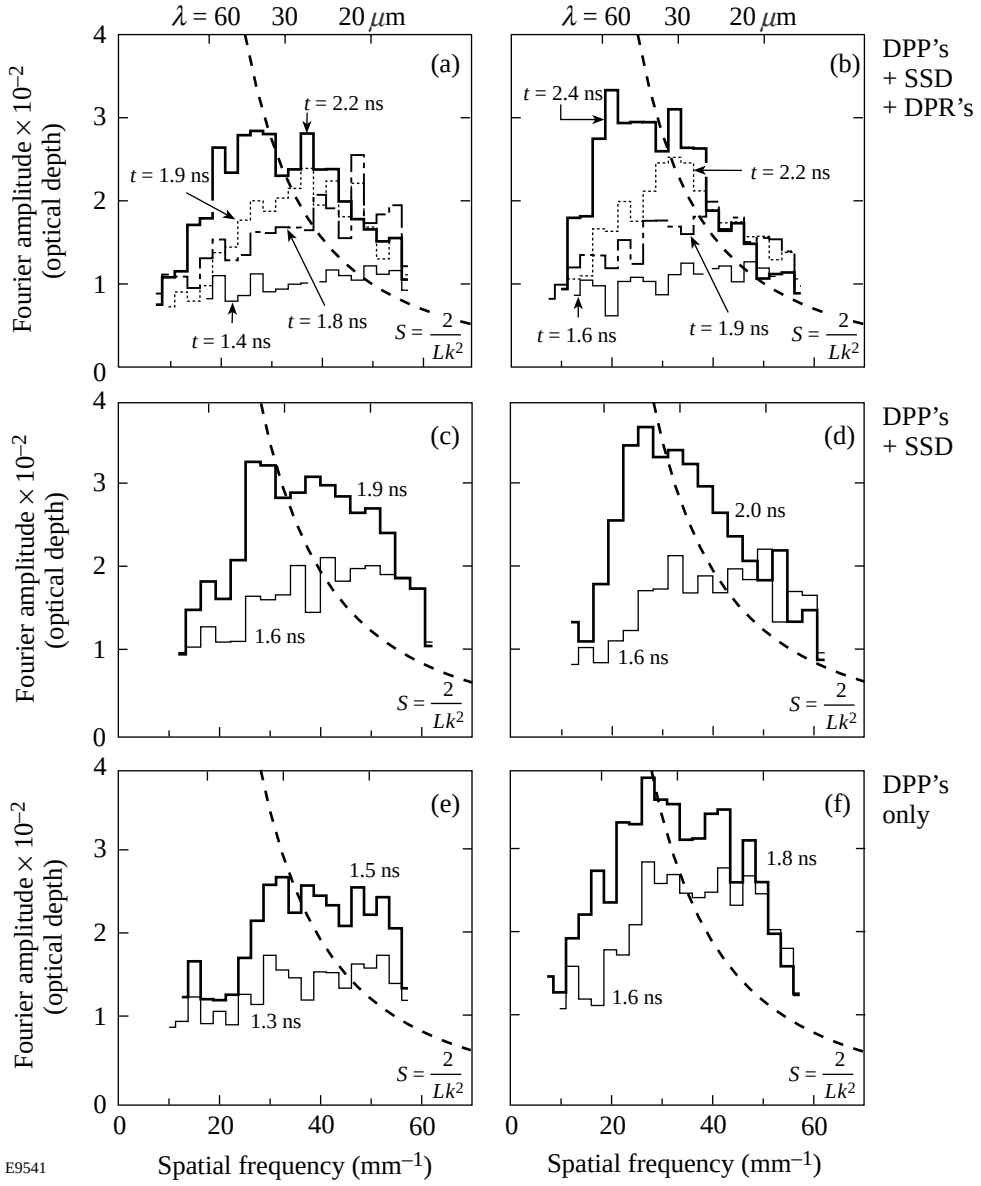

Figure 79.48
The measured azimuthally averaged Fourier amplitudes of the optical-depth modulations as a function of spatial frequency for six shots: (a) a 20-μm-thick foil at times 1.4, 1.8, 1.9, and 2.2 ns with laser conditions that include DPP's, SSD, and DPR's; (b) at 1.6, 1.9, 2.2, and 2.4 ns with DPP's, SSD, and DPR's; (c) at 1.6 and 1.9 ns with DPP's and SSD; (d) at 1.6 and 2.0 ns with DPP's and SSD; (e) at 1.3 and 1.5 ns with DPP's; and (f) at 1.6 and 1.8 ns with DPP's. Haan's saturation amplitude S is shown by the dashed line.

(2) DPP's and SSD [three shots, Figs. 79.50(b), 79.50(e), and 79.50(h)]; and (3) DPP's only [two shots, Figs. 79.50(c), 79.50(f), and 79.50(i)]. It is expected that SSD smoothes out perturbations at high spatial frequencies much more efficiently than at low spatial frequencies;[34] therefore, the expected initial imprinted spectra with and without SSD have not only different nonuniformities σ_{rms}, but also different shapes. According to Haan's model, however, later in time, and after considerable RT growth, the perturbation spectra are expected to be similar but shifted in time with the evolution occurring later in the case of DPP's plus SSD compared to DPP's only.

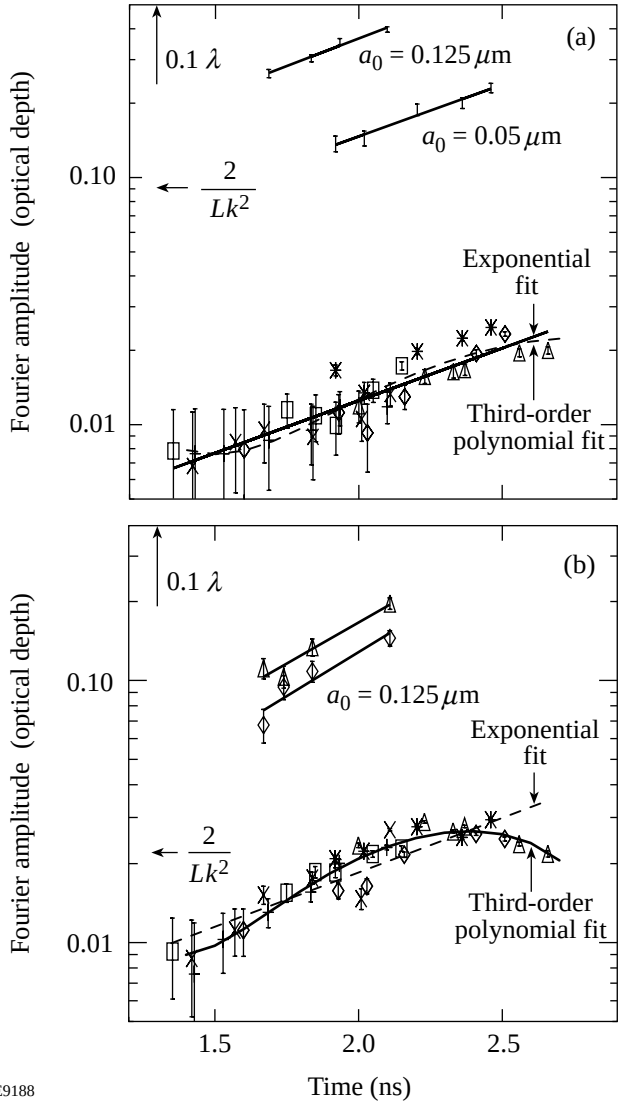

Figure 79.49
(a) Average Fourier amplitudes of optical depth of imprinted features versus time at 60-μm wavelength for six shots (distinguished by different symbols) and the amplitude of preimposed 60-μm perturbations of corrugated targets with initial amplitudes of 0.05 and 0.125 μm (upper data). (b) The same for the 30-μm wavelength with the amplitudes of initial, preimposed, 30-μm perturbations of 0.025 μm (upper data). Exponential fits (solid lines) were used for the preimposed corrugation data, 60-μm imprinted data (solid lines), and 30-μm imprinted data (dashed line), and a third-order polynomial fit was used to the imprinted data at 60 μm (dashed line) and 30 μm (solid line).

The measured temporal evolution for all three cases is similar, as evident from the evolution of the amplitudes of broadband perturbations at 60-μm, 30-μm, and 20-μm wavelengths. The 30-μm- and 20-μm-wavelength perturbations saturate at different times for different smoothing conditions but always at the same levels. The 60-μm perturbations grow in the linear regime (exponential growth) with similar growth rates (0.70±0.05 ns^{-1}, 0.93±0.05 ns^{-1}, and 0.91±0.05 ns^{-1} with DPP's only; DPP's and SSD; and DPP's, SSD, and DPR's, respectively, for all smoothing conditions). As shown earlier, these growth rates are in very good agreement with the measured growth rates of preimposed 2-D sinusoidal perturbations at a 60-μm wavelength [Fig. 79.49(a), upper data points].

For cases with less laser uniformity [case (3): DPP's only], the initial imprinted amplitudes are higher, and as a result, the RT evolution is advanced in time [~250 ps earlier than in case (2), and ~500 ps earlier than in case (1)]. This observation is evident for the 60-μm, 30-μm, and 20-μm wavelengths of broadband perturbations. Note also that the 30-μm-wavelength perturbations saturate at higher amplitude than the 20-μm perturbations, as expected.

Even though the experimental data (see Fig. 79.48) cannot show the saturation level $S(k) = 2/Lk^2$ explicitly, it was tested by comparing peaks of measured Fourier spectra with those predicted by using Haan's model. Such comparison becomes possible because the shape of Fourier spectra and the position of their peaks depend primarily on the saturation level rather than on the initial or drive conditions (shown experimentally in Fig. 79.48). For example, from Fig. 79.48(a) one can see that measured spectral peaks at spatial frequencies of 30 mm^{-1} and 50 mm^{-1} are positioned at the values of Fourier amplitudes of approximately 2.7×10^{-2} and 1.2×10^{-2} OD, at times 2.2 ns and 1.4 ns, respectively. The predicted spectral peaks at these spatial frequencies are at the values of approximately 3.7×10^{-2} and 1.2×10^{-2} OD, respectively, as shown in Fig. 79.42.

The main experimental errors in measurements of target optical depth shown in Fig. 79.48 include noise in the experimental system (dominated by photon statistics of the backlighter x rays), uncertainty of the system resolution, and nonlinearities

in the detection system, which was considered to be linear during Wiener filtering and MTF deconvolution.[26] The total uncertainty of optical-depth measurements at the spatial frequency range of 30 to 50 mm^{-1} was determined to be about 10^{-3} OD. It included the relative error of system resolution measurement, which was about 4%, and the uncertainty due to nonlinearity in the detection system, which was about 2% of the noise in the experimental system.[26]

The Haan's model predictions shown in Fig. 79.42 were converted to the optical depth using spectrally weighted attenuation length λ_{CH},[26] which depends on the calculated target compression C_p and the measured attenuation length λ_x of the undriven target [see Eq. (3)]. λ_x was determined to be 10±2 μm,[26] and the target compression was calculated to be about $C_p = 1.7 \pm 0.3$ during the time interval of 1.4 to 2.2 ns.

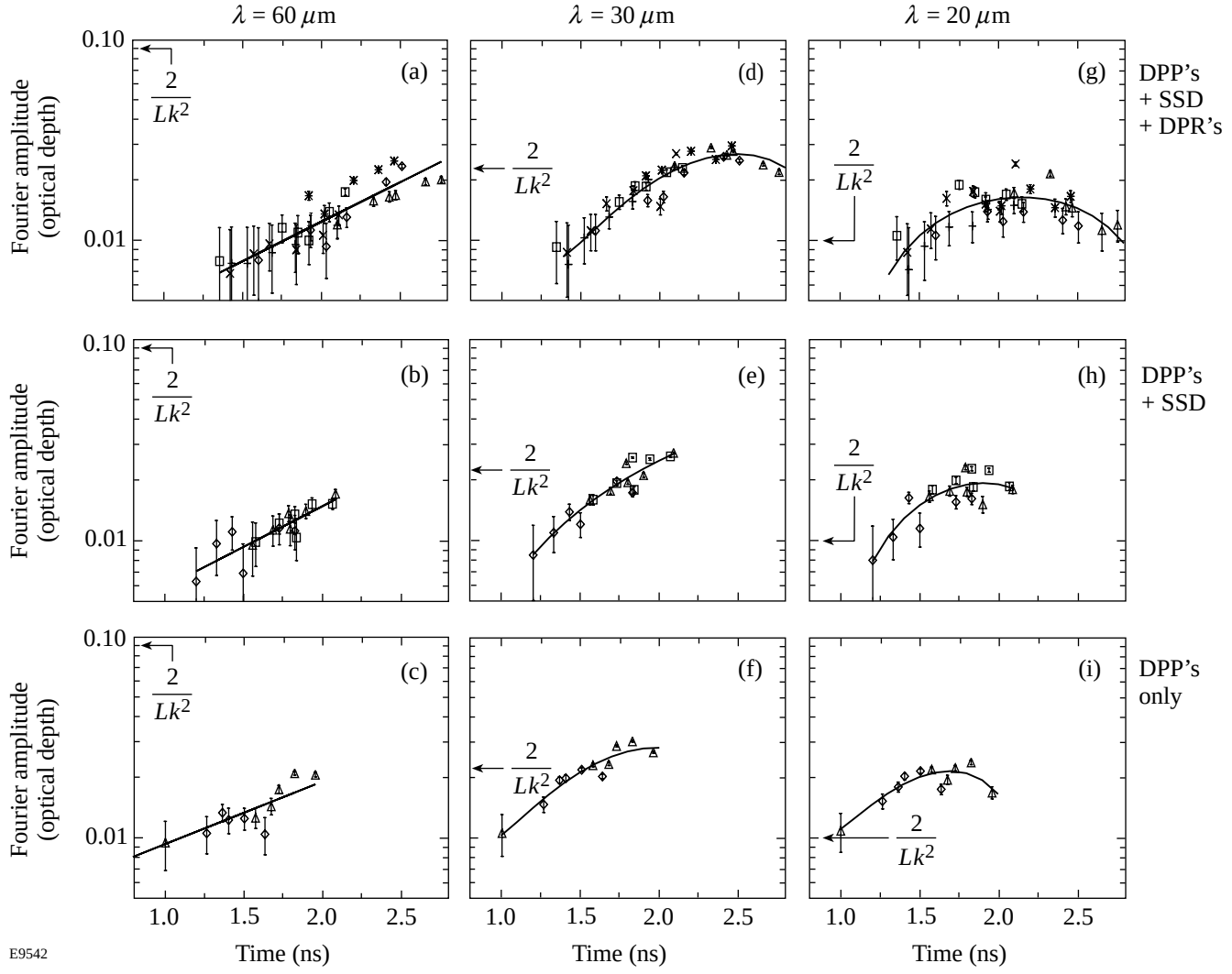

Figure 79.50

(a) Average Fourier amplitudes of optical depth of imprinted features versus time at 60-μm wavelength for six shots (distinguished by different symbols) with DPP's, SSD, and DPR's. Exponential fit (solid line) indicates the growth rate of 0.91±0.05 ns^{-1}. (b) The same for the three shots with DPP's and SSD. Exponential fit (solid line) indicates the growth rate of 0.93±0.05 ns^{-1}. (c) The same for the two shots with DPP's only. Exponential fit (solid line) indicates the growth rate of 0.70±0.05 ns^{-1}. (d) Average Fourier amplitudes of optical depth of imprinted features versus time at 30-μm wavelength for six shots with DPP's, SSD, and DPR's. The solid line is a third-order polynomial fit. (e) The same for the three shots with DPP's and SSD. (f) The same for the two shots with DPP's only. (g) Average Fourier amplitudes of optical depth of imprinted features versus time at 20-μm wavelength for six shots with DPP's, SSD, and DPR's. The solid line is a third-order polynomial fit. (h) The same for the three shots with DPP's and SSD. (i) The same for the two shots with DPP's only.

Using all of these uncertainties, the measured amplitudes of optical-depth modulations that have been converted to perturbation amplitudes in the target [using Eq. (2)] are $15.9 \times 10^{-2} \pm 4.5 \times 10^{-2}$ μm and $7.1 \times 10^{-2} \pm 1.6 \times 10^{-2}$ μm at spatial frequencies of 30 mm^{-1} and 50 mm^{-1}, respectively. Those predicted by Haan's model are 18×10^{-2} μm and 6.0×10^{-2} μm at spatial frequencies of 30 mm^{-1} and 50 mm^{-1}, respectively.

To demonstrate the agreement of these data with the Haan's model, we have compared the measurements and the predictions for the peak of the nonuniformity spectrum in accelerated targets. As has been discussed, the location of the peak follows the predicted trend to longer wavelengths, but it is important to compare the actual amplitude of that peak. Since that amplitude is independent of the initial conditions, we are able to plot together all data shown in Fig. 79.48, irrespective of the different laser-uniformity conditions. Again, the amplitude is obtained using the measured attenuation length of the undriven target and the calculated target compression (Fig. 79.43 shows the density as a function of time). In Fig. 79.51, the amplitudes at which the peaks in the measured spectra occur are plotted versus those for the predicted spectra. These data show that the Haan's model well represents the spectral peaks of broadband nonuniformities.

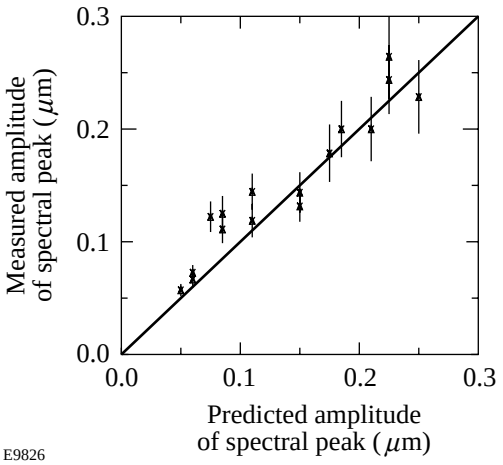

Figure 79.51
The amplitude of measured spectral peak as a function of predicted spectral peak.

In summary, broad-bandwidth perturbations were observed to saturate at levels predicted by Haan's model,[4] which were much lower than the single-mode saturation levels (0.1 λ). This has been shown by the combined data from shots having different drive uniformities. This behavior was noted in both the shape of the spatial Fourier spectra and the temporal behavior of modes at various wavelengths. In addition, it was found that the growth of 3-D perturbations from the broadband spectrum in the linear regime is the same as that for the linear growth of preimposed 2-D perturbations, also in agreement with Haan's model. The measured spectral evolution including the saturation level is insensitive to the details of the initial perturbation spectrum; this is also in agreement with Haan's model.

The relationship between the evolution of the preimposed modes and their coupling to the broadband spectrum must be clarified. The results inferred from Fig. 79.49 require that the growth of the preimposed modes remain in the linear regime (exponential growth) and unaffected by mode coupling. It was experimentally observed that the absolute values of Fourier amplitudes of the broadband spectra are randomly distributed from zero to about twice the average level $2\bar{\xi}_k(t)$ for any azimuthal lineout with wave vector k and at any time t. Therefore, the evolution of any mode $\xi_k(t)$ from the azimuthal lineout at a wave vector k of the broadband spectrum is confined between zero and $2\bar{\xi}_k(t)$. This means that the effects of nonlinear mode coupling on any particular mode $\xi_k(t)$ from all other modes is of the order of $\bar{\xi}_k(t)$ or less. This observation is in agreement with the theoretical work performed by Haan[14] for ablatively accelerated targets. If the amplitude of some particular mode $\xi_k(t)$, growing in the linear regime, is much higher than the average level of broadband spectrum $\xi_k(t) >> \bar{\xi}_k(t)$ as for the preimposed modes from Fig. 79.49, then nonlinear effects will be only a small fraction of its amplitude $\xi_k(t)$. For example, the evolution of the mode $\xi_k(t)$ can be approximated to second-order accuracy and neglecting high-order terms by[14]

$$\xi_k(t) = \xi_k^{\exp}(t) + 1/2\, k\left[\sum_{k'} \xi_{k'}^{\exp}(t)\xi_{k+k'}^{\exp}(t) - 1/2 \sum_{k'<k} \xi_{k'}^{\exp}(t)\xi_{k-k'}^{\exp}(t)\right], \quad (10)$$

where $\xi_k^{\exp}(t) = \xi(t=0)\,\exp[\gamma(k)t]$ is the exponential (or first-order) amplitude of mode k. If the amplitude of some particular mode $\xi_k(t)$, growing in the linear regime, is much higher than the average level of broadband spectrum $\xi_k(t) >> \bar{\xi}_k(t)$ as for preimposed modes from Fig. 79.49, then nonlinear effects will be only a small fraction of its amplitude $\xi_k(t)$ [i.e., the first linear term in Eq. (10) is much larger than the second nonlinear term]. This means that the effect of mode coupling on the amplitudes of 60-μm and 30-μm preimposed modes [which are 10 to 20 times above the average level of broadband

amplitudes (see Fig. 79.49)] is small (of the order of 5% to 10% of their amplitudes) and can be neglected compared with their exponential growth in the linear regime.

The same concept can be expected in a simple physical picture. Figure 79.52 schematically shows an image of the driven target that has a single-mode perturbation (dashed lines) and broadband features with individual 3-D bubbles (solid lines). In some small regions (containing only one or two bubbles), the material flow in the horizontal direction can be dominated by the flow from individual 3-D bubbles. In 3-D, the material from bubbles flows in all directions, but it flows only in one horizontal direction from 2-D bubbles. In the whole region of box size L, however, the material flow in the horizontal direction is dominated by the flow from the tips of the 2-D bubble (dashed lines) because the overall contribution to the flow in this direction from the 3-D bubbles becomes much smaller in the whole region with box size L. Therefore, the overall effect of the broadband features on the evolution of a single mode is insignificant providing that the amplitude of the single mode is high enough. This consideration in real space is complimentary to that in Fourier space described in the previous paragraph.

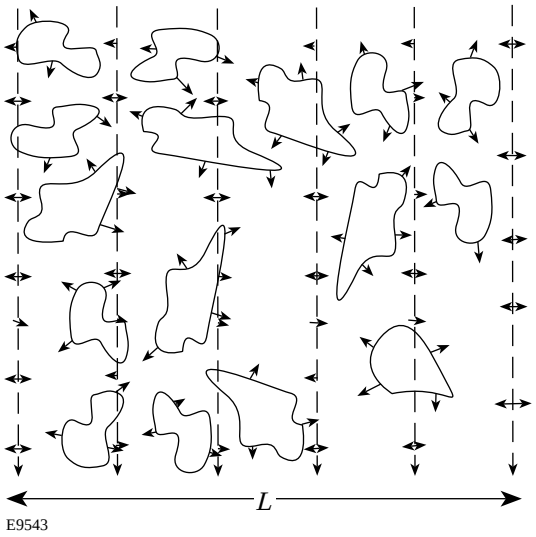

Figure 79.52
Schematic image of the driven target, which has a single-mode perturbation (dashed lines) and broadband features with individual 3-D bubbles (solid lines). In the small regions (containing only one or two bubbles), the material flow in the horizontal direction can be dominated by the flow from individual 3-D bubbles (solid lines). In the whole region with box size L, however, the material flow in the horizontal direction is dominated by the flow from the tips of the 2-D bubble (dashed lines).

Late-Time Perturbation Evolution

In Fig. 79.50, the amplitudes of both the 20-μm- and 30-μm-wavelength broadband perturbations decrease late in time (at 2.5 to 2.8 ns for the case with all smoothing techniques employed). In the nonlinear regime, Haan's model predicts the growth of these perturbations to be linear in time (constant velocity growth) after they reach their saturation levels. This is in contradiction with experimental data. Figure 79.53 shows nonuniformity spectra at 2.5 ns (dashed line) and 2.8 ns (solid line) for one of the shots with all laser-smoothing techniques employed including DPP's, SSD, and DPR's. It clearly shows a decrease in amplitude of all spatial frequencies higher than 30 mm^{-1}. Figure 79.54 shows images of the target at 2.5 ns (a)

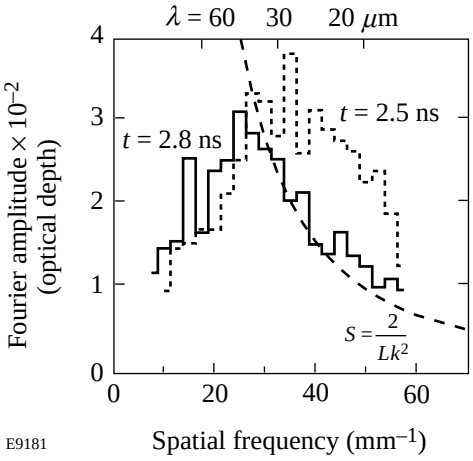

Figure 79.53
Experimentally measured late-time perturbation spectra. Azimuthally averaged Fourier amplitude of the optical-depth modulation as a function of spatial frequency for a 20-μm-thick foil at 2.5 and 2.8 ns and with laser-smoothing techniques including DPP's, SSD, and DPR's. The saturation amplitude S is shown by the dashed line.

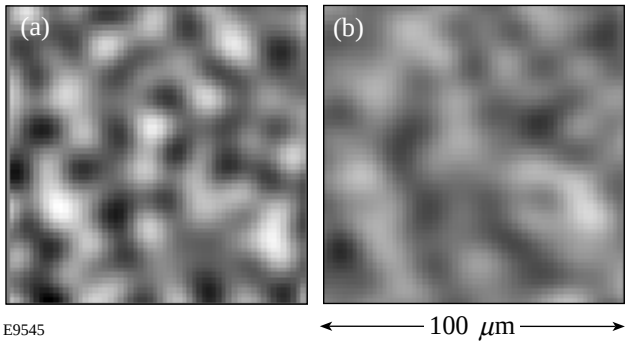

Figure 79.54
Late-time images of the target optical-depth perturbations captured at (a) 2.5 ns and (b) 2.8 ns with a 20-μm-thick target and with laser-smoothing techniques including DPP's, SSD, and DPR's.

and 2.8 ns (b). Compared to the image at 2.5 ns, features in the 2.8-ns image become much more round as neighboring bubbles coalesce, and the typical scale length of all the features becomes larger in the latter image. A 2-D model for bubble competition[17] predicts that such bubble coalescence occurs at higher bubble amplitudes and consequently much farther into the nonlinear regime than shown here. At the end of the drive (~3 ns) 1-D *LILAC* simulations predict an increase in ablation velocity (by a factor of 2) with the target decompressing quickly. In this case, target perturbations in optical depth could decrease because of the stabilizing effect of ablation.

Another possible explanation for the observed spectral behavior is that even earlier in the nonlinear regime (before the bubble coalescence), some short-scale-length bubbles move underneath larger, long-scale-length bubbles because larger bubbles grow faster than smaller bubbles.[17] The areal-density (or optical-depth) measurement becomes insensitive to short-scale-length bubbles because, in the direction of the x-ray propagation, the short-scale-length bubble becomes a part of the long-scale-length bubble, even though physically the two bubbles are still separate.

"Bowing" of the Target

Bowing of the target is another effect that has been observed and quantified in these experiments. Figure 79.55 schematically explains this effect. Before the shot, the CH target is attached to the massive Mylar washer. Without this washer a part of the laser energy from the laser beams, which irradiate the target at non-normal incidence, would miss the target and propagate toward opposing ports of the OMEGA target chamber, threatening to damage the laser system. During the drive, the central ~1-mm portion of a target accelerates, while the portion attached to the washer stays undriven. Toward the end of the drive the target becomes "stretched" (see Fig. 79.55). Experiments performed by Knauer[5] with the same drive condition on similar targets with preimposed 2-D corrugation showed that the wavelength of the corrugations increased 7% to 10% toward the end of the drive. This effect was explained by the target bowing and, as a result, stretching all features on the target, as though they were magnified.

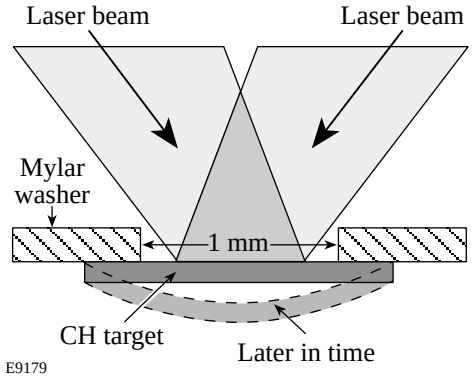

Figure 79.55
Schematic of the foil setup. The CH foil is attached to the massive Mylar washer. After the drive begins, it bows (dashed contour) because the drive pressure is applied only to its central part.

Figure 79.56 describes this effect quantitatively for one of the shots, using six target images of different time frames at 1.6, 1.9, 2.0, 2.2, 2.4, and 2.5 ns. It was assumed (for simplicity) that the main effect of the bowing was a magnification of late-time images with respect to early-time images. If so, the correlation of the magnified early-time image with late-time image should be higher than the correlation of the unmagnified images. (The bowing analysis was performed using raw, unfiltered target images because Wiener-filtered images were all processed with a fixed box size, not allowing this box size to vary, which is necessary to perform bowing analysis.) The dotted line in Fig. 79.56 shows the cross-correlation coefficient of the image at 2.2 ns with the image at 2.5 ns as the function of the magnification of the 2.2-ns image. The cross-correlation coefficient is maximized when the 2.2 ns image is magnified 1.04 times. To maximize the correlation of the same 2.2-ns image with the early-time image at 1.6 ns, it must be demagnified 0.97 times as shown by a dashed line in Fig. 79.56. The thick solid line shows the cross-correlation

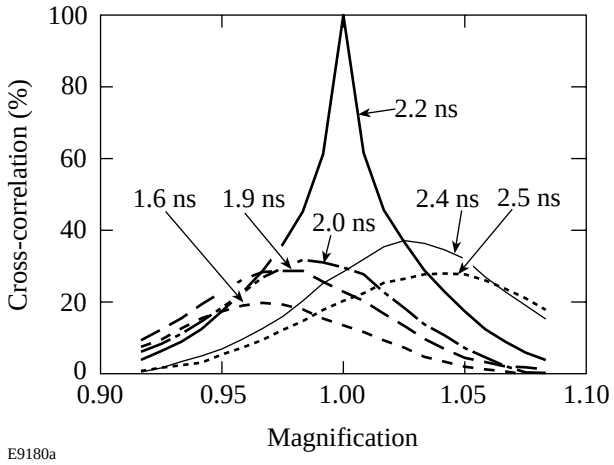

Figure 79.56
"Bowing" of the target. The cross-correlation of the image at 2.2 ns with the images at 2.5 ns, at 2.4 ns, itself, at 2.0 ns, at 1.9 ns, and at 1.6 ns as a function of the magnification of the 2.2-ns image. The smoothing techniques for this shot included DPP's, SSD, and DPR's.

coefficient of the image at 2.2 ns with itself. The shorter the time interval between images, the less magnification (or demagnification) is required for one of the images to be maximally correlated to the features in the other images. This analysis shows that as time progresses, the target images become magnified by about 7% to 10% between the 1.6-ns and 2.5-ns images. This effect is small enough to have minimal effect on the perturbation evolution. For example, Fig. 79.56 shows that all features of the 2.4-ns image are magnified by ~2.5% with respect to the earlier image at 2.2 ns. Figure 79.48(b) shows the spectral evolution for the same shot. The spectrum is peaked at ~34 mm^{-1} for the image at 2.2 ns, and the peak is shifted to ~20 mm^{-1} for the image at 2.4 ns. This ~40% change in the wavelength of the spectral peak has only a ~2.5% contribution from the bowing effect.

Finite Target Thickness Effect

The growth rates for 60-μm and 30-μm preimposed modulations, measured from 1.6 to 2.5 ns, are smaller by a factor of 2 to 2.5 than those measured for earlier times (from 0 to 1.2 ns) by Knauer[5] in similar experiments. These experiments used a larger initial amplitude of preimposed modulations (a_0 = 0.5 μm) and were driven with full smoothing techniques employed. This effect can be attributed to the perforation of the target by short-wavelength perturbations.

The short-wavelength perturbations imprinted by the laser beams are too small to be resolved in the experiments described in this article. Yet, they are estimated to evolve at late times to a σ_{rms} amplitude that equals about three to four (compressed and ablated) thicknesses of the target. If some bubbles penetrate the target, the mass available to feed the growth of the longer-wavelength preimposed modulations by lateral flow is limited; therefore, the growth of these modes is reduced.[15]

This effect has been studied numerically using calculations on the hydrocode *LEEOR2D*.[18] These simulations were conducted for conditions corresponding to the experiment with 20-μm-thick targets irradiated with five overlapped laser beams having various smoothing techniques and with various pulse shapes. One of the pulse shapes used was, as in the experiments, a 3-ns square with an exponential rise of 100 ps per decade and a peak intensity of 2×10^{14} W/cm^2.

Two levels of laser nonuniformity were simulated. The first, using DPP smoothed beams, had the same 1-D nonuniformity's power per mode as experimentally measured using 2-D time-integrated photographs of laser beams.[9] The second was of beams smoothed by DPP's, SSD and DPR's. The smoothing time of the SSD was 25 ps, approximately the effective smoothing time for the pulse used here.[34] Simulations using smooth laser beams were also performed.

2-D calculations of the perturbation evolution with an initial broadband spectrum of laser nonuniformities with and without preimposed 60- and 30-μm-wavelength, single-mode perturbations with initial amplitudes of 0.05 μm have been performed. For each case, the 2-D calculation with the preimposed modulation represents the direction of the preimposed modulation in the 3-D experiment, and the calculation without the preimposed modulation represents the perpendicular direction. The calculated amplitude of the preimposed mode was defined as the Fourier component of that mode in the latter calculation subtracted from that in the former calculation.

Even though the drive and smoothing conditions used in the simulations were similar to those used in the experiments described above, the comparison between the results of the 2-D simulations and the 3-D experiments must be considered only qualitatively because both the initial perturbations and the RT evolution are similar but not identical in 2-D and 3-D. Figure 79.57 shows the calculated evolution of the amplitude of the target areal density (normalized to the initial target density) of the preimposed 60- [Fig. 79.57(a)] and 30-μm-wavelength [Fig. 79.57(b)] modes for the three levels of laser nonuniformity described above. The amplitude of the preimposed modulations grows similarly for all cases until ~1.5 ns. After 1.5 ns, the amplitude of the preimposed mode continues to grow in the case of the smooth drive but is reduced

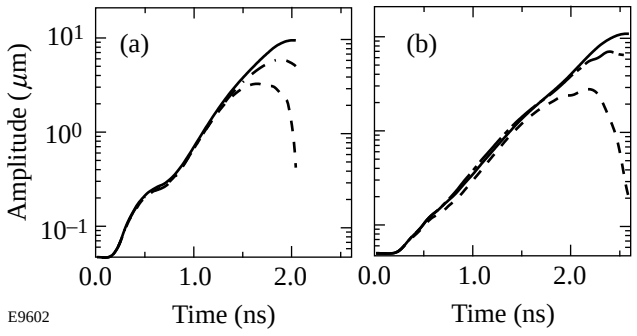

Figure 79.57
The evolution of the amplitude of the target areal density (normalized to the initial density) of preimposed (a) 30-μm- and (b) 60-μm-wavelength modes with smooth laser beams (solid), with DPP's, DPR's, and SSD (dash-dot), and with DPP's only (dashed) calculated using 2-D hydrodynamic simulations.

in the cases of the perturbed drives. This reduction is greater and starts earlier for the case of DPP only, without SSD and DPR's. This behavior is attributed to the perforation of the foil by the short-wavelength modes introduced by the laser nonuniformities.

This evolution can also be seen in Fig. 79.58, where the logarithmic growth rate of the areal-density perturbations of the preimposed modes $\left[\gamma = (\mathrm{d}a/\mathrm{d}t)/a\right]$ is plotted versus time. The growth rate decreases for both 60- [Fig. 79.58(a)] and 30-μm [(Fig. 79.58(b)] wavelengths of the preimposed mode due to the presence of the broadband spectrum of perturbations introduced by the laser nonuniformities.

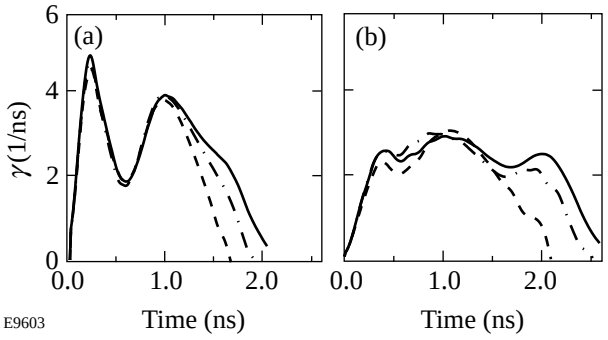

Figure 79.58
The evolution of the logarithmic growth rate $\left[\gamma = (\mathrm{d}a/\mathrm{d}t)/a\right]$ of the areal-density perturbations of (a) 30-μm and (b) 60-μm preimposed modes with smooth laser beams (solid), with DPP's, DPR's, and SSD (dash-dot), and with DPP's only (dashed).

The perforation of the target is most clearly seen in the density maps of the target, shown in Fig. 79.59 for the various 30-μm-wavelength calculations. It can be seen that the short-wavelength perturbations in the target perforate it at $t = 1.4$ ns for the case of DPP [Fig. 79.59(b)] and at $t = 1.6$ ns for the case of DPP's, SSD, and DPR's [Fig. 79.59(f)]. In the case of the uniform drive, the target is not yet perforated at these times, as can be seen in Fig. 79.60. When looking at later times, however, the perforation can clearly be seen to occur between $t = 1.8$ ns and $t = 2$ ns (Fig. 79.60).

One can clearly see the correlation between the times of perforation of the target in these density maps and the saturation in the growth of the preimposed modes, seen in Figs. 79.57 and 79.58. This correlation strengthens the explanation suggested above, that the growth of the preimposed modes is reduced when the broadband perturbations introduced by the laser nonuniformities perforate the target. The reason this reduction has not been measured in other experiments[5] is that the initial amplitude of the imposed perturbation in these experiments was larger; therefore, all measurements were performed at earlier times, when the imprinted perturbations had not yet evolved to large enough amplitudes and therefore the target was still not perforated.

To confirm that the saturation level and the late-time spectra do not depend on the target thickness, Fig. 79.61 shows the results of an additional experiment using a laser drive with DPP's only for 40-μm foil thickness. The measured spectra are shown for a 40-μm CH foil at 2.7 for one shot, and at 2.7 and 2.8 ns for the other shot. The saturation level was again calculated using the spectrally weighed attenuation length λ_x (which does not change significantly going from 20- to 40-μm foils) and the predicted compression (about 2 at ~2 to 3 ns). It can be seen that the finite target thickness does not affect the saturation level since the shapes of measured spectra are similar for both 20- and 40-μm target thicknesses, which is also in agreement with Haan's model. Note that the resulting

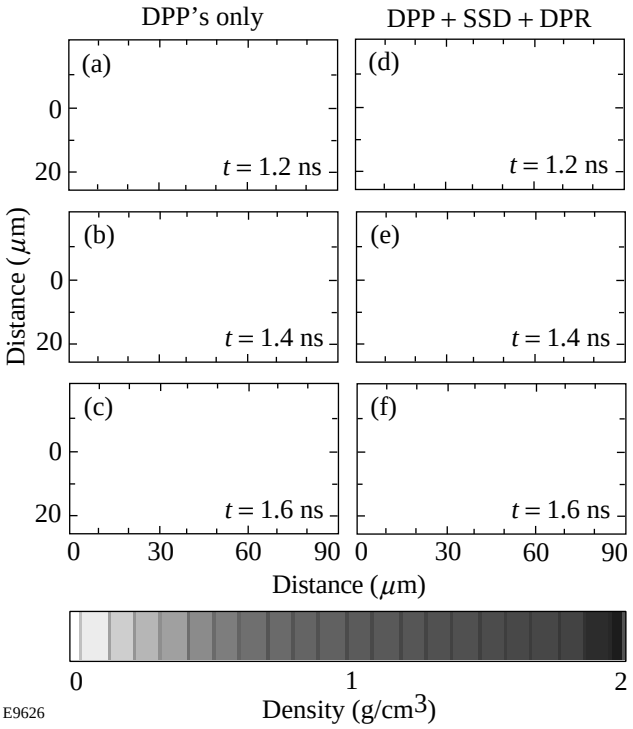

Figure 79.59
Density color maps of the target from the calculation with preimposed 30-μm mode driven by laser beams having DPP's only at (a) $t = 1.2$ ns, (b) $t = 1.4$ ns, (c) $t = 1.6$ ns, and by laser beams having DPP's, SSD, and DPR's at (d) $t = 1.2$ ns, (e) $t = 1.4$ ns, and (f) $t = 1.6$ ns.

acceleration of the 40-μm-thick foils was about a factor of 2 lower and the shock breakout time a factor of 2 later compared to 20-μm foils. The measured noise level is also about twice as high since approximately four-times-fewer photons are transmitted through the 40-μm foil. As a result, the imprint was detected only near the end of the drive and with DPP-only drive. When additional smoothing by SSD and DPR's were added, the initial imprinted amplitudes of target nonuniformity were small enough that, even at the end of the drive, no signal was measured above the noise.

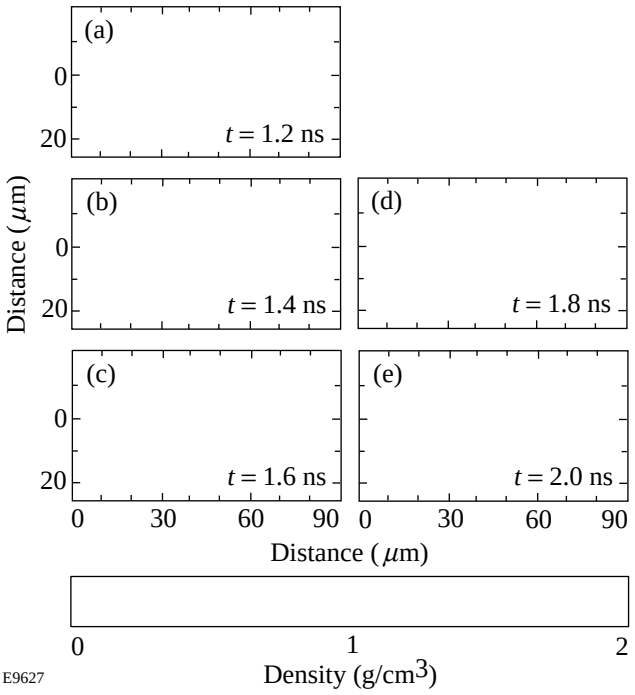

Figure 79.60
Density color maps of the target from the calculation with preimposed 30-μm mode driven by uniform laser beams at (a) t = 1.2 ns, (b) t = 1.4 ns, (c) t = 1.6 ns, (d) t = 1.8 ns, and (e) t = 2.0 ns.

Summary

This article has presented the measured evolution of 3-D broadband perturbations produced by laser imprinting in CH foils, accelerated by UV light. Using through-foil radiography these features were observed to saturate at levels in agreement with those predicted by Haan's model.[4] This behavior was noted in both the shape of the spatial Fourier spectra and in the temporal behavior of modes at various wavelengths. In addition, we noted that the growth of perturbations from broadband spectrum in the linear regime was the same as that for the linear growth of preimposed 2-D perturbations, also in agreement with the Haan model. These experiments were designed to test predicted saturation levels that are used in target designs for ICF experiments. We believe this is a clear experimental demonstration that the Haan model correctly predicts the saturation levels, spectral shape, and temporal evolution of broadband perturbations that are RT unstable. The contributions of measurement error and the effects of finite target thickness and target bowing have been shown to have little effect on our conclusions.

ACKNOWLEDGMENT

This work was supported by the U.S. Department of Energy Office of Inertial Confinement Fusion under Cooperative Agreement No. DE-FC03-92SF19460, the University of Rochester, and the New York State Energy Research and Development Authority. The support of DOE does not constitute an endorsement by DOE of the views expressed in this article.

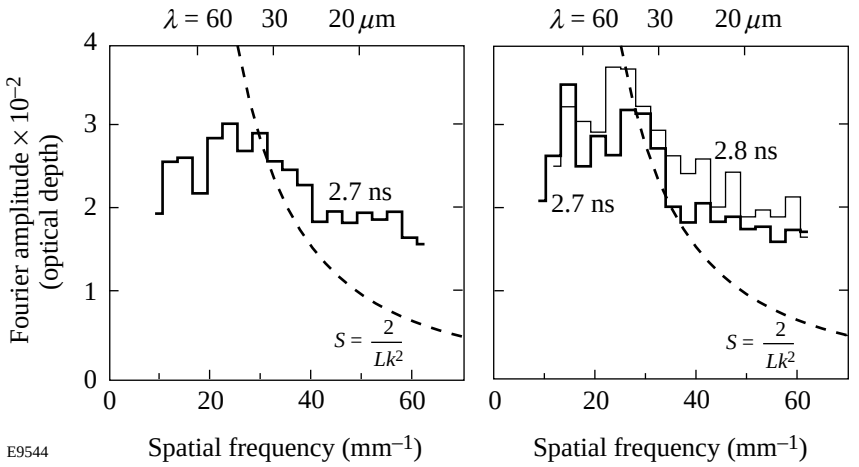

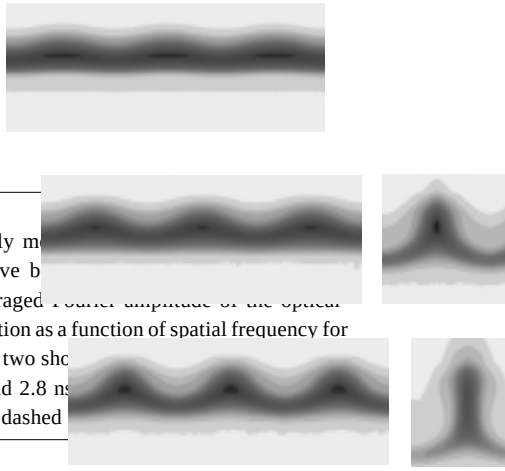

Figure 79.61
Experimentally m
DPP-only drive b
muthally averaged
depth modulation as a function of spatial frequency for
(a) one of the two sho
shot at 2.7 and 2.8 n
shown by the dashed

REFERENCES

1. D. K. Bradley, J. A. Delettrez, R. Epstein, R. P. J. Town, C. P. Verdon, B. Yaakobi, S. Regan, F. J. Marshall, T. R. Boehly, J. P. Knauer, D. D. Meyerhofer, V. A. Smalyuk, W. Seka, D. A. Haynes, Jr., M. Gunderson, G. Junkel, C. F. Hooper, Jr., P. M. Bell, T. J. Ognibene, and R. A. Lerche, Phys. Plasmas **5**, 1870 (1998).

2. S. E. Bodner, D. G. Colombant, J. H. Gardner, R. H. Lehmberg, S. P. Obenschain, L. Phillips, A. J. Schmitt, J. D. Sethian, R. L. McCrory, W. Seka, C. P. Verdon, J. P. Knauer, B. B. Afeyan, and H. T. Powell, Phys. Plasmas **5**, 1901 (1998).

3. S. V. Weber, S. G. Glendinning, D. H. Kalantar, M. H. Key, B. A. Remington, J. E. Rothenberg, E. Wolfrum, C. P. Verdon, and J. P. Knauer, Phys. Plasmas **4**, 1978 (1997).

4. S. W. Haan, Phys. Rev. A **39**, 5812 (1989).

5. J. P. Knauer, C. P. Verdon, D. D. Meyerhofer, T. R. Boehly, D. K. Bradley, V. A. Smalyuk, D. Ofer, P. W. McKenty, S. G. Glendinning, D. H. Kalantar, R. G. Watt, P. L. Gobby, O. Willi, and R. J. Taylor, in *Laser Interaction and Related Plasma Phenomena*, edited by G. H. Miley and E. M. Campbell (American Institute of Physics, New York, 1997), Vol. 406, pp. 284–293.

6. S. G. Glendinning, S. N. Dixit, B. A. Hammel, D. H. Kalantar, M. H. Key, J. D. Kilkenny, J. P. Knauer, D. M. Pennington, B. A. Remington, R. J. Wallace, and S. V. Weber, Phys. Rev. Lett. **78**, 3318 (1997).

7. K. Shigemori *et al.*, Phys. Rev. Lett. **78**, 250 (1997).

8. J. P. Knauer, R. Betti, D. K. Bradley, T. R. Boehly, T. J. B. Collins, V. N. Goncharov, P. W. McKenty, D. D. Meyerhofer, V. A. Smalyuk, C. P. Verdon, S. G. Glendinning, D. H. Kalantar, and R. G. Watt, "Single-Mode Rayleigh-Taylor Growth-Rate Measurements with the OMEGA Laser System," to be published in Physics of Plasmas.

9. T. R. Boehly, V. A. Smalyuk, D. D. Meyerhofer, J. P. Knauer, D. K. Bradley, C. P. Verdon, and D. Kalantar, in *Laser Interaction and Related Plasma Phenomena*, edited by G. H. Miley and E. M. Campbell (American Institute of Physics, New York, 1997), Vol. 406, pp. 122–129.

10. T. R. Boehly, V. A. Smalyuk, D. D. Meyerhofer, J. P. Knauer, D. K. Bradley, R. S. Craxton, M. J. Guardalben, S. Skupsky, and T. J. Kessler, J. Appl. Phys. **85**, 3444 (1999).

11. B. A. Remington *et al.*, Phys. Fluids B **5**, 2589 (1993).

12. R. J. Taylor *et al.*, Phys. Rev. Lett. **76**, 1643 (1996).

13. C. J. Pawley *et al.*, Phys. Plasmas **4**, 1969 (1997).

14. S. W. Haan, Phys. Fluids B **3**, 2349 (1991).

15. M. J. Dunning and S. W. Haan, Phys. Plasmas **2**, 1669 (1995).

16. J. P. Dahlburg *et al.*, Phys. Plasmas **2**, 2453 (1995).

17. D. Shvarts, U. Alon, D. Ofer, R. L. McCrory, and C. P. Verdon, Phys. Plasmas **2**, 2465 (1995).

18. D. Ofer, U. Alon, D. Shvarts, R. L. McCrory, and C. P. Verdon, Phys. Plasmas **3**, 3073 (1996).

19. M. M. Marinak *et al.*, Phys. Rev. Lett. **75**, 3677 (1995).

20. M. M. Marinak *et al.*, Phys. Rev. Lett. **80**, 4426 (1998).

21. V. A. Smalyuk, T. R. Boehly, D. K. Bradley, V. N. Goncharov, J. A. Delettrez, J. P. Knauer, D. D. Meyerhofer, D. Oron, and D. Shvarts, Phys. Rev. Lett. **81**, 5342 (1998).

22. T. R. Boehly, D. L. Brown, R. S. Craxton, R. L. Keck, J. P. Knauer, J. H. Kelly, T. J. Kessler, S. A. Kumpan, S. J. Loucks, S. A. Letzring, F. J. Marshall, R. L. McCrory, S. F. B. Morse, W. Seka, J. M. Soures, and C. P. Verdon, Opt. Commun. **133**, 495 (1997).

23. Y. Lin, T. J. Kessler, and G. N. Lawrence, Opt. Lett. **20**, 764 (1995).

24. S. Skupsky, R. W. Short, T. Kessler, R. S. Craxton, S. Letzring, and J. M. Soures, J. Appl. Phys. **66**, 3456 (1989).

25. S. G. Glendinning *et al.*, in *Applications of Laser Plasma Radiation II*, edited by M. C. Richardson and G. A. Kyrala (SPIE, Bellingham, WA, 1995), Vol. 2523, pp. 29–39.

26. V. A. Smalyuk, T. R. Boehly, D. K. Bradley, J. P. Knauer, and D. D. Meyerhofer, Rev. Sci. Instrum. **70**, 647 (1999).

27. T. Endo *et al.*, Phys. Rev. Lett. **74**, 3608 (1995).

28. R. Ishizaki and K. Nishihara, Phys. Rev. Lett. **78**, 1920 (1997).

29. B. A. Remington *et al.*, Phys. Fluids B **4**, 967 (1992).

30. M. C. Richardson, P. W. McKenty, F. J. Marshall, C. P. Verdon, J. M. Soures, R. L. McCrory, O. Barnouin, R. S. Craxton, J. Delettrez, R. J. Hutchison, P. A. Jaanimagi, R. Keck, T. Kessler, H. Kim, S. A. Letzring, D. M. Roback, W. Seka, S. Skupsky, B. Yaakobi, S. M. Lane, and S. Prussin, in *Laser Interaction and Related Plasma Phenomena*, edited by H. Hora and G. H. Miley (Plenum Press, New York, 1986), Vol. 7, pp. 421–448.

31. R. Betti, V. N. Goncharov, R. L. McCrory, and C. P. Verdon, Phys. Plasmas **5**, 1446 (1998).

32. H. Takabe, L. Montierth, and R. L. Morse, Phys. Fluids **26**, 2299 (1983).

33. H. Takabe *et al.*, Phys. Fluids **28**, 3676 (1985).

34. S. Skupsky, LLE, private communication (1998).

Uniaxial/Biaxial Stress Paradox in Optical-Materials Hardening

Owing to its excellent homogeneity and low-intrinsic absorption properties, fused silica remains the preferred material for high-power laser applications over a wide wavelength range, but especially in the UV. In particular, large-aperture glass and excimer lasers, such as Nova, Beamlet, OMEGA, NIKE, and, in the foreseeable future, the National Ignition Facility (NIF), the Megajoule laser (LMJ, France), and others, owe their existence to readily available, large-diameter fused silica finding use in the form of beam-transport lenses and windows. Often these lenses and windows separate atmospheric pressure from vacuum areas, such as on spatial filters and target tanks, experiencing not only high-fluence irradiation conditions but also pressure-differential–induced stresses. The combination of the two presents an interesting challenge in terms of laser damage, as the formation of pits and cracks during conventional damage may get aggravated by the presence of stress and lead to dramatic device failure by fragmentation and acceleration of the lens or window shards into the evacuated space.

Even in the absence of a vacuum issue with its concomitant stress, laser damage to fused silica under periodic illumination by UV light, such as found in UV-lithography or medical-instrument applications, limits system performance and increases maintenance costs. This motivates the search for simple methods to alleviate the onset of or, at least, the detrimental consequences of laser damage. In earlier work,[1–4] dynamic aspects of laser-induced crack formation in fused silica and its correlation with stress, both self-induced[2] and externally applied,[3,4] have been studied by us with an eye toward preparing the foundation for such remedies. In the current work, we try to answer several important questions raised by this prior work.

In brief, a laser-initiated crack has been shown to grow upon repeated irradiation by either IR[5] or UV[1,5] laser pulses, causing a *hoop stress*[2] to form in its immediate surroundings, the existence of which is essential for further growth. This causal relation was tested by breaking the *hoop-stress symmetry* with the help of an external stress field and thereby arresting further crack propagation, even at pump fluences much larger than those necessary for starting the crack initially. This was demonstrated for fused silica initiated at either the substrate exit or entrance surface. Surfaces, with few exceptions, suffer from lower laser-damage thresholds than bulk—a fact attributable to the consequences of the requisite, but extremely intrusive, acts of cutting, grinding, polishing, and cleaning the surfaces. Cleaved surfaces that are spared these procedures offer comparably higher damage thresholds.[6] The surfaces of fused silica are of special interest in that a *near-surface layer* of material *densification*[7] is surmised to be formed during polishing, which, by itself, may prompt *near-surface residual-stress fields* to develop. One key question arising from the prior work[3,4] thus became whether or not, in the absence of a densification layer and its residual-stress field, the effects observed in fused silica will remain. Or, put another way, will externally applied stresses also delay laser-damage initiation in cleaved silica bulk and/or in materials for which no such densification layer exists? To find the answer, this work addresses, in addition to polished fused silica, alternate model systems: cleaved silica bulk and BK-7, borosilicate glass.

A second question arises from the earlier *observed increase in surface-damage initiation threshold* and *crack growth arrest* with external stresses applied in the laser-beam direction. The question is whether or not the direction of the applied load has an effect on the surface-damage initiation threshold and crack growth. To answer this question, different applied load configurations are considered in this work; among them are the uniaxial compressions in the x or z direction, the biaxial compression in the x and z directions for rectangular samples (fused silica and BK-7), as well as radially applied pressure for round fused-silica samples.

Sample irradiation was carried out by the fundamental and frequency-tripled outputs of a Nd:glass oscillator/single-pass amplifier system. This system produced a beam of nearly Gaussian profile after passage through a vacuum spatial filter, prior to any frequency conversion. The beam was then focused by a 2-m-focal-length fused-silica lens to a ~600-μm spot size

at the sample entrance surface. Laser pulses, produced at a repetition rate of one pulse every 10 s, had nominal pulse duration of 1 ns at 1053 nm and 500 ps at 351 nm.

A PDP-II computer and CAMAC [computer-aided measurement and control (J. White Co. 800)] crate system were used for data acquisition and experiment control. The system included a charge-injection-device (CID) camera located in a sample-equivalent plane for recording the fluence distribution in the beam spot.

The beam-incident direction was chosen to be ≤10° off-normal to the sample entrance face to prevent any back-reflection of residual, unconverted IR from seeding the amplifier in the backward direction, and setting up a 351-nm Fresnel interference pattern between the sample entrance and exit surfaces that would invalidate the calculated fluence distribution.

In this work, *damage* is defined to be any visible permanent modification to the surface of the glass material, observable with a 110×-magnification, dark-field microscope. The smallest damage spots observed as faint scatter sites were approximately 0.5 to 1 μm in diameter. Due to the thickness of the samples, spatial and temporal distortions of the beam were avoided; therefore, both front- and exit-surface damages were considered. Damage thresholds were determined by averaging between the highest laser fluence incident on the sample that produced no damage and the lowest laser fluence that did produce damage.

The samples studied in this work were rectangular, 64 × 13.6×4.3-mm and circular, 50-mm-diam, fused-silica samples of Corning 7940 UV, grade A. They were conventionally pitch polished to *laser quality* (rms ≤ 10 Å) on the entrance and exit surfaces and to *cosmetic quality* around the edges to monitor *in situ* the crack propagation, as were the BK-7 samples, which were also commercial blocks (52 × 11.5 × 5 mm).

Samples were mechanically loaded by clamping each between aluminum plates separately attached to a load cell (Eaton, Model 3397-25, max. load capacity: 25 lbs). A predetermined, constant uniaxial, compressive load was applied in each geometrical configuration. Details of the experimental setup of the applied load used in the laser-beam direction can be found in Ref. 8.

Laser-damage thresholds (for pulse lengths greater than picoseconds) are always reported as *average values* derived from a statistical number of sample sites *per tested specimen*. In all *nondeterministic*, i.e., extrinsic-impurity-driven laser-damage processes, the damage occurrence hinges on the statistical presence or absence of one or more absorbing impurities within a given irradiated area. This statistical distribution in defect volume density is now convoluted by a site-to-site–varying stress distribution. In an ideal experiment, a large enough number of tests on samples and sites with precisely known local stress will deconvolve the two distributions. In practice, however, this is unrealistic. Rather, simulation of local stress conditions by finite-element methods permits one to find with acceptable accuracy, for various loading-geometry-boundary conditions, the stresses within the aperture, based on which one may choose many irradiation sites on a single sample. A three-dimensional, finite-element analysis code ANSYS 5.4A®, developed by ANSYS Inc., was used to determine the stress distribution within loaded samples.

Figure 79.62 shows the 500-ps/351-nm damage-onset fluence threshold for fused-silica exit and entrance surfaces versus the stress σ_{zz} resulting from a compressive load in the laser-beam direction. The question to address is whether or not a link exists between the silica surface–densification layer (and its residual-stress distribution) and the damage-threshold

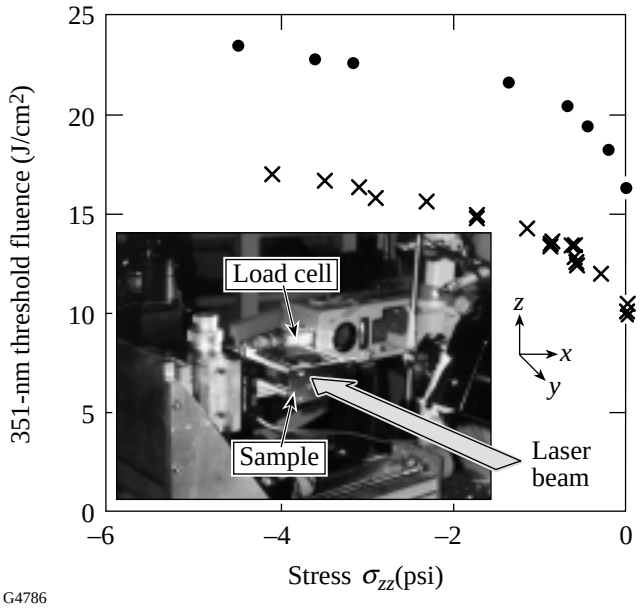

Figure 79.62
Entrance (•)- and exit (×)-surface, 351-nm damage-initiation thresholds as functions of applied stress in fused silica for the laser beam direction–loading configuration.

trend. Applying external stresses will bias these effects. In light of Fig. 79.62, it appears plausible that increasing stresses within the sample are decreasing the effect of the densified layer and, at the same time, are increasing the damage-onset threshold. To confirm or rule out this premise, further tests were needed on cleaved silica bulk and on a material that does not densify when polished. Figure 79.63 displays the exit-surface-damage-threshold results versus applied stress obtained for BK-7 with 1-ns, 1053-nm pulses. A data point from Ref. 9, obtained at 1 ns, 1064 nm (also represented in Fig. 79.63), shows good agreement with our *stress-free* measurements. Furthermore, Fig. 79.64 illustrates the front-surface-damage thresholds against the externally applied stresses obtained for cleaved bulk silica. From Figs. 79.63 and 79.64, it becomes clear that a damage-initiation-threshold enhancement in response to externally applied stress is also obtained for borosilicate glass as well as for cleaved bulk silica, ruling out causal relations between densification, applied stress, and damage-initiation-threshold enhancement in all systems considered here.

Next, we address correlations between (1) the external stress and the laser-beam polarization and/or (2) the external stress and thermal stress. In other words, (1) What is the effect of external stress on the damage threshold and crack growth for a certain beam polarization? and (2) What is the magnitude of transient, thermal stresses induced by laser heating of the material compared to the magnitude of the externally applied stresses?

The answer to the second question was obtained by using ANSYS in a thermal, transient analysis. A metallic defect (Hf) of size $200 \times 200 \times 100$ Å embedded in the fused-silica matrix was considered and assumed to have reached a temperature of 20,000 K by the end of the laser pulse (1 ns). Details of the transient thermal finite-element analysis can be found in Ref. 10. The thermal stresses deduced from ANSYS {$\sim \alpha E \Delta T$, where α is the thermal expansion coefficient, E the Young's modulus, and ΔT the temperature [relative to the strain-free temperature (room temperature)] of a given point in the matrix} were found to be two orders of magnitude larger than the applied mechanical stresses, rendering them all but irrelevant.

The issue of mechanical stress versus beam polarization was addressed by using the original loading setup in two different geometrical loading configurations; the load was first applied in the x direction (Fig. 79.65), and second in the z direction (Fig. 79.66). For these two configurations, the result-

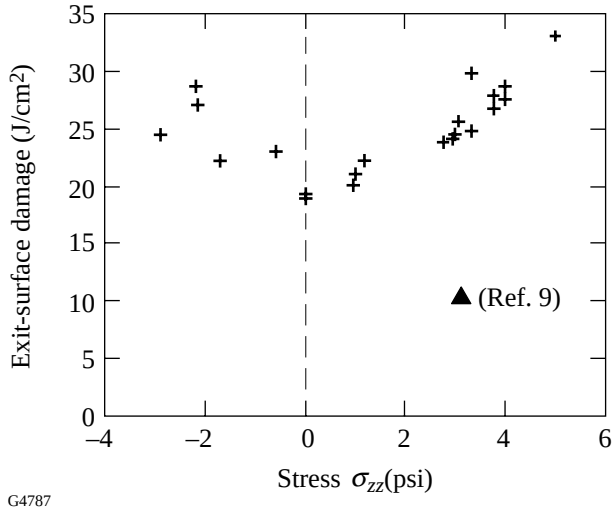

Figure 79.63
Exit-surface, 1053-nm damage-initiation threshold as a function of externally applied stresses obtained with borosilicate glass (BK-7) for the same loading configuration as Fig. 79.62. For comparison a data point (triangle) obtained at 1064 nm, 1 ns from Ref. 9 is reported.

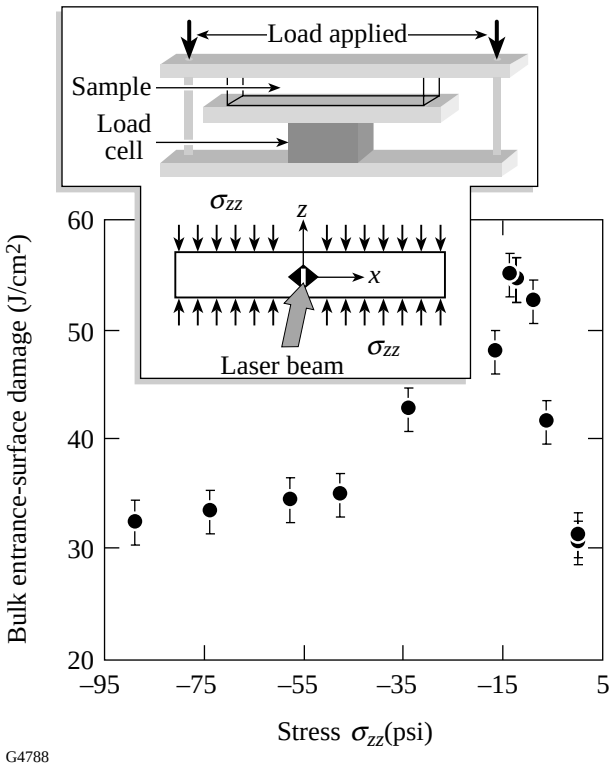

Figure 79.64
Entrance-surface, 351-nm, 500-ps, damage-initiation threshold as functions of applied pressure in the z direction (perpendicular to the laser beam) in cleaved silica bulk.

ing stress estimated from ANSYS is uniaxial along the *x* axis or the *z* axis, respectively. For uniaxial stress, Figs. 79.65 and 79.66 show the damage threshold to reach a maximum around –5 psi and to drop to its initial, stress-free value for loads larger than –15 psi. The same behavior was obtained with BK-7 loaded in the *z* direction (Fig. 79.66), ruling out any relationship between the stress-onset damage threshold and the laser-beam polarization.

To investigate the effect of the loading geometry on the damage threshold, a setup was designed that provided simultaneous stresses in both the *x* and *z* directions. Figure 79.67 shows the results obtained with this configuration for both entrance and exit surfaces of fused silica. The damage threshold reaches a maximum around $\sigma_{zz} = \sigma_{xx} = -5$ psi and stays constant thereafter, a behavior similar to that found for the configuration in Fig. 79.62, where the ANSYS-derived stress distribution shows stresses in both the *x* and *z* directions, although $\sigma_{zz} > \sigma_{xx}$. On the other hand, experiments carried out on circular fused-silica samples are illustrated in Fig. 79.68. Although the current setup did not permit pressures larger than 4.2 psi to be applied, Fig. 79.68 hints that the maximum threshold would be reached also around 4 to 5 psi.

Key results from Fig. 79.62 and Figs. 79.65–79.68 are: (1) Independently of the loading geometry used, the maximum threshold for fused silica is obtained around an applied stress of –5 psi. (2) A geometrical loading approximating practical situations is that of Fig. 79.62, where a plateau is reached (the configuration used in Fig. 79.67 is very difficult to implement in practice).

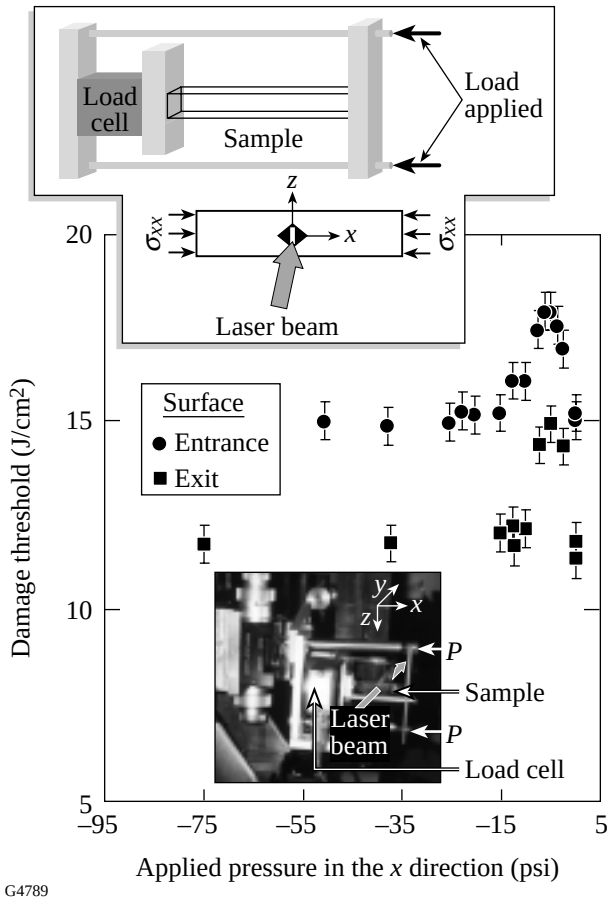

Figure 79.65
Entrance- and exit-surface, 351-nm, 500-ps damage-initiation thresholds as functions of applied pressure in the *x* direction (perpendicular to the laser beam) in polished fused silica. The load *P* is applied via two screws.

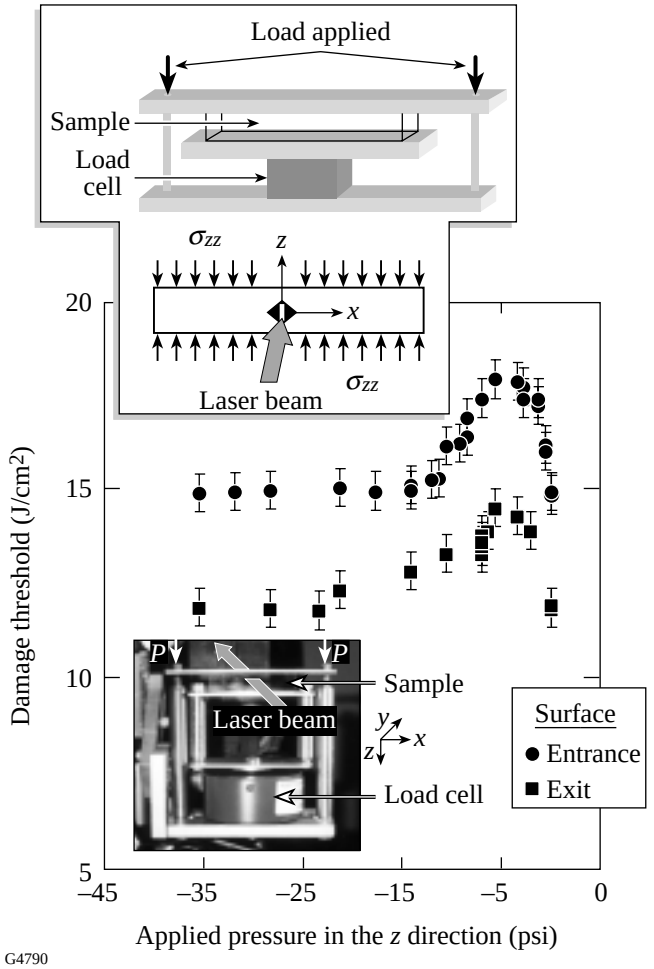

Figure 79.66
Entrance- and exit-surface, 351-nm, 500-ps damage-initiation thresholds as functions of applied pressure in the *z* direction (perpendicular to the laser beam) in polished fused silica. The load *P* is applied via two screws.

Experiments on crack growth using *uniaxial* stress configurations were also carried out, but *no crack arrest* was observed for any of these configurations, leading one to conclude again that the optimum result for both damage-threshold enhancement and crack-growth arrest in fused silica can be obtained only in a biaxial stress configuration.

In conclusion, this work presents experimental results on stress-inhibited, laser-driven crack growth and stress-delayed, laser-damage-initiation thresholds in fused silica and borosilicate glass (BK-7). The use of different loading geometries providing uniaxial and biaxial stresses shows that the *biaxial* stress configuration offers superior efficiency in raising the laser-damage-initiation threshold by up to 78% and arresting crack growth down to 30% relative to stress-free conditions. The results also raise the intriguing paradox of biaxial symmetry breaking proving superior to uniaxial effects—a paradox that calls for further tests.

ACKNOWLEDGMENT

This work was supported by the U.S. Department of Energy Office of Inertial Confinement Fusion under Cooperative Agreement No. DE-FC03-92SF19460, the University of Rochester, and the New York State Energy Research and Development Authority. The support of DOE does not constitute an endorsement by DOE of the views expressed in this article.

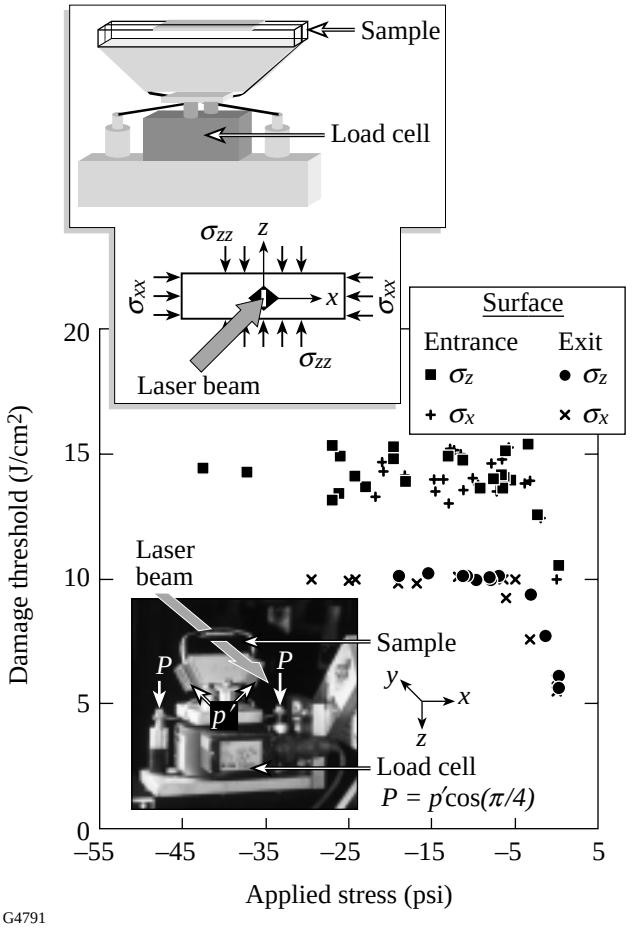

Figure 79.67
Entrance- and exit-surface, 351-nm, 500-ps damage-initiation thresholds as functions of applied stresses in polished fused silica for the case of a compression load in the *x*-*z* plane.

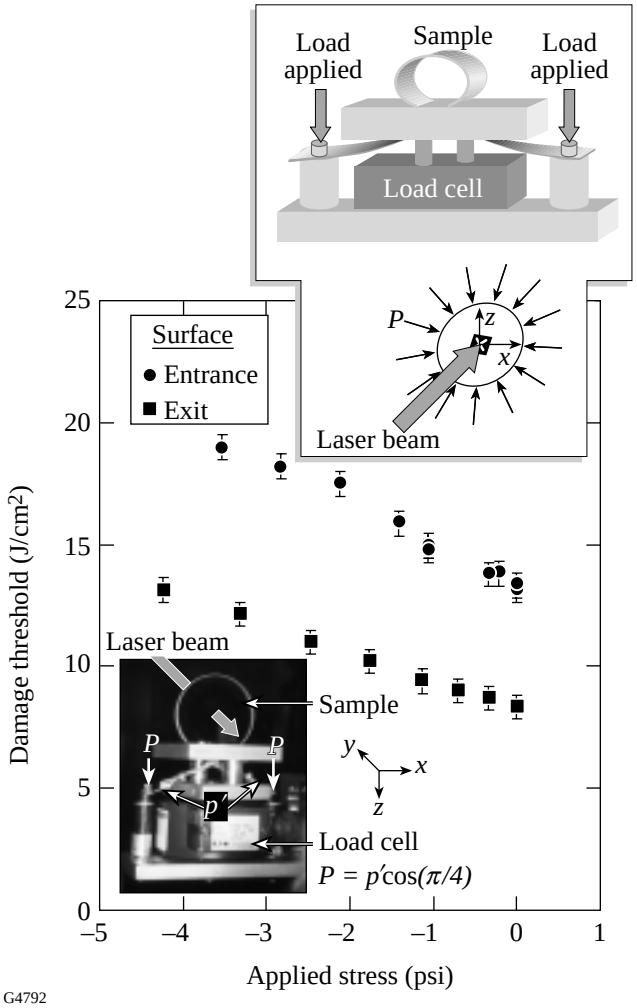

Figure 79.68
Entrance- and exit-surface, 351-nm, 500-ps damage-initiation thresholds as functions of applied pressure in round, polished-fused-silica samples.

REFERENCES

1. F. Dahmani, J. C. Lambropoulos, A. W. Schmid, S. Papernov, and S. J. Burns, J. Mater. Res. **14**, 597 (1999).

2. F. Dahmani, A. W. Schmid, J. C. Lambropoulos, and S. Burns, Appl. Opt. **37**, 7772 (1998).

3. F. Dahmani, S. J. Burns, J. C. Lambropoulos, S. Papernov, and A. W. Schmid, Opt. Lett. **24**, 516 (1999).

4. F. Dahmani, J. C. Lambropoulos, A. W. Schmid, S. Papernov, and S. J. Burns, "Crack Arrest and Stress Dependence of Laser-Induced Surface Damage in Fused Silica and Borosilicate Glass," submitted to Applied Optics.

5. A. Salleo, R. Chinsio, and F. Y. Génin, in *Laser-Induced Damage in Optical Materials: 1998*, edited by G. J. Exarhos *et al.* (SPIE, Bellingham, WA, 1998), Vol. 3578, pp. 456–471.

6. S. Papernov, D. Zaksas, J. F. Anzellotti, D. J. Smith, A. W. Schmid, D. R. Collier, and F. A. Carbone, in *Laser-Induced Damage in Optical Materials: 1997*, edited by G. J. Exarhos *et al.* (SPIE, Bellingham, WA, 1998), Vol. 3244, pp. 434–445.

7. H. Yokota *et al.*, Surf. Sci. **16**, 265 (1969).

8. Laboratory for Laser Energetics LLE Review **77**, 26, NTIS document No. DOE/SF/19460-284 (1998). Copies may be obtained from the National Technical Information Service, Springfield, VA 22161.

9. F. Rainer, R. P. Gonzales, and A. J. Morgan, in *Laser-Induced Damage in Optical Materials: 1989*, Natl. Inst. Stand. Technol. (U.S.), Spec. Publ. 801 (U.S. Government Printing Office, Washington, DC, 1990), Vol. 1438, pp. 58–73.

10. S. Papernov and A. W. Schmid, J. Appl. Phys. **82**, 5422 (1997).

Observation of Electron Trapping in an Intense Laser Beam

Since the discovery of the ponderomotive force over 40 years ago, it has been known that charged particles interacting with an oscillating electromagnetic field will seek regions of low intensity.[1] It was immediately proposed that with the appropriate field distribution, particles could be trapped with this force.[2] The case of electron confinement with a specially shaped laser focus has been discussed since then.[3–5] Recently we reported on the optical generation of a three-dimensional, ponderomotive-optical trap with a high-peak-power laser.[6] In this article we present the first evidence of electron trapping in a high-intensity laser field, with confinement of electrons with energies up to 10 keV. To our knowledge, this work represents the first controlled manipulation of electrons in a high-intensity laser field by the modulation of the spatial intensity distribution of the beam. This opens up a new direction of study in high-intensity laser–electron interactions. Here, we present the effects of trapping on linear Thomson scattering. A trapping beam could also be used to enhance the recently observed nonlinear Thomson scattering.[7] While some further experiments may use the particular geometry described in this work, more generally we have shown that near-field phase control of a high-power laser beam can lead to tailored focal regions that may be optimized for a myriad of experiments.

Electrons interact with a laser field via the Lorentz force. For field distributions with a slowly varying temporal and spatial envelope, the motion of the electrons can be decomposed into a high-frequency quiver and a slower, "dark-seeking" drift.[8] The quiver motion is a direct result of the rapidly oscillating electromagnetic field, while the drift is a consequence of the ponderomotive force (the cycle-averaged Lorentz force). The ponderomotive force takes the form $\mathbf{F}_{\text{pond}} = -\nabla U_{\text{pond}}$, where $U_{\text{pond}} = \left(e^2 I\lambda^2\right)/\left(2\pi mc^3\right)$ (I is the intensity, λ is the wavelength, c is the speed of light, and e and m are the electron charge and rest mass, respectively). At low intensities, the quiver velocity is nonrelativistic and the magnetic field term in the Lorentz force can be ignored. The electron motion is a result of the electric field alone and is purely harmonic. Under these conditions, the electron undergoes linear Thomson scattering.[9] For high intensities ($I \sim 10^{18}$ W/cm^2 for λ = 1-μm light), the fully relativistic Lorentz force must be used and the electron quivers anharmonically. In this case, the electron emits harmonics of the incident field (nonlinear Thomson scattering).[7,10,11] To reach such intensities, a short-pulse, high-energy laser beam must be focused to a small spot size. Tight focusing yields high peak intensities but also results in large-intensity gradients and, therefore, large ponderomotive forces. In an ordinary centrally peaked focus, the strongest gradients point radially inward, so the ponderomotive force pushes electrons outward, directly away from the regions of high intensity.

To control the drift of electrons from the focal region, we have developed a scheme to create a focus with a local minimum at its center.[6] A uniphase laser beam, regardless of its amplitude distribution, will focus to a centrally peaked spot due to the constructive interference at the center of the focal region. By inducing a π-phase shift in the central portion of an incident beam, the light from the unshifted outer region will destructively interfere with the shifted light. If half of the incident field is shifted, there will be complete destructive interference at the center of the focus, creating a field null surrounded on all sides by regions of nonzero intensity. This occurs for a π-region diameter of 1.65w for a Gaussian beam, where w is the incident beam's $1/e^2$ (in intensity) radius.[6]

Computer simulations of electron trajectories in a Gaussian focus and a trapping focus have been performed. With the trap, the electrons spend a significantly longer time interacting with the intense field. In one simulation, the electrons were released into the field by barrier-suppression ionization[12] from He^{1+} at an intensity of 1.5×10^{15} W/cm^2 by a laser pulse with the same characteristics as in our laboratory:[13] $I_{\text{peak}} = 10^{18}$ W/cm^2, $w_0 = 5\ \mu$m, $\tau = 2$ ps, $\lambda = 1.05\ \mu$m, where I_{peak} is the peak intensity of the ordinary beam, w_0 is the $1/e^2$ (in intensity) radius of the focal spot, τ is the FWHM pulse width, and λ is the central wavelength. The fully relativistic Lorentz force was used in this and all subsequent simulations. A typical electron released into the trapping region experiences an average intensity approximately three times as high for a time approximately six

times as long as an electron released into a comparable Gaussian focus (generated with the same near-field power distribution). These values depend on the electron's initial location in the focal region. Similar results are obtained with different gas species and charge states. By tuning the trap minimum away from zero (by changing the size of the π region),[6] the peak intensity that the electron experiences can be increased by a factor of 10, while maintaining trapping.

The most direct signature of electron trapping is the enhanced linear Thomson scattering that results from the increased laser–electron interaction. Figure 79.69 shows the results of a computer code used to generate images of Thomson-scattered radiation from three different focal regions. The code uses the same laser pulse as described above and propagates electrons ionized from up to the first eight charge states in argon by barrier-suppression ionization. Since the total, time-integrated Thomson scattering is a linear function of intensity, interaction time, and number of electrons, the total signal at a given point in the focal region was approximated as the sum over all times of the product of electron number, instantaneous laser intensity, and time step. Figure 79.69(a) shows the w_0 = 5-μm Gaussian focal-plane image, Fig. 79.69(b) the focal-plane image generated by a flat-top incident beam (which mimics the extra structure present in the experimental, unaltered focal spot), and Fig. 79.69(c) the focal-plane image generated by passing a flat-top incident beam through an appropriately sized π-phase plate. The value of the intensity walls surrounding the central minimum of the trapping beam is approximately 12% of the nontrapping beam's peak intensity. For the peak intensity achievable with this laser system, this corresponds to a wall intensity of 1.2 $\times 10^{17}$ W/cm^2, which is equal to a ponderomotive barrier of 12 keV. Figure 79.69(d) shows the two-dimensional *x*,*z* projection of the Thomson-scattered light from the Gaussian focus (the laser is polarized along the *x* direction and propagates along the *z* direction), Fig. 79.69(e) shows the predicted signal from the flat-top beam, and Fig. 79.69(f) shows the predicted signal from the trapping flat-top beam. Figure 79.69(g) shows the total predicted Thomson-scattered signal for each beam type as a function of *z*. This corresponds to a transverse integral along *x* for each *z* position. The thin dashed line is the signal from the Gaussian focus, the dot–dashed line is the signal from the nontrapping flat-top focus, and the solid line is the signal from the trapping flat-top focus. The signal from the regular flat-top focus is substantially higher than the signal from the Gaussian focus at $z = 0$. This is due to the weak trapping that occurs in the low-intensity rings that surround the central spot. Even though the rings can capture only low-energy electrons, they represent a large volume and therefore add considerably to the total signal. At $z = 0$, the peak intensity value of the rings is 2% of the peak intensity of the central spot. A central peak intensity of 10^{18} W/cm^2 corresponds to 2-keV electrons being trapped by the rings. In contrast, the trapping

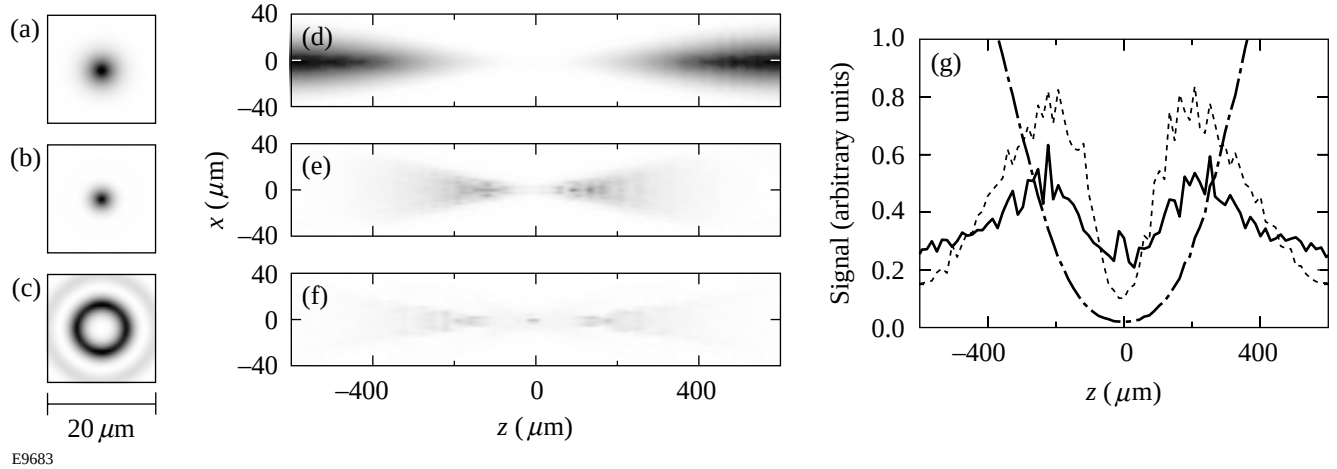

Figure 79.69
Computer simulations of Thomson scattering. (a) Focal-plane image of a Gaussian beam, (b) focal-plane image generated with a flat-top incident beam, (c) focal-plane image of a trapping beam generated with a flat-top incident beam, (d) image of the Thomson-scattered light from a Gaussian focus as viewed orthogonally to the plane of polarization, (e) Thomson-scattered image from the flat-top beam, (f) Thomson-scattered image from the trapping flat-top beam, (g) total Thomson-scattered signal as a function of *z* (laser propagation direction) for the Gaussian beam (thin dashed line), the nontrapping flat-top beam (dot–dashed line), and the trapping flat-top beam (solid line). The increase in signal from the center of the trapping focus is due to the confinement of electrons, while the decrease away from $z = 0$ is due to more-rapid ponderomotive expulsion along the steeper gradients in those portions of the trapping focal region.

focus generated with the phase plate can confine 12-keV electrons at $z = 0$. As expected, the trapping focus has the largest signal in the central focal region. Away from $z = 0$, the signal is lower than in the nontrapping case because of the more strongly peaked beam profiles of the trapping beam in those regions, resulting in more-rapid ponderomotive expulsion.

To generate the trapping focus in the laboratory, a segmented wave-plate arrangement was used to induce the π-phase shift on the laser pulse.[6] A disk and annulus were cut from a half-wave plate, and the disk was rotated by 90° with respect to the annulus. In this position, the *o* axis of the disk coincided with the *e* axis of the annulus and vice versa. Since the operation of a half-wave plate relies on the retardation of a half-wave between the *o* and *e* waves, this simple arrangement adds a π-phase shift to the inner portion of the beam with respect to the outer region. The size of the disk (4-cm diameter) was chosen such that approximately half of the incident field was shifted. The laser beam had an essentially flat-top profile of 6.5-cm diameter, with extra energy at the center and edges of the beam.

The experimental setup for imaging Thomson-scattered radiation from the laser focus is shown in Fig. 79.70. The horizontally polarized (perpendicular to the plane of the figure) laser pulse enters a high-vacuum chamber from the right and is focused by an internally mounted aspherical focusing lens ($f = 20$ cm, $\phi = 12$ cm, with an 8-mm-diam block in the center). The chamber is typically backfilled with 1 to 5 Torr of nitrogen or argon. To generate the trapping beam, the wave-plate pieces are placed directly before the entrance window. The focused beam passes into and out of an aluminum tube (outer diameter of 4.4 cm) through a pair of 1.9-cm holes. The end of the tube is blocked by a solid aluminum cone that serves as a dark background for the height-adjustable 4× microscope objective. Both the tube and the cone were bead blasted and black anodized for maximum absorption of background light. The focal region is transversely imaged onto a CCD camera (CCD1) by the objective and a camera lens (back focal length of 15 mm, open aperture of 10 mm) after passing through an infrared bandpass filter ($T_{max} = 38\%$ at $\lambda = 1055.5$ nm, $\lambda_{FWHM} = 2.5$ nm). The tip of the objective was approximately 8 mm from the laser axis. The total magnification of the imaging system (from the laser focus to the 4.8-mm × 3.6-mm CCD1 array) was 1.0. After passing through the tube, the diverging laser beam is refocused by a second lens (identical to the focusing lens) onto a second CCD camera (CCD2) approximately 6 m away (the convergence angle of the beam is exaggerated in the schematic). CCD2 was used to take typical focal-plane images.

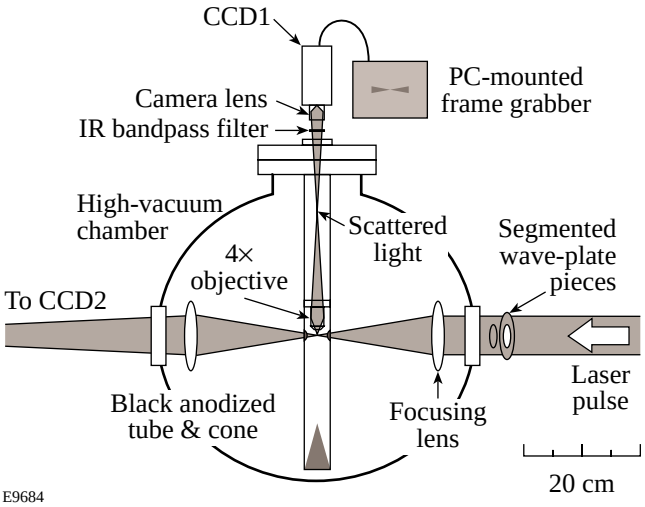

Figure 79.70
Experimental arrangement for imaging Thomson-scattered light from a high-intensity laser focus. The tube and cone serve to reduce the substantial laser light background, and recombination light is eliminated by an infrared bandpass filter. The chamber is typically backfilled with a low density (1 to 5 Torr) of argon or nitrogen.

The experimental results for Thomson-scattered radiation from 2.5 Torr of argon are shown in Fig. 79.71. Figure 79.71(a) shows the nontrapping focal-plane image at CCD2 (which was coupled to a 10× microscope objective for a total magnification of 150 from inside the vacuum chamber to the CCD2 array). Figure 79.71(b) shows the trapping focal-plane image generated with the wave-plate pieces in place. The value of the intensity walls surrounding the central minimum of the trapping beam at $z = 0$ is approximately 15% of the nontrapping beam's peak intensity, and the central minimum is less than 3% of the nontrapping beam's peak intensity. For a nontrapping beam's peak intensity of 10^{18} W/cm^2, this corresponds to a trap depth of 12 keV at $z = 0$. Away from $z = 0$, the trap wall's height falls to approximately 10% of the nontrapping beam's peak intensity, giving a three-dimensional trap depth of approximately 7 keV. The focal-plane images were not noticeably affected for backfill pressures of less than 10 Torr. Figure 79.71(c) shows the image of the Thomson-scattered radiation from the regular beam, and Fig. 79.71(d) the scattered image from the trapping beam. Each image is an average of 30 laser shots. The average laser energy was 500 mJ, which corresponds to a peak intensity of 7×10^{17} W/cm^2 for the nontrapping beam. The shape of the images was independent of gas species (argon or nitrogen) or pressure (1 Torr or 2.5 Torr), and the total signal strength varied linearly with

pressure. Rotating the polarization of the incident beam so it was aligned with the observation direction completely extinguished the signal, as expected for linear Thomson scattering. The total signal as a function of z [as in Fig. 79.69(g)] is shown in Fig. 79.71(e). The signal from the trapping focus is higher at $z = 0$ because of electron confinement and lower away from $z = 0$ because of steeper intensity gradients, in agreement with predictions [see Fig. 79.69(g)]. The asymmetry in the signal about $z = 0$ is due to the asymmetry in the intensity distribution of the laser along the propagation direction.

In addition to increased signal strength, the signal shows the expected enhanced dependence on laser intensity. In a smooth, Gaussian focus, electrons exit the focal region well before the peak of the pulse. For an electron from a given charge state released into the field at a given position, the initial intensity and spatial intensity gradient that it experiences will be the same regardless of peak intensity. As the electron leaves the laser focus, the intensity that it experiences as a function of time will be only slightly modified by the change in its temporal position in the laser pulse envelope. The total signal will, however, increase because of the increasing focal volume with intensity.[14] The effect of the increase in focal volume can be minimized by considering only the signal from the center of the focal region ($-z_0 < z < z_0$, where $z_0 = 75\ \mu$m is the Rayleigh range of a Gaussian beam with $w_0 = 5\ \mu$m). With the trapping focus, electrons interact with the laser pulse for a much longer period of time; therefore, the Thomson-scattered signal will be more sensitive to the peak intensity of the laser.

Figure 79.72(a) shows the experimentally measured, Thomson-scattered signal from the center of the focal region as a function of laser intensity. The horizontal axis represents the peak intensity of the unaltered, nontrapping beam (laser energy could have been used equally well, where 700 mJ is equal to 10^{18} W/cm^2). The solid line is a straight-line fit to the trapping-beam signal (open squares), and the dashed line is a fit to the unaltered-beam signal (open circles). The gas species was either argon or nitrogen at a pressure of 1.0 or 2.5 Torr for any given run. The signal value is the total signal from the center of the focal region ($-75\ \mu$m $< z <$ 75 μm); the data from each run was normalized to the average signal strength (at E = 700 mJ) for each beam type, and each shot was background subtracted. The normalization of the trapping-beam data was performed independently of the normalization of the nontrapping-beam data. As expected, the signal strength and slope are enhanced for the trapping beam. The scatter in the data is likely due to fluctuations in the beam quality.

Figure 79.72(b) shows the predicted intensity scaling from the computer simulation for an ordinary focus (open circles, dashed line) and a trapping focus (open squares, solid line) generated from an incident flat-top beam focused into argon gas. The choice of gas species is arbitrary since the overall trends are universal. As in Fig. 79.72(a), the signal is taken from the center of the focal region. Because of the minimal amount of trapping with the ordinary beam, the scattered signal is low and varies weakly with laser intensity. As in the experiment, the signal from the trapping beam is larger and depends

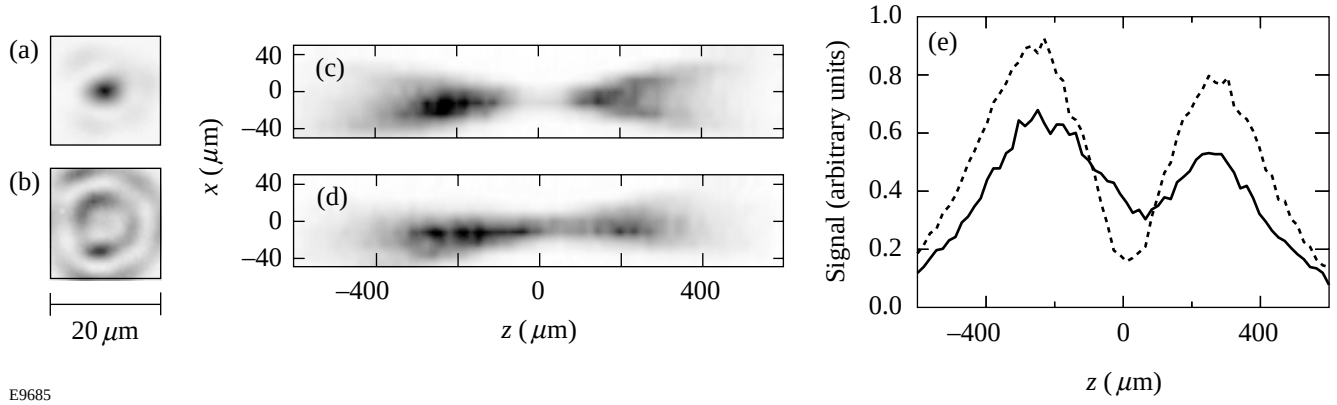

Figure 79.71
Observed focal-plane images and Thomson-scattered images. (a) Ordinary-beam focal-plane image taken at high power (E = 500 mJ) with CCD2, (b) trapping-beam focal-plane image, (c) image of Thomson-scattered radiation taken with CCD1 (30-laser-shot average) generated with the ordinary beam with 2.5 Torr of argon, viewed normal to the polarization direction, (d) image generated with the trapping beam, (e) total Thomson-scattered signal as a function of the laser-propagation direction (z). The signal from the trapping beam is greater at the center of the focal region and smaller on either side, as predicted.

more strongly on laser energy. The calculated contrast in signal strength and slope between ordinary and trapping beams is even greater when using a perfect Gaussian incident beam. A greater calculated signal enhancement is observed when using a "bright" trap, whose trapping region has a nonzero intensity minimum.[6] In such a trap, the effect on the nonlinear Thomson-scattered signal is especially pronounced since electrons are confined in a region of high field. Simulations also show that for an unaltered beam's peak intensity of $I_0 = 10^{19}$ W/cm^2, the nonlinear Thomson-scattering signal[10,11] from the center of a bright trap ($I_{center} = 0.20\ I_0$) is 2.2×10^4 times larger than the signal from the center of a Gaussian focus.

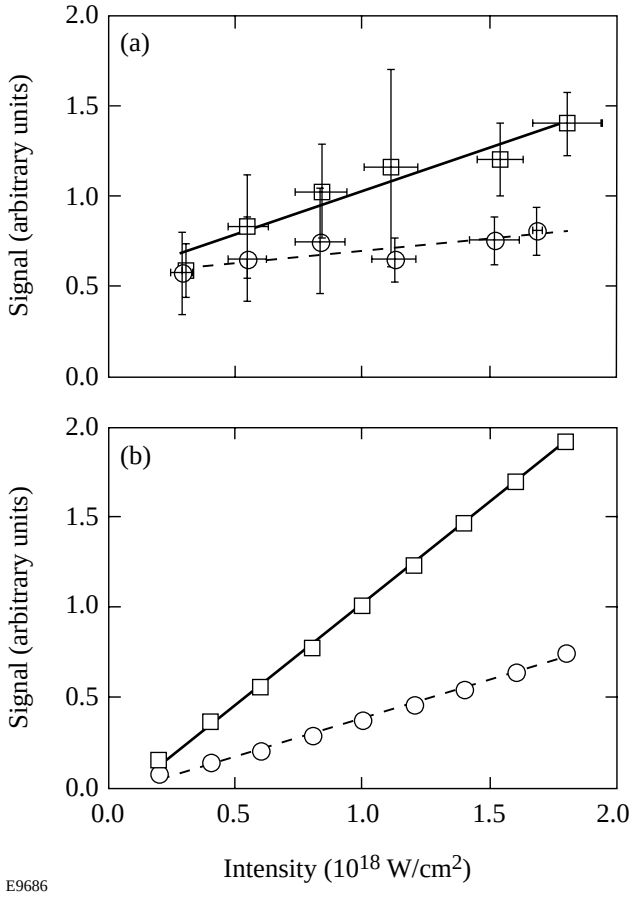

Figure 79.72
Energy dependence of Thomson-scattered light from the center of the focal region. (a) Experimental results of linear Thomson scattering from several data-taking runs with the ordinary beam (open circles, dashed line) and the trapping beam (open squares, solid line). (b) Results from a computer simulation with an ordinary focus (open circles, dashed line) and a trapping focus (open squares, solid line) generated by an incident flat-top beam. Both experiment and simulation show an increase in signal strength and energy dependence for the trapping beams due to the increased electron–laser interaction.

In conclusion, we have made the first observation of electron trapping in an intense laser beam. A novel, segmented-wave-plate scheme was used to generate the trapping focus. Electron trapping in the altered focus resulted in enhanced linear Thomson scattering from the center of the focal region as predicted by computer simulations. The observed increase in energy dependence was also expected. Computer simulations show that the trapping focus would also increase the signal generated by nonlinear Thomson scattering.

ACKNOWLEDGMENT

The authors thank A. Maltsev for machining the $\lambda/2$ plate. We also thank N. P. Bigelow, J. H. Eberly, Y. Fisher, and T. J. Kessler for helpful discussions. This research was supported by the National Science Foundation, with additional support by the U.S. Department of Energy Office of Inertial Confinement Fusion under Cooperative Agreement No. DE-FC03-92SF19460, the University of Rochester, and the New York State Energy Research and Development Authority. The support of the DOE does not constitute an endorsement by the DOE of the views expressed in this article.

REFERENCES

1. H. A. H. Boot and R. B. R.-S.-Harvie, Nature **180**, 1187 (1957).
2. A. V. Gapanov and M. A. Miller, J. Exptl. Theoret. Phys. (USSR) **34**, 242 (1958).
3. N. J. Phillips and J. J. Sanderson, Phys. Lett. **21**, 533 (1966).
4. U. Mohideen *et al.*, J. Opt. Soc. Am. B **9**, 2190 (1992).
5. C. I. Moore, J. Mod. Opt. **39**, 2171 (1992).
6. J. L. Chaloupka, Y. Fisher, T. J. Kessler, and D. D. Meyerhofer, Opt. Lett. **22**, 1021 (1997).
7. S. Chen, A. Maksimchuk, and D. Umstadter, Nature **396**, 653 (1998).
8. J. H. Eberly, in *Progress in Optics*, edited by E. Wolf (North-Holland, Amsterdam, 1969), Vol. 7.
9. J. D. Jackson, *Classical Electrodynamics*, 2nd ed. (Wiley, New York, 1975).
10. Vachaspati, Phys. Rev. **128**, 664 (1962).
11. E. S. Sarachik and G. T. Schappert, Phys. Rev. D **1**, 2738 (1970).
12. S. Augst, D. D. Meyerhofer, D. Strickland, and S. L. Chin, J. Opt. Soc. Am. B **8**, 858 (1991).
13. Y.-H. Chuang, D. D. Meyerhofer, S. Augst, H. Chen, J. Peatross, and S. Uchida, J. Opt. Soc. Am. B **8**, 1226 (1991).
14. M. D. Perry *et al.*, Phys. Rev. A **37**, 747 (1988).

Publications and Conference Presentations

Publications

A. Babushkin, W. Bittle, S. A. Letzring, M. D. Skeldon, and W. Seka, "Regenerative Amplifier for the OMEGA Laser System," in *Solid State Lasers for Application to Inertial Confinement Fusion*, edited by W. H. Lowdermilk (SPIE, Bellingham, WA, 1999), Vol. 3492, pp. 124–130.

A. Babushkin, R. S. Craxton, S. Oskoui, M. J. Guardalben, R. L. Keck, and W. Seka, "Demonstration of Dual-Tripler Broadband Third-Harmonic Generation and Implications for OMEGA and the NIF," in *Solid State Lasers for Application to Inertial Confinement Fusion*, edited by W. H. Lowdermilk (SPIE, Bellingham, WA, 1999), Vol. 3492, pp. 406–413.

A. Babushkin, J. H. Kelly, C. T. Cotton, M. A. Labuzeta, M. O. Miller, T. A. Safford, R. G. Roides, and W. Seka, "Compact Nd^{3+}-Based Laser System with Gain $G \leq 10^{13}$ and Output Energy of 20 J," in *Solid State Lasers for Application to Inertial Confinement Fusion*, edited by W. H. Lowdermilk (SPIE, Bellingham, WA, 1999), Vol. 3492, pp. 939–943.

T. R. Boehly, V. A. Smalyuk, D. D. Meyerhofer, J. P. Knauer, D. K. Bradley, R. S. Craxton, M. J. Guardalben, S. Skupsky, and T. J. Kessler, "Reduction of Laser Imprinting Using Polarization Smoothing on a Solid-State Fusion Laser," J. Appl. Phys. **85**, 3444 (1999).

C.-H. Chen, D. Katsis, P. H. Chen, J. C. Mastrangelo, and T. Tsutsui, "Circularly Polarized Light Produced with Glassy Liquid Crystal Films," Polymer Reprints **40**, 1171 (1999).

F. Dahmani, S. Burns, and J. C. Lambropoulous, "Arresting Ultraviolet-Laser Damage in Fused Silica," Opt. Lett. **24**, 516 (1999).

F. Dahmani, J. C. Lambropoulos, S. Burns, S. Papernov, and A. W. Schmid, "How Small Stresses Affect 351-nm Damage Onset in Fused Silica," in *Laser-Induced Damage in Optical Materials: 1998*, edited by G. J. Exarhos, A. H. Guenther, M. R. Kozlowski, K. L. Lewis, and M. J. Soileau (SPIE, Bellingham, WA, 1999), Vol. 3578, pp. 431–435.

O. M. Efimov, L. B. Glebov, S. Papernov, and A. W. Schmid, "Laser-Induced Damage of Photo-Thermo-Refractive Glasses for Optical-Holographic-Element Writing," in *Laser-Induced Damage in Optical Materials: 1998*, edited by G. J. Exarhos, A. H. Guenther, M. R. Kozlowski, K. L. Lewis, and M. J. Soileau (SPIE, Bellingham, WA, 1999), Vol. 3578, pp. 564–574.

K. Green, W. R. Donaldson, R. L. Keck, A. V. Okishev, M. D. Skeldon, W. Seka, and R. Sobolewski, "Transient Bandwidth Analysis of Photoconductive Microwave Switches Implemented in the OMEGA Pulse-Shaping System," in *Solid State Lasers for Application to Inertial Confinement Fusion*, edited by W. H. Lowdermilk (SPIE, Bellingham, WA, 1999), Vol. 3492, pp. 165–172.

K. S. Il'in, G. N. Gol'tsman, B. M. Voronov, and R. Sobolewski, "Characterization of the Electron Energy Relaxation Process in NbN Hot-Electron Devices," in the *Proceedings of the 10th International Symposium on Space Terahertz Technology*, edited by T. W. Crowe and R. M. Weikle (University of Virginia, Charlottesville, VA, 1999), pp. 390–397.

S. D. Jacobs, W. I. Kordonski, and H. M. Pollicove, "Precision Control of Aqueous Magnetorheological Fluids for Finishing of Optics," in the *Proceedings of the Sixth International Conference on Electro-Rheological Fluids, Magneto-Rheological Suspensions and Their Applications*, edited by M. Nakano and K. Koyama (World Scientific, Singapore, 1998), pp. 861–869.

J. M. Larkin, W. R. Donaldson, T. H. Foster, and R. S. Knox, "Reverse Intersystem Crossing from a Triplet State of Rose Bengal Populated by Sequential 532- + 1064-nm Laser Excitation," Chem. Phys. **244**, 319 (1999).

M. Lindgren, M. Currie, W.-S. Zeng, R. Sobolewski, S. Cherednichenko, B. Voronov, and G. N. Gol'tsman, "Picosecond Response of a Superconducting Hot-Electron NbN Photodetector," Appl. Supercond. **6**, 423 (1998).

J. A. Marozas, "The Cross-Phase Modulation Between Two Intense Orthogonally Polarized Laser Beams Co-Propagating Through a Kerr-like Medium," in *Solid State Lasers for Application to Inertial Confinement Fusion*, edited by W. H. Lowdermilk (SPIE, Bellingham, WA, 1999), Vol. 3492, pp. 454–465.

A. V. Okishev, M. D. Skeldon, and W. Seka, "Multipurpose, Diode-Pumped Nd:YLF Laser for OMEGA Pulse Shaping and Diagnostic Applications," in *Solid State Lasers for Application to Inertial Confinement Fusion*, edited by W. H. Lowdermilk (SPIE, Bellingham, WA, 1999), Vol. 3492, pp. 118–123.

S. P. Regan, D. K. Bradley, A. V. Chirokikh, R. S. Craxton, D. D. Meyerhofer, W. Seka, R. W. Short, A. Simon, R. P. J. Town, and B. Yaakobi, J. J. Carroll III, and R. P. Drake, "Laser–Plasma Interactions in Long-Scale-Length Plasmas Under Direct-Drive National Ignition Facility Conditions," Phys. Plasmas **6**, 2072 (1999).

M. D. Skeldon, A. V. Okishev, R. L. Keck, W. Seka, and S. Letzring, "An Optical Pulse Shaping System Based on Aperture-Coupled Striplines for OMEGA Pulse Shaping Applications," in *Solid State Lasers for Application to Inertial Confinement Fusion*, edited by W. H. Lowdermilk (SPIE, Bellingham, WA, 1999), Vol. 3492, pp. 131–135.

S. Skupsky and R. S. Craxton, "Irradiation Uniformity for High-Compression Laser-Fusion Experiments," Phys. Plasmas **6**, 2157 (1999).

R. Sobolewski, "Ultrafast Dynamics of Nonequilibrium Quasiparticles in High-Temperature Superconductors," in *Superconducting and Related Oxides: Physics and Nanoengineering III*, edited by D. Pavuna and I. Bozovic (SPIE, Bellingham, WA, 1999), Vol. 3481, pp. 480–491.

J. M. Wallace, T. J. Murphy, N. D. Delamater, K. A. Klare, J. A. Oertel, G. R. Magelssen, E. L. Lindman, A. A. Hauer, P. Gobby, J. D. Schnittman, R. S. Craxton, W. Seka, R. Kremens, D. K. Bradley, S. M. Pollaine, R. E. Turner, O. L. Landen, D. Drake, and J. J. MacFarlane, "Inertial Confinement Fusion with Tetrahedral Hohlraums at OMEGA," Phys. Rev. Lett. **82**, 3807 (1999).

J. D. Zuegel and W. Seka, "Upconversion and Reduced $^4F_{3/2}$ Upper-State Lifetime in Intensely Pumped Nd:YLF," Appl. Opt. **38**, 2714 (1999).

Forthcoming Publications

R. Adam, M. Currie, C. Williams, R. Sobolewski, O. Harnack, and M. Darula, "Direct Observation of Subpicosecond Single-Flux-Quantum in Pulse-Driven Y-Ba-Cu-O Josephson Junctions," to be published in Applied Physics Letters.

T. R. Boehly, A. Babushkin, D. K. Bradley, R. S. Craxton, J. A. Delettrez, R. Epstein, T. J. Kessler, J. P. Knauer, R. L. McCrory, P. W. McKenty, D. D. Meyerhofer, S. P. Regan, W. Seka, S. Skupsky, V. A. Smalyuk, R. P. J. Town, and B. Yaakobi, "Laser-Uniformity and Hydrodynamic-Stability Experiments at the OMEGA Laser Facility," to be published in Laser and Particle Beams.

S.-H. Chen, J. C. Mastrangelo, B. M. Conger, and D. Katsis, "Design, Synthesis, and Potential Application of Glass-Forming Functional Organic Materials," to be published in the Proceedings of the 6th International Polymer Conference, Kusatsu, Japan, 20–24 October 1997 (invited).

M. Currie, C.-C. Wang, R. Sobolewski, and T. Y. Hsiang, "Picosecond Nodal Testing of Centimeter-Size Superconducting Nb Microstrip Interconnects," to be published in Applied Superconductivity.

F. Dahmani, J. C. Lambropoulos, A. W. Schmid, S. Papernov, and S. J. Burns, "Crack Arrest and Stress Dependence of Laser-Induced Surface Damage in Fused Silica and Borosilicate Glass," to be published in the Journal of Applied Physics.

F. Dahmani, A. W. Schmid, J. C. Lambropoulos, and S. J. Burns, "Lifetime Prediction of Laser-Precracked Fused Silica Subjected to Subsequent Cyclic Laser Pulses," to be published in the Journal of Materials Science.

R. E. Giacone, C. J. McKinstrie, and T. Kolber, "Angular Dependence of Stimulated Brillouin Scattering in a Homogeneous Two-Dimensional Plasma," to be published in Physics of Plasmas.

V. N. Goncharov, J. A. Delettrez, S. Skupsky, and R. P. J. Town, "Modeling Laser Imprint for Inertial Confinement Fusion Targets," to be published in Physical Review Letters.

K. Green and R. Sobolewski, "Extending the *S*-Parameter Approach to Linear Time-Varying Microwave Devices: Part I. Analysis," to be published in IEEE Microwave Theory and Techniques.

S. D. Jacobs, S. A. Arrasmith, I. Z. Kozhinova, L. L. Gregg, H. J. Romanofsky, A. B. Shorey, D. Golini, W. I. Kordonski, P. Dumas, and S. Hogan, "Magnetorheological Finishing of KDP," to be published in the Proceedings of the 1999 Annual Meeting of the Optical Society of America.

D. Katsis, P. H. M. Chen, J. C. Mastrangelo, and S.-H. Chen, "Vitrified Chiral-Nematic Liquid Crystalline Films for Selective Reflection and Circular Polarization," to be published in Chemistry of Materials.

J. P. Knauer, R. Betti, D. K. Bradley, T. R. Boehly, T. J. B. Collins, V. N. Goncharov, P. W. McKenty, D. D. Meyerhofer, V. A. Smalyuk, C. P. Verdon, S. G. Glendinning, D. H. Kalantar, and R. G. Watt, "Single-Mode Rayleigh–Taylor Growth-Rate Measurements with the OMEGA Laser System," to be published in Physics of Plasmas.

R. S. Knox, "Physical Aspects of the Greenhouse Effect and Global Warming," to be published in the American Journal of Physics.

R. L. McCrory and J. M. Soures, "Status of Direct-Drive Inertial Confinement Fusion Research at the Laboratory for Laser Energetics," to be published in the Proceedings of the 2nd Symposium on Current Trends in International Fusion Research Review and Assessment, Washington, DC, 10–14 March 1997 (invited).

P. W. McKenty, "Direct-Drive Capsule Requirements for the National Ignition Facility and OMEGA Laser Systems," to be published in Fusion Technology.

P. W. McKenty and M. D. Wittman, "Characterization of Thick Cryogenic Layers Using an Interferometric Imaging System," to be published in Fusion Technology.

C. J. McKinstrie and E. A. Startsev, "Forward and Backward Stimulated Brillouin Scattering of Crossed Laser Beams," to be published in Physical Review E.

A. B. Shorey, W. I. Kordonski, S. R. Gorodkin, S. D. Jacobs, R. F. Gans, K. M. Kwong, and C. H. Farney, "Design and Testing of a New Magnetorheometer," to be published in the Review of Scientific Instruments.

A. B. Shorey, K. M. Kwong, and S. D. Jacobs, "Nanoindentation Hardness of Magnetic Particles Used in Magnetorheological Finishing (MRF)," to be published in the Journal of Materials Research.

V. A. Smalyuk, T. R. Boehly, D. K. Bradley, V. N. Goncharov, J. A. Delettrez, J. P. Knauer, D. D. Meyerhofer, D. Oron, D. Shvarts, Y. Srebro, and R. P. J. Town, "Nonlinear Evolution of Broad-Bandwidth, Laser-Imposed Nonuniformities in Planar Targets Accelerated by 351-nm Laser Light," to be published in Physics of Plasmas.

J. M. Soures, R. L. McCrory, R. Betti, W. Bittle, T. R. Boehly, R. Boni, D. K. Bradley, T. J. B. Collins, R. S. Craxton, J. A. Delettrez, W. R. Donaldson, R. Epstein, V. Glebov, V. N. Goncharov, D. R. Harding, P. A. Jaanimagi, R. L. Keck, J. H. Kelly, T. J. Kessler, J. P. Knauer, C. K. Li, S. J. Loucks, F. J. Marshall, P. W. McKenty, D. D. Meyerhofer, S. F. B. Morse, S. Padalino, R. Petrasso, P. B. Radha, S. Regan, W. Seka, R. W. Short, A. Simon, S. Skupsky, D. J. Smith, R. P. J. Town, B. Yaakobi, and J. D. Zuegel, "Recent Advances in Direct-Drive ICF Target Physics at the Laboratory for Laser Energetics," to be published in the Proceedings of the 1998 IAEA Conference, Yokohama, Japan, 19–24 October 1998.

M. D. Wittman and R. S. Craxton, "Self-Interference Patterns and Their Application to Inertial-Fusion Target Characterization," to be published in Applied Optics.

Conference Presentations

The following presentations were made at the Spring Meeting of the Materials Research Society, San Francisco, CA, 5–9 April 1999:

I. A. Kozhinova, S. R. Arrasmith, L. L. Gregg, and S. D. Jacobs, "Origin of Corrosion in Magnetorheological Fluids Used for Optical Finishing."

A. B. Shorey, S. D. Jacobs, W. I. Kordonski, S. R. Gorodkin, and K. M. Kwong, "Design and Testing of a New Magnetorheometer."

S. A. Arrasmith, S. D. Jacobs, A. B. Shorey, D. Golini, W. I. Kordonski, S. Hogan, and P. Dumas, "Studies of Material Removal in Magnetorheological Finishing (MRF) from Polishing Spots," 101st Annual Meeting of the American Ceramics Society, Indianapolis, IN, 25–28 April 1999.

The following presentations were made at CLEO/QELS 1999, Baltimore, MD, 23–28 May 1999:

A. Babushkin, W. A. Bittle, M. D. Skeldon, and W. Seka, "Diode-Pumped Regenerative Amplifier for the OMEGA Laser System."

A. Maksimchuk, J. Queneuille, G. Chériaux, G. Mourou, and R. S. Craxton, "Efficient Second-Harmonic Generation of Sub-100-fs Pulses from High-Power Nd:Glass Laser."

A. V. Okishev, "High-Repetition-Rate, Diode-Pumped, Multipass Preamplifier for the OMEGA Master Oscillator."

A. V. Okishev, D. Jacobs-Perkins, S. F. B. Morse, D. Scott, and W. Seka, "Prepulse Contrast Monitor for the OMEGA Drive Line."

M. D. Skeldon, A. V. Okishev, R. L. Keck, and W. Seka, "An Optical Pulse-Shaping System Based on Aperture-Coupled Striplines for OMEGA Pulse–Shaping Applications."

The following presentations were made at the 29th Annual Anomalous Absorption Conference, Pacific Grove, CA, 13–18 June 1999:

R. S. Craxton, D. D. Meyerhofer, S. P. Regan, W. Seka, R. P. J. Town, and B. Yaakobi, "Simulations of OMEGA Long-Scale-Length Plasmas Representative of the Transition Portion of NIF Direct-Drive Pulses."

J. A. Delettrez, S. P. Regan, T. R. Boehly, C. Stoeckl, D. D. Meyerhofer, P. B. Radha, J. Gardner, Y. Aglitskiy, T. Lehecka, S. Obenschain, C. Pawley, and S. Serlin, "Analysis of Planar Burnthrough Experiments on OMEGA and NIKE."

R. Epstein, T. J. B. Collins, J. A. Delettrez, V. N. Goncharov, S. Skupsky, R. P. J. Town, and B. Yaakobi, "Simulation of the Radiative Preheat of Target Foils and Shells in Laser-Driven Ablation and Implosion Experiments."

V. Yu. Glebov, D. D. Meyerhofer, P. B. Radha, W. Seka, S. Skupsky, J. M. Soures, C. Stoeckl, T. C. Sangster, S. Padalino, J. Nyquist, and R. D. Petrasso, "Tertiary Neutron Diagnostic by Carbon Activation."

V. N. Goncharov, "Modeling of Laser Imprint for OMEGA and NIF Capsules."

A. V. Kanaev and C. J. McKinstrie, "Numerical Two-Dimensional Studies of Near-Forward Stimulated Brillouin Scattering of a Laser Beam in Plasmas."

M. V. Kozlov and C. J. McKinstrie, "Analysis and Simulation of Sound Waves Governed by the Ion Fluid and Poisson Equations."

V. Lobatchev and R. Betti, "Numerical Study of Linear Feed-out of Short-Wavelength, Rear-Surface Perturbations in Planar Geometry."

C. J. McKinstrie and M. V. Kozlov, "Analysis and Simulation of Sound Waves Governed by the Korteweg–de Vries Equation."

D. D. Meyerhofer, R. Bahr, R. S. Craxton, S. P. Regan, W. Seka, R. P. J. Town, and B. Yaakobi, "Laser–Plasma Interactions in Plasmas Characteristic of the Direct-Drive NIF Foot-to-Main Drive Region."

S. P. Regan, J. A. Delettrez, T. R. Boehly, D. K. Bradley, J. P. Knauer, D. D. Meyerhofer, and C. Stoeckl, "Planar Burnthrough Experiments on OMEGA and NIKE."

R. W. Short, "Forward SBS, Filamentation, and SSD."

V. A. Smalyuk, F. J. Marshall, D. D. Meyerhofer, and B. Yaakobi, "Imaging of Compressed Shells with Embedded Thin, Cold, Titanium-Doped Layers on OMEGA."

Y. Srebro, D. Oron, D. Shvarts, T. R. Boehly, V. N. Goncharov, O. Gotchev, V. N. Smalyuk, S. Skupsky, and D. D. Meyerhofer, "Hydrodynamic Simulations of Static and Dynamic Laser Imprint."

E. A. Startsev and C. J. McKinstrie, "Particle-in-Cell Simulation of Ponderomotive Particle Acceleration in a Plasma."

C. Stoeckl, V. Yu. Glebov, D. D. Meyerhofer, W. Seka, V. A. Smalyuk, and J. D. Zuegel, "Hard X-Ray Signatures for Laser–Plasma Instabilities on OMEGA."

The following presentations were made at ISEC '99, Berkeley, CA, 21–25 June 1999:

R. Adam, C. Williams, R. Sobolewski, O. Harnack, and M. Darula, "Experiments and Simulations of Picosecond Pulse Switching and Turn-on Delay Time in Y-Ba-Cu-O Josephson Junctions."

K. S. Il'in, A. A. Verevkin, G. N. Gol'tsman, and R. Sobolewski, "Infrared Hot-Electron NbN Superconducting Photodetectors for Imaging Applications."

J. L. Chaloupka and D. D. Meyerhofer, "Observation of Electron Trapping in an Intense Laser Beam," Applications of High-Field and Short-Wavelength Sources VIII Topical Meeting, Potsdam, Germany, 27–30 June 1999.

UNIVERSITY OF
ROCHESTER